The Pennsylvania State University

The Graduate School

Department of Materials Science and Engineering

DEPOSITION AND MEASUREMENT OF EPITAXIAL BARIUM TITANATE THIN FILMS USING CONDUCTIVE EPITAXIAL OXIDE ELECTRODES PREPARED BY PULSED LASER DEPOSITION

A Thesis in
Ceramic Science

by
Jon-Paul Maria

Submitted in Partial Fulfillment
of the Requirements
for the Degree of

Master of Science

May 1996

I grant The Pennsylvania State University the nonexclusive right to use this work for the University's own purposes and to make single copies of the work available to the public on a not-for-profit basis if copies are not otherwise available.

Jon-Paul Maria

We approve the thesis of Jon-Paul Maria.

Date of Signature

Susan Trolier-McKinstry Assistant Professor of Ceramic Science Thesis Adviser	April 19, 1996
Darrell G. Schlom Assistant Professor of Materials Science and Engineering	April 19, 1996
Russell Messier Professor of Engineering Science and Mechanics	April 18, 1996
Clive A. Randall Associate Professor of Materials Science	April 18, 1996
Robert E. Newnham Alcoa Professor of Solid State Science	april 12, 1996
David J. Green Professor of Ceramic Science Chair of the Progran in Ceramic Science	April 19, 1996

ABSTRACT

In the manufacture of electroceramic devices, size is of primary concern. Marketing trends typically demand improved performance from the next generation of electronic devices in increasingly smaller packages. Central to those devices are the materials whose properties, such as conductivity or capacitance, make them useful. Unfortunately, those material properties which are well characterized for bulk samples are not always retained with decreasing physical dimension. As has been observed and explained for ferromagnetism, intrinsic size effects occur which result in a loss of some of the most useful material properties. A similar size effect has been observed in ferroelectric materials, but the problem is not well understood. Given the current interest in high density non-volatile memory devices, to which thin film ferroelectrics are central, much attention has recently been directed towards this problem. Thus, this thesis is intended to establish a basis upon which a fundamental study of the origins of intrinsic size effects can begin.

Epitaxial barium titanate films were prepared by laser ablation on a variety of single crystal substrates including MgO, $SrTiO_3$, LiF, and $LaAlO_3$. With the exception of spinel, the structure of the $BaTiO_3$ films was optimized for each substrate via characterization by 4-circle x-ray diffraction. The available processing variables in laser ablation, i.e,. pressure, laser fluence, and target to substrate separation, were investigated and it was determined that those parameter settings which optimize certain film characteristics can be detrimental to others. For example, a pressure of 50 mTorr and a target to substrate separation distance of 7.0 cm were found to produce films with the best thickness uniformity and morphology, however, the crystallinity of the films suffered damage from energetic particle bombardment. Knowing this, a compromise when establishing the deposition conditions may sometimes be necessary for the production of the best samples.

Heterostructures incorporating $SrRuO_3$ as an epitaxial bottom electrode and $BaTiO_3$ as an insulator were fabricated and optimized for structure. Electrical properties of

the $BaTiO_3$ were measured, but bulk values were not observed. The oxide bottom electrodes proved very sensitive to oxygen pressure and bombardment, making reliable and directly interpretable electrical property measurements non-trivial. Epitaxial barium titanate samples with Curie transitions depressed between 72 K and 165 K were made, with the ferroelectric nature substantiated by the presence of a polarization hysteresis and a diffuse peak in the temperature dependence of the dielectric constant. These samples had room temperature dielectric constants between 65 and 160, room temperature dielectric losses between 1 and 4%, and remnant polarizations ranging from of ~ 2 to 7 $\mu C/cm^2$ at 77 K. The depressions in T_c and the dilution of the ferroelectric properties were attributed to a derease in the coherent lattice dimension of the samples.

A brief study of the deposition pressure and bombardment dependence of the $SrRuO_3$ electrode was conducted. It was found that the material's conductivity could be changed from metallic to semiconducting depending upon the particular processing conditions. These differences were also observed optically via spectroscopic ellipsometric measurements. X-ray analysis of both the low pressure and high bombardment conditions revealed additional reflections as well as d-spacing measurements disparate from bulk values. Annealing at temperatures as high as 680°C did not result in measurable changes in the film crystallinity.

TABLE OF CONTENTS

List of figures vii
List of tables x
Acknowledgements xi
Chapter 1 INTRODUCTION 1
1.1 Introduction 1
1.2 Pulsed laser deposition (PLD) 3
1.2.1 History 3
1.2.2 Excimer lasers 4
1.2.3 Laser target interaction 5
1.2.4 Plume characterization 7
1.2.5 Particulate generation 9
1.3 Barium titanate 10
1.4 Size effects 20
1.4.1 Size effects in small particles 20
1.4.2 Size effects in fine grained ceramics 22
1.4.2.1 Anomalous room temperature dielectric constant 23
1.4.2.2 Loss of ferroelectricity 23
1.5 Barium titanate thin films 24
1.5.1 Pertinent thin film characterization techniques 27
1.5.1.1 X-ray diffraction 27
1.5.1.2 Raman scattering 27
1.5.1.3 Composition analysis 28
1.5.1.4 Electrical property measurements 29
1.5.1.5 Transmission electron microscopy 29
1.5.2 Experimental observations of size effects in thin films 29
1.5.2.1 Polycrystalline thin films 29
1.5.2.2 Epitaxial thin films 33
Chapter 2 EXPERIMENTAL PROCEDURE 39
2.1 Vacuum system 39
2.1.1 Vacuum chamber 39
2.1.2 Gas delivery 41
2.1.3 Substrate heating 42
2.1.4 Target rotation 44
2.2 Substrates 44
2.3 Excimer laser 45
2.4 Laser optics 46
2.5 Deposition of barium titanate films 46
2.6 Structural characterization 47
2.7 Morphological characterization 48
2.8 Compositional characterization 48
2.9 Electrical property measurements 48
Chapter 3 DEPOSITION PARAMETER STUDY 51
3.1 On-axis deposition 51
3.2 Off-axis thickness distribution study 59
Chapter 4 EPITAXIAL DEPOSITION AND OPTIMIZATION OF BATIO3 FILMS 64
4.1 BaTiO3 deposition on magnesium oxide 64
4.2 Barium titanate deposition on lithium fluoride 69
4.3 Barium titanate deposition on lanthanum aluminate (001) 73

4.4 Barium titanate deposition on strontium titanate..... 79
Chapter 5 HETEROSTRUCTURE FABRICATION AND MEASUREMENT..... 86
5.1 Heterostructure Fabrication..... 86
5.2 BSL and BSS series heterostructures..... 86
5.3 Morphology for the BSL and BSS heterostructure systems..... 95
5.4 Electrical property measurements..... 97
5.5: SrRuO3 deposition as an oxide bottom electrode:..... 117
Chapter 6 SUMMARY AND FUTURE WORK..... 131
6.1 Hardware..... 131
6.2 Deposition uniformity study..... 131
6.3 Deposition of epitaxial barium titanate..... 133
6.4 Heterostructure deposition..... 134
6.5 Electric property measurements..... 135
6.6 Pressure and Bombardment dependence of SrRuO3..... 136
REFERENCES..... 138

TABLE OF FIGURES

Figure 1.1: Laser induced thermal cycle 5
Figure 1.2: $BaTiO_3$ pseudo-perovskite unit cell with room temperature dimensions..... 10
Figure 1.3: Crystallographic phases of $BaTiO_3$..... 11
Figure 1.4: Hysteresis loop for $BaTiO_3$ crystal..... 13
Figure 1.5: Permittivity versus Temperature..... 14
Figure 1.6: Spontaneous polarization versus Temperature..... 14
Figure 1.7: Continuity conditions for dielectric displacement..... 16
Figure 1.8: Domain formation 17
Figure 1.9: Formation of depolarization field..... 17
Figure 1.10: Polarization distribution of thin ferroelectric crystals..... 18
Figure 1.11: Epitaxial interfaces..... 35
Figure 2.1: PSU MRL PLD chamber schematic..... 40
Figure 2.2: Ozone delivery schematic..... 42
Figure 2.3: Substrate heater..... 43
Figure 2.4: Schematic of thin film capacitors 49
Figure 3.1 Plume behavior as a function of background pressure..... 55
Figure 3.2: a-SRO surface roughness pressure dependence 56
Figure 3.3: Microstructural comparison between films deposited at 57
Figure 3.4: Thickness distribution of film as a function of target to substrate distance..... 58
Figure 3.5: Schematic of off-axis ablation arrangement 60
Figure 3.6: Off axis thickness distribution as a function of distance from target face for different background gas pressures..... 61
Figure 3.7: Normalized thickness distribution as a function of distance from target 63
Figure 4.1: {001} surface schematic of magnesium oxide..... 64
Figure 4.2 Temperature dependence of the lattice constants of MgO and $BaTiO_3$..... 65
Figure 4.3: θ-2θ scan of $BaTiO_3$ on MgO (001)..... 67
Figure 4.4: Phi-scan of $BaTiO_3$ (101) reflection..... 68
Figure 4.5: ω-scan of the $BaTiO_3$(002) reflection 68
Figure 4.6: LiF {001} crystal surface..... 69
Figure 4.7: θ-2θ scan of $BaTiO_3$on LiF (001)..... 70
Figure 4.8: ϕ-scan of $BaTiO_3${101} reflections on LiF (001)..... 71
Figure 4.9: ω-scan of $BaTiO_3$(003) reflection on LiF (001) 71
Figure 4.10: Temperature dependence of the lattice constants of LiF and $BaTiO_3$ 72
Figure 4.11: {001} surface of $LaAlO_3$, numbers indicate height in unit cell..... 74
Figure 4.12: Temperature dependence of the lattice constants of $LaALO_3$ and $BaTiO_3$ 75
Figure 4.13: θ-2θ scan of $BaTiO_3$on $LaAlO_3$ (001)..... 76
Figure 4.14: ϕ-scan of $BaTiO_3$(101) reflections..... 76
Figure 4.15: ω-scan of $BaTiO_3$(002) reflection..... 77
Figure 4.16: Close-up of $BaTiO_3$(002) rocking curve..... 77
Figure 4.17: Close-up in 2θ of thin $BaTiO_3$films grown on $LaAlO_3$ 79
Figure 4.18: {001} surface of $SrTiO_3$, numbers give the heights along <001> in the unit cell..... 80

Figure 4.19: Temperature dependence of the lattice constants of $SrTiO_3$ and $BaTiO_3$ 81
Figure 4.20: θ-2θ scan of $BaTiO_3$on $SrTiO_3$ (001) 82
Figure 4.21: ϕ-scan of $BaTiO_3$(101) reflections 82
Figure 4.22: Rocking curve of $BaTiO_3$(002) reflection 83
Figure 5.23: Twinned orientations of $BaTiO_3$ and the diffractometer angles which satisfy the Bragg conditions for diffraction 84
Figure 4.24: θ-2θ scan of $BaTiO_3$ (114) reflection on a $SrTiO_3$ substrate 85
Figure 5.1: θ-2θ scan of BSS-series off-axis grown heterostructure 87
Figure 5.2: ϕ-scan of BSS-series, off-axis $SrRuO_3$ off-axis $BaTiO_3$(101) peak 88
Figure 5.3: ω-scan of BSS-series off-axis $SrRuO_3$ off-axis $BaTiO_3$(002) peak 88
Figure 5.4: θ-2θ scan of BSL-series off-axis $SrRuO_3$ on-axis $BaTiO_3$heterostructure 89
Figure 5.5: ϕ-scan of BSL-series off axis $SrRuO_3$ on-axis $BaTiO_3$(101) peak 90
Figure 5.6: ω-scan of BSL-series off-axis $SrRuO_3$ on-axis $BaTiO_3$(002) reflection 90
Figure 5.7: θ-2θ scan of BSL-series on-axis $SrRuO_3$ on-axis $BaTiO_3$heterostructure 91
Figure 5.8: ϕ-scan of BSL-series on-axis $SrRuO_3$ on-axis $BaTiO_3$(101) peak 92
Figure 5.9: ω-scan of BSL-series on-axis $SrRuO_3$ on-axis $BaTiO_3$(002) reflection 92
Figure 5.10: Trend in (004) peak position with increasing bombardment for $BaTiO_3$ films 94
Figure 5.11: SEM image of columnar BSL-series heterostructure, ... 96
Figure 5.12: SEM image of smooth BSL-series heterostructure 97
Figure 5.13: Current voltage characteristics for sample BSL-18 100
Figure 5.14: Linear relationship between Log leakage current and applied electric field 102
Figure 5.15: Temperature dependence of Permittivity of BSS-12 and BSL-18 104
Figure 5.16: Mosaic structure representation in an epitaxial film 106
Figure 5.17: Field and temperature dependent polarization hysteresis curves for BSS-12 108
Figure 5.18: Field and temperature dependent polarization hysteresis curves for BSL-18 110
Figure 5.19: Temperatutre dependence of the dielectric constant of BSL-10 113
Figure 5.20: Curie-Weiss plot for BSL-10 114
Figure 5.21: Application of scaling theory for the determination of gamma 115
Figure 5.22: θ-2θ scan of low and high pressure deposited $SrRuO_3$ 120
Figure 5.23: ϕ-scans of low and high pressure deposited $SrRuO_3$ films 121
Figure 5.24: ω-scans of low and high pressure deposited $SrRuO_3$ films 122
Figure 5.25: θ-2θ scan of an off-axis $SrRuO_3$ film 124
Figure 5.26: θ-2θ pattern for $SrRuO_3$ deposited in $O_3/0_2$/Ar mix 125
Figure 5.27: Temperature dependence of the resistivity of $SrRuO_3$ films 126
Figure 5.28: Proposed model for increasing resisitivity in bombarded$SrRuO_3$ 128
Figure 5.29: Potential distribution in (a) a perfect crystal and (b) a disordered crystal 129
Figure 5.30: Anderson distribution of localized and delocalized states 130

TABLE OF FIGURES

Table 1: Ionic displacements through ferroelectric transition 12
Table 2: Size effects observed in small particle barium titanate 21
Table 3: $BaTiO_3$ thin film deposition methods 25
Table 4: Sample designation and description 98
Table 5: Coherence length determination data 104
Table 6: Summary of the electrical property data obtained for BSS-12 and BSL-18 110
Table 8: Simulated dielectric response of BaTiO3 film upon addition of a parasitic non-ferroelectric layer of variable permittivity and volume fraction 116

Table 8: Results of $BaTiO_3$ depositions 133
Table 9: Electrical property data summary for $BaTiO_3$ 135

ACKNOWLEDGEMENTS

The completion of this Master's thesis represents an important milestone in my academic career. The truition of this goal would not have been possible without the help and guidance of the following individuals to whom I am very grateful: My advisor, Dr. Susan Trolier-McKinstry, Dr. Darrell G. Schlom, Dr. Clive Randall, Dr. Robert E. Newnham, Dr. Russell Messier, Dr. Larry Pilione, Brady J. Gibbons, Johanna L. Lacey, Pavadee Aungkavattana, Sonny Gross, and The IMRL technical support staff. Thank you all very much.

Chapter 1

INTRODUCTION

1.1 Introduction

Perovskite crystals represent a family of often ferroic materials rich in commercially useful properties such as high permitivity, piezoelectricity, electrostriction, pyroelectricity, and non-linear optical effects. In most cases, these properties are due to the presence of a phase transition leading to a low temperature stable ferroic state [Jaffe, Cook and Jaffe, 1971]. In many of these cases, this non-ferroic to ferroic transition is also a function of some material dimension.

In 1943 the high permitivity ceramic barium titanate was discovered and very rapidly integrated into existing capacitor technology [Arlt, Hennings, and de With, 1985]. The very large permitivity values, which can be as large as 10,000, make this material very useful, but the instability of the enormous dielectric constant with dimension made both the reproducibility and integratibility of this extraordinary material non-trivial.

Often considered to be the prototype perovskite ferroelectric, barium titanate displays a very pronounced size effect such that below a critical dimension all ferroelectric properties are lost [Arlt *et al.*, 1985 and Kinoshita and Yamaji, 1975]. This will ultimately limit the usefulness of barium titanate and many other ferroelectrics in small particle, fine grain, or thin film forms. These effects become commercially important in applications such as piezoelectric actuators, where mechanical toughness increases with decreasing grain size; in multilayer capacitors, where capacitance increases with decreasing dielectric thickness; and in DRAMs, where the dielectric thickness is limited to 10's of nanometers in order to achieve reasonable storage densities. The very pronounced size effects in barium titanate do, however make it a prime candidate for the study of this phenomena.

The term size-effects has been widely adopted and refers to the variability of the dielectric properties with some critical material dimension. Size effects have been studied as a function of grain size in ceramic materials, thickness in bulk single crystals, ferroelectric domain size, coherent scattering domain size, and thickness in epitaxial films [Arlt *et al.*, 1985, Kinoshita and Yamaji, 1975, Cao and Randall, 1995, Biryukov *et al.*, 1984, Frey and Payne, 1993, and Yoneda *et al.*, 1993] Unfortunately, the crystal boundary conditions for each of these systems are unique. Given that the polarization in ferroelectric barium titanate cannot be decoupled from the spontaneous strain, residual stress and its dependence upon physical boundary conditions would be a worthy variable to consider. A barium titanate grain in a ceramic matrix experiences residual stresses in three dimensions, while the same grain, contained in a polycrystalline film, to a first approximation, would experience only planar stress. If indeed residual stress is a determining factor in producing size effects, one can appreciate that the critical size for ferroelectricity should not be the same for the two systems.

In this investigation, epitaxial barium titanate thin films have been chosen since they afford the largest array of material parameters to be investigated. For epitaxial films, along with thickness, the effect of crystalline quality of the films may be investigated by modifying the substrate lattice mismatch and growth temperature. The effects of these changes can be quantified by diffraction methods and correlated to size effects. In addition, the residual stresses due to thermal expansion mismatch between film and substrate can also be varied by choosing the appropriate substrates.

The barium titanate films investigated in this work were deposited by pulsed laser deposition. Though this technique is currently inappropriate for commercial use or industrial scale production, the rapid deposition rates and the ability to deposit nearly any solid makes this technique ideal for such an investigation.

1.2 Pulsed laser deposition (PLD)

1.2.1 History

Closely following the development of the first high power ruby laser in 1963, much interest in the interaction of high fluence radiation with solid surfaces evolved. The ability to rapidly vaporize a solid surface became apparent. The first demonstration using laser energy to generate and transport a vapor phase occurred in 1965 by Smith and Turner who deposited dielectric and metal films with a ruby laser [Smith and Turner, 1965]. For the two decades ensuing, little work involving laser ablation was done, largely due to the popularity of other techniques such as sputtering and evaporation, and the youth of laser technology. Two major breakthroughs led to the current surge of PLD popularity; the invention of the 'Q'-switch, which allowed lasers to be rapidly pulsed with extremely short durations and high peak intensities, and more importantly, the demonstration of complex multicomponent superconducting oxide deposition [Chrisey and Hubler, 1994 and Venkatesan *et al.*, 1988]. The work of Venkatesan at Bellcore showed that the large energy density incident upon a solid target resulted in congruent material removal, even for multicomponent oxides such as $YBa_2Cu_3O_{7-\partial}$, and the subsequent deposition of stoichiometric films [Venkatesan *et al.*, 1988]. Though sputtering techniques can boast the same capabilities, bombardment by energetic species and resputtering have proven problematic for maintaining composition in multi-cation systems, particularly where one species is considerably more volatile than the others [Surowiak, 1989]. Molecular beam epitaxy has also been used to deposit these compositions, but the hardware expense and the difficulty in evaporating refractory metals such as tantalum and zirconium suppress widespread application. For these reasons, pulsed laser deposition has become quite common in thin film laboratories, and has now been used to deposit over 200 materials.

Following the surge of interest in high temperature superconducting materials (HTSC's), other perovskite based materials were studied by PLD. The work of Ramesh,

Krupanidhi, and Norton showed early on that ferroelectric compositions with complex stoichiometries could be successfully deposited by PLD [Krupanidhi *et al.*, 1991, Norton and Carter, 1990, and Ramesh *et al.*, 1991]. The large number of compositions which have been attempted in the last 4 years attests to the agility of this technique.

1.2.2 Excimer lasers

The majority of PLD systems use excimer gas lasers for material removal. These lasers have proven to be well suited for PLD of insulators due to the large fluence (~1J), ideal wavelength regime (190-308nm), and short pulse lengths (~25 ns).

In the case of an excimer laser operating with a krypton/fluorine gas mixture, the lasing action comes from the degeneration of the excited excimer molecule. Energy is pumped into the mixture via a rapid avalanche electronic discharge in the range of 25 to 40 kV. Spanning a distance of ~3 cm, the field produced ranges from 10 to 15 kV/cm. In the presence of an inert buffer gas, typically Ne or He, the excimer molecules are formed as a result of the discharge. Since the lifetime of the ground state excimer molecule is shorter than that of the excited species, the condition of population inversion is easily achieved, leading to the high pulse energy. The typical 25 ns pulse length of excimer lasers results from the lifetime of the excimer molecule [Chrisey and Hubler, 1994].

The ultraviolet portion of the spectrum is best suited for PLD since in that spectral regime most materials absorb strongly. Large absorption coefficients are desirable since they tend to minimize the interaction volume of the solid, thus minimizing target degradation and particle ejection. Longer wavelengths tend to travel deeper into the target, resulting in a thermal evaporation process rather than ablation [Chrisey and Hubler, 1994]. It would of course be desirable to reduce the wavelength to an even smaller value, but this would require optics efficient in the vacuum ultraviolet region.

1.2.3 Laser target interaction

Understanding the interaction of the laser beam with the target surface is of primary importance for thin film deposition by laser ablation. Several attempts have been made to model the laser solid interaction and the subsequent material removal, but none have provided a comprehensive model. The difficulty in modeling this seemingly simple process suggests that several mechanisms are involved.

When a high intensity pulse of coherent photons is incident upon a solid target, a rapid thermal cycle is induced and repeated with each successive shot. The influencing factors are the laser wavelength, fluence, absorption coefficient of the target, pulse length and the target thermophysical properties. Following finite difference models, Singh and Narayan have elucidated three important aspects of surface modification by radiation [Singh and Narayan, 1990]:

1. The maximum temperature reached in the solid, and the melt depth increase with increasing wavelength, or decreasing energy.
2. The thermal pulse penetrates deeper into solids with low absorption coefficients and high thermal conductivities.
3. Shorter pulse lengths produce higher melting and solidification velocities.

Figure 1.1 graphically illustrates this thermal cycle.

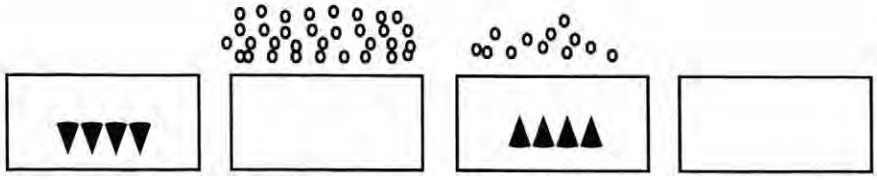

Figure 1.1: Laser induced thermal cycle
(i) melt front moves into solid
(ii) Vapor is ejected and plasma forms through vapor/laser interaction
(iii) beam ceases and melt front proceeds back to surface
(iv) Surface is left modified after laser incidence

Initially, the solid surface absorbs the radiation and melts. The melted region expands into the solid while vaporization begins. After the pulse, the melt front recedes back towards the surface, where irregularities due to shock waves are frozen in. The target surface has now been altered, and will continue to degrade with successive pulses [Singh and Narayan, 1990].

A threshold energy exists which separates ablation from thermal evaporation. The most important characteristic of the ablation mechanism is the congruent removal of the target composition. Unlike sputtering, where the individual yields may differ by a factor of 2 or more for different cations in a multicomponent system, given the appropriate laser intensity, all components of a complex target will be removed stoichiometrically [Yamakawa, 1996]. The threshold for ablation can be quantified by measuring film composition as a function of laser intensity, or can be qualitatively observed by the presence of a luminous plasma. Profilometric measurements may also be made on the irradiated zone of the target, such that the fluence at which a depression can be measured may be deemed the threshold energy [Chrisey and Hubler, 1994].

The most striking aspect of laser ablation is the luminous plasma present at the target surface. This occurs as a result of secondary interaction between the laser pulse and evaporant. It has been observed that evaporated material leaves the surface during the laser pulse, leading to the very important photon-vapor interaction. Electrons and ions are thermionically emitted from the irradiated surface and couple strongly with the incident electromagnetic radiation. Being accelerated by the beam, these particles collide with each other, and more importantly the ambient gas molecules (referred to as inverse *Bremsstrahlung*) [Chrisey and Hubler, 1994]. The charged particle population will rapidly increase due to cascade ionization, and the target will effectively be shielded from the laser beam. As a result of beam blocking, the plasma will extinguish until the beam can once again penetrate to the target, starting the entire cycle once more. In this manner, the plume is self regulating with its characteristics determined by fluence, spot size, gas pressure, and

target optical and thermophysical properties [Singh and Narayan, 1990, Emmony *et al.*, 1973, Cheung and Sankur, 1988, and Atwater *et al.*, 1990]. The size and shape of the plasma is most strongly influenced by the pressure, but the plume always evolves normally to the irradiated surface regardless of the laser incidence angle, following the pressure gradient of the solid vapor [vanDriel *et al.*, 1982].

Upon a visual inspection of the laser-induced plasma two coincident components are easily observed. In a simplified treatment, the entire plasma may be thought of as a superposition of a standard cosine distribution upon a peaked $\cos^n\theta$ distribution where n scales with background pressure. Following this approximation, the $\cos\theta$ component would be a result of thermal evaporation, and the peaked distribution a result of some non-equilibrium ablation process. The $\cos\theta$ component is believed to be a result of evaporation since the films deposited from this region do not conserve the stoichiometry of the target. In addition to being observable visually, the same results have been obtained by film thickness distribution measurements where a discontinuity in the thickness profile is observed and indicates a second material removal mechanism [vanDriel *et al.*, 1990].

1.2.4 Plume characterization

A laser-induced plasma may consist of electrons, ion, radicals, neutrals, molecules clusters, and boulders. Because of this wide variety of species, no one spectroscopic technique can accurately characterize the plume. Several techniques, each offering different sensitivity regimes must be used for thorough investigation [Goehegan, 1992, and Zhang *et al.*, 1989].

Mass spectrometry has proven quite useful for characterization at low pressures and laser fluences. This technique has been demonstrated to very accurately measure the initial ions emitted from a surface, hence qualitatively determining the ablation threshold as well as material removal mechanisms at low fluence values [Weidman and Heluajian, 1991]. When gas pressures and laser fluences are increased, as would be the case during a

deposition, the species density and their velocity distribution increase to values which are beyond the sensitivity of mass spectrometry.

To overcome the difficulties of high pressure plasma measurements by mass spectrometry, traditional ion-probe methods have been used. Though this method does not have the species resolution of mass spectrometry, the robust construction allows its use in such rugged environments as a laser plasma. Such measurements have been made for the ablation of yittrium barium copper oxide, (YBCO) with a KrF laser in atmosphere, (vacuum - 200 mTorr), by Geohegan, [1991].

Detailed chemical information about the plume can be collected by emission or absorption spectroscopy by comparing the experimental findings with tabulated spectra for materials. If the emission or absorption spectra are then collected as a function of time, the energies and populations of the plume species may also be known. Again for the case of YBCO PLD by KrF radiation, time resolved optical methods show an abundance of ionic species and their relative concentrations [Champeaux *et al.*, 1992].

To investigate the hydrodynamic aspects of laser plasmas, fast photography techniques have been used. Unlike other PVD methods, the laser plasma exhibits turbulent flow regions which can be directly imaged. The most typical experiment uses an intensified CCD array, or ICCD (intensified charge coupled device) photography [Geohegan, 1992]. These studies have demonstrated that the propagation of the plume is hindered by the background gas, which tends to attenuate and scatter the plasma species.

The general results of these characterization methods are that the plume is comprised of many species, both charged and neutral, micro and macroscopic; the energies of the species range anywhere from 10 to 10,000 eV, depending upon pressure and fluence; the degree of ionization of the plasma can be as large as 50%; and that in gas ambients, the plume exhibits hydrodynamic behavior [Geohegan, 1991, Geohegan, 1992, and Champeaux *et al.*, 1992].

1.2.5 Particulate generation

The most unfortunate aspect of pulsed laser deposition is the production of macroscopic particles often termed boulders. The boulders are formed as a result of the explosive nature of the laser/solid interaction. Several mechanisms have been proposed to explain their origin, all of which depend most importantly upon the laser fluence.

After multiple incidences of laser radiation, small cone-like features form on the target surface. These features have been attributed to two mechanisms which depend upon the incident laser fluence. In the case of low fluence radiation, irregularities referred to as ribbons form as a result of diffraction effects at the focus of a lens. These features are not interesting, as the intensities of laser pulses which cause them are less energetic than the ablation threshold of most solids [Emmony *et al.*, 1973 and vanDriel *et al.*, 1982]. The more important origin of these feature is the presence of small concentrations of impurities or compositional heterogeneities distributed throughout the target which result in spatially non-uniform evaporation rates. Some regions will preferentially evaporate, forming trenches, while those regions which are more refractory form the cones. As the trench depth increases, the cone heads become slim and mechanically unstable. Eventually they are dislodged and expelled towards the growing film surface [Dyer *et al.*, 1986, and Geohegan, 1991].

Cone-like features need not be present for boulder production. Splashing is a second source of macroparticles. When produced by this mechanism, boulders are characterized by a condensed globular structure. Coincident with the explosive expansion of the plume is a significant recoil pressure imposed upon the target. When this recoil pressure impinges upon the thin molten skin of the irradiated surface, the result is ejection of the liquid [Chrisey and Hubler, 1994]. Again, the amount of macroparticles produced in this fashion is related directly to the laser fluence.

The production of boulders and their subsequent deposition represent the most serious detriment of laser ablation. Since this is an intrinsic property of the technique,

much similar to arc-plasma discharge deposition, the process is unsuited for many commercial processes. Though many schemes have been designed to avoid the deposition of boulders, mechanical filters [Champeaux *et al.*, 1992], off-axis geometries [Goehegan, 1992], and multiple laser systems [Strikovski *et al.*, 1993], none offer a complete solution. Boulders can however be minimized by setting the laser fluence only slightly greater than the threshold energy.

1.3 Barium titanate

Barium titanate is one of a large number of room temperature ferroelectric crystals exhibiting the perovskite structure in its paraelectric state. Barium titanate occurs in two primary crystallographic forms, a high temperature hexagonal phase, stable above 1460°C, and the nominally perovskite phase stable at temperatures lower. Figure 1.2 illustrates the ferroelectric room temperature tetragonal perovskite unit cell of $BaTiO_3$.

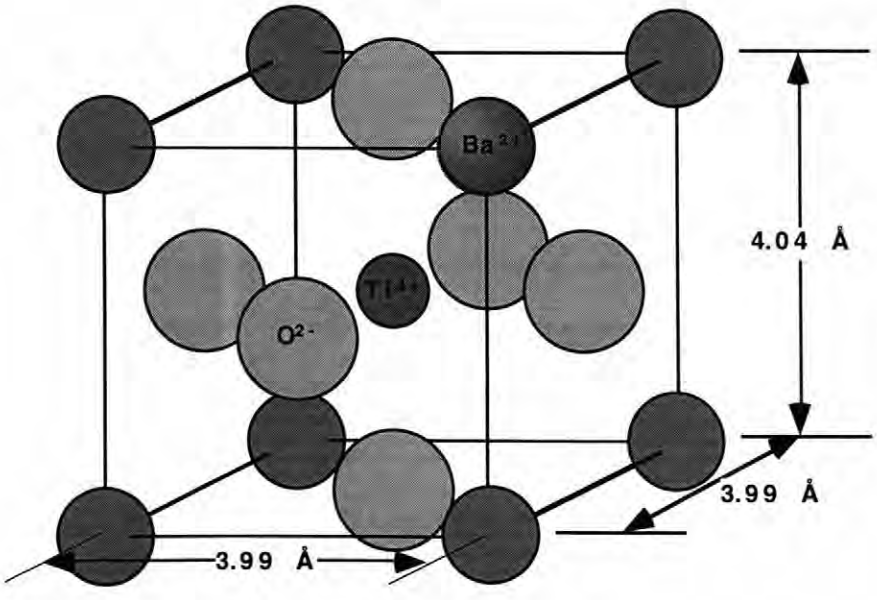

Figure 1.2: $BaTiO_3$ pseudo-perovskite unit cell with room temperature dimensions

The transition between the hexagonal and perovskite structures is kinetically limited, so the metastable high temperature structure can be observed at room temperature. Owing to its electrical properties, the perovskite phase is widely utilized in the electronic ceramic industry, unlike the hexagonal phase which has little application.

Paraelectric barium titanate has the formula ABO_3, where Ba^{2+} ions occupy the A site, and Ti^{4+} ions occupy the B site of the standard perovskite unit cell. At room temperature in the ferroelectric phase barium titanate has a distorted perovskite structure belonging to the space group P4mm.

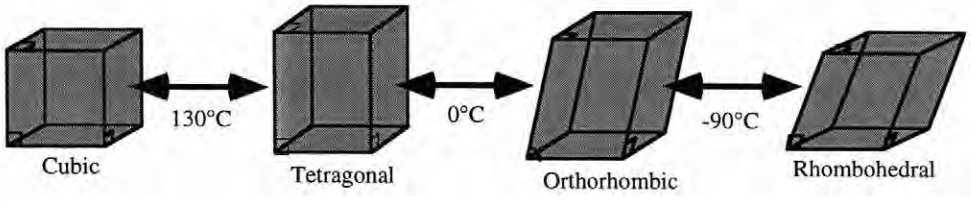

Figure 1.3: Crystallographic phases of $BaTiO_3$
The monoclinic subcell is shown for the orthorhombic phase [Herbert, 1985]

Upon the first order transition from the high temperature cubic paraelectric phase to the tetragonal ferroelectric phase, nominally occurring at 130°C, the cubic cell elongates by 1.00% along c and contracts 0.10% along a and b, corresponding to a net volume gain of 0.80%. Accompanying this elongation is a loss of the center of symmetry, and the acquisition of a polar axis and spontaneous polarization. Tetragonal barium titanate polarizes along the [100] direction with a shift in the oxygen and titanium ions in the cell. When the field is applied along the polar axis, the titanium ions shift with the applied field while the oxygens shift both with and opposite to the applied field. Table 1 lists the ionic

displacements which occur through the transition. The maximum polarization value of ~ 26 $\mu C/cm^2$ can be measured along the tetragonal BaTiO3 c-axis.

Table 1: Ionic displacements through ferroelectric transition
[Lines and Glass, 1979]
(decimal numbers are in angstroms)

Unit cell position in cubic phase	Ba^{2+} (0,0,0)	Ti^{4+} $(\frac{1}{2},\frac{1}{2},\frac{1}{2})$	O^{2-} (1) $(\frac{1}{2},\frac{1}{2},0)$	O^{2-} (2) $(\frac{1}{2},0,\frac{1}{2})$	O^{2-} (2) $(0,\frac{1}{2},\frac{1}{2})$
Relative displacement after transition	(0,0,0)	$(\frac{1}{2},\frac{1}{2},\frac{1}{2}$ + 0.05)	$(\frac{1}{2},\frac{1}{2}$,-0.09)	$(\frac{1}{2},0,\frac{1}{2}$ - 0.06)	$(0,\frac{1}{2},\frac{1}{2}$ + 0.06)

The tetragonal phase is stable down to 0°C (some report 5°C) at which point a second transition to the orthorhomic phase occurs. Polarization in the orthorhombic phase occurs along the <110> type directions of the cubic phase. A third transition occurs at -90°C to the rhombohedral state in which polarization occurs along the <111> type directions. The tetragonal state is of most interest due to its stability at room temperature and its values of permittivity and polarization which are the largest of all the phases [Jaffe, Cooke and Jaffe, 1971].

Ferroelectric domains nucleate in barium titanate upon cooling through the Curie transition, forming in both 90° and 180° geometries. 180° domain walls form parallel to the {100} type planes and are typically 4 to 10 angstroms in width, while 90° domain walls form along the {110} type planes and are near 100 angstroms wide [Jaffe, Cook and Jaffe, 1971]. The 90° walls form as a mechanism for reducing the stress generated by the elongation of the barium titanate unit cell c axis, any uncompensated surface charges, or as a result of physical discontinuities. Along the {110} planes, the two domain configurations can meet coherently with no strain, hence this geometry is stable.

Well prepared $BaTiO_3$ crystals exhibit strong hysteresis and a remanant polarization value of ~26μC/cm^2 at room temperature. Figure 1.4 shows the polarization vs. applied field behavior for a high quality single crystal specimen.

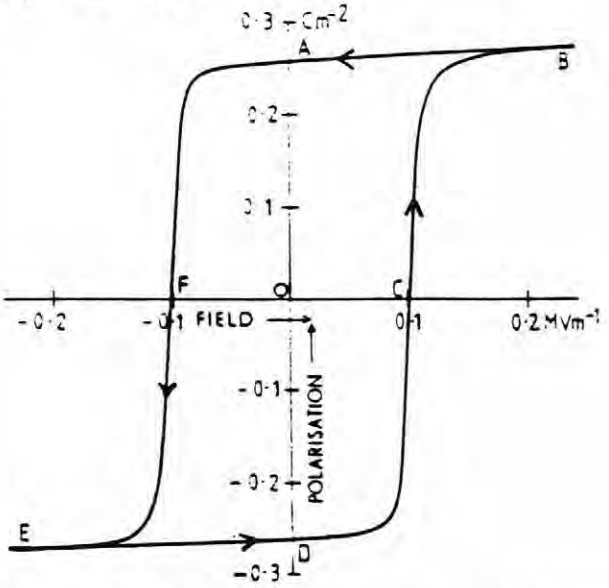

Figure 1.4: Hysteresis loop for $BaTiO_3$ crystal at room temperature [Herbert, 1985]

Given the small magnitude of the structural reconstructions associated with the phase transformations, the best way to observe them is by monitoring the changes of the dielectric constant with temperature. Permittivity and polarization values for $BaTiO_3$ as a function of temperature are shown in the following figures:

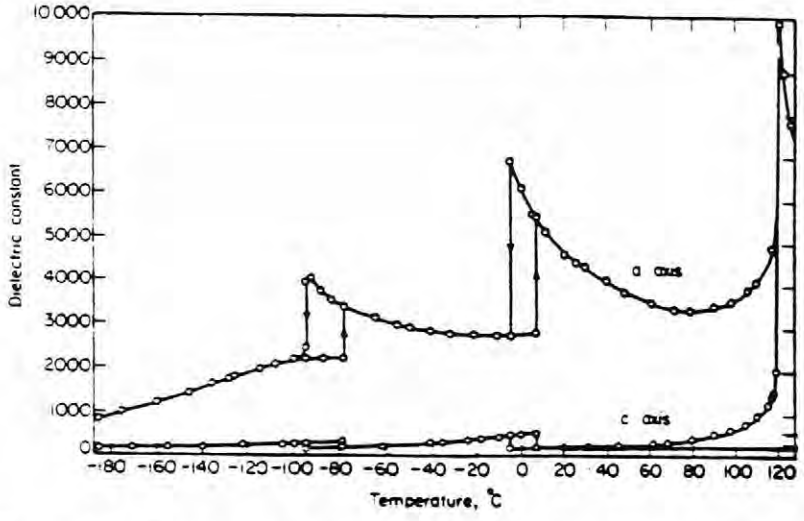

Figure 1.5: Temperature dependence of the permittivity in $BaTiO_3$ [Merz, 1949]

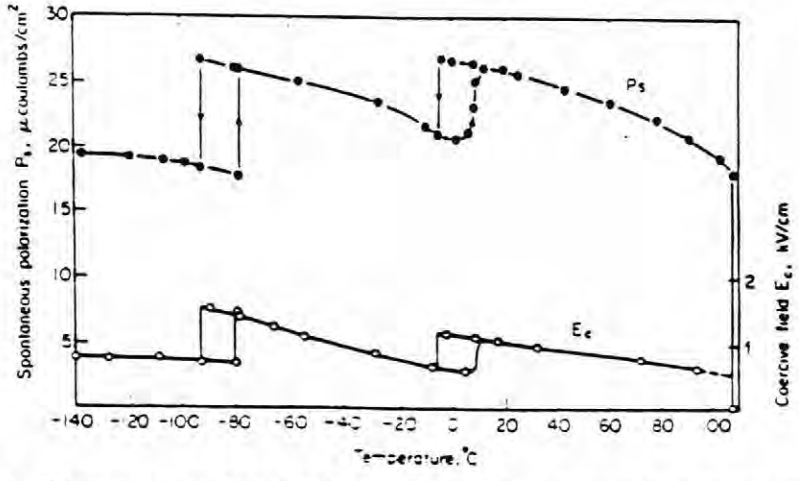

Figure 1.6: Temperature dependence of the spontaneous polarization in $BaTiO_3$ [Merz, 1953]

The electrical properties of barium titanate are strongly influenced by small changes in composition. Barium titanate, which is an equimolar mixture of BaO and TiO_2 has a very small region of solid solubility. Only approximately 3% excess of TiO_2 can be accommodated into the structure, after which, Ti enriched phases such as $BaTi_2O_5$ evolve [Jaffe, Cook and Jaffe, 1971]. If excess BaO is encountered, the Ba_2TiO_4 will evolve nearly immediately. Since these observations have been made for powder processed materials where equilibrium conditions prevailed, they may not accurately predict the behavior for vapor deposited barium titanate, where the opportunity for metastable phases is considerably larger [Smith, D. L., 1995].

The remainder of section 1.3 describes the dependence of the ferroelectric properties on pressure and surface conditions of $BaTiO_3$. These phenomena are introduced since their influence upon size-induced transitions is likely to be important.

The ferroelectric properties of barium titanate exhibit a strong dependence upon externally applied stresses. From experiments in which hydrostatic compressive stresses were applied to barium titanate crystals, it was found that the Curie point of $BaTiO_3$ decreased linearly with hydrostatic pressure, but the rate at which this decreased depended upon sample impurities and domain structure. As well, confirmation of Curie-Weiss behavior was made at constant pressures, and a critical pressure was found beyond which the spontaneous and remanant values of polarization dropped to zero [Samara, 1966]. Since the paraelectric-ferroelectric transition in $BaTiO_3$ is first order, it must obey the Clausius-Clapeyron equation:

$$\frac{dT_c}{dp} = T_c \Delta \frac{V}{Q}$$

where:

dT_c/dp = Pressure coefficient of the transition temperature

T_c = Curie temperature

ΔV = transition volume change

Q = Latent heat of transition

Samara found the value of the pressure coefficient of the transition temperature to be -7°C/kbar.

A second set of experiments have been conducted where radial stresses were applied about the circumference of round barium titanate crystals. In the case of this planar stress, the transition temperature was found to increase parabolically with applied stress. The interpretation of these experiments was somewhat more straightforward, since the stresses were applied only perpendicularly to the barium titanate polar axis. In this case, the applied stress tended to stabilize the crystal tetragonality, requiring more thermal energy for the transformation to the cubic phase [Forsbergh Jr., 1954].

Though the presence of an intrinsic surface layer in barium titanate is widely accepted, the size, origin, or actions of this heterogeneity on thin specimens is not understood [Binder, 1981, Kretschmer and Binder, 1979, Dudkevich *et al.*, 1977, Lezgintseva, 1977]. The most convincing argument as to the origin of such layers stems from the electrostatic boundary conditions obtained through Maxwell's equations. These intrinsic surface layers should not be confused with extrinsic ones for which more mundane explanations apply [English, 1968]. To the best of the author's knowledge, intrinsic surface layers have never been experimentally observed. For a system consisting of two dielectric media, at the interface we know that the dielectric displacement vector $\underline{D}$ perpendicular to the surface of both must be the same:

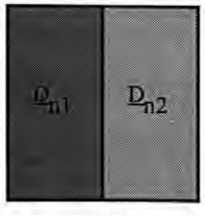

$\underline{D}_{n1} = \underline{D}_{n2}$

where: $\underline{D}_n = \varepsilon_o \underline{E} + \underline{P}$

Figure 1.7: Continuity conditions for dielectric displacement

If a monodomain, perfectly insulating, ferroelectric crystal in atmosphere with a homogeneous spontaneous net polarization is considered, the continuity condition at the surface is violated. For the above conditions to be satisfied, some process must occur to eliminate the polarization. In a bulk crystal, 180° domains form such that the net polarization and dielectric displacement is zero.

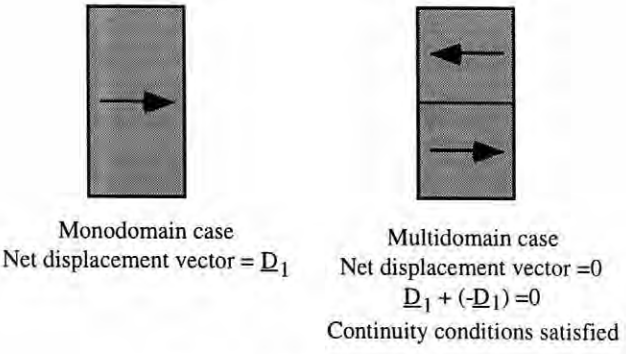

Figure 1.8: Domain formation

In the case where conductive electrodes are deposited on both of the monodomain crystal surfaces and connected in short circuit, a depolarization field will form. This field will counter the spontaneous polarization of the crystal, once more satisfying the continuity conditions.

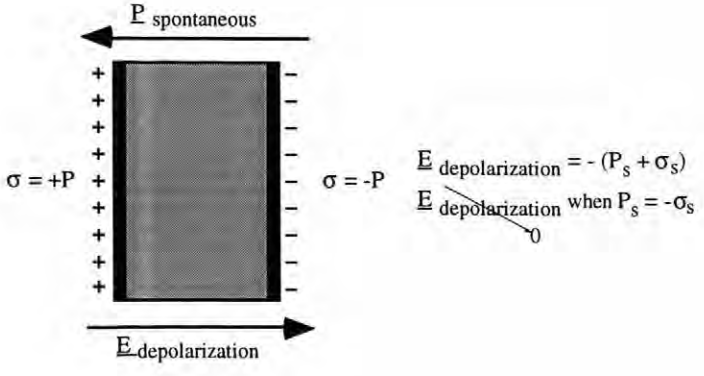

Figure 1.9: Formation of depolarization field

In the case of a ferroelectric crystal with no conductive electrodes, domain formation is the primary way in which the continuity conditions can be satisfied. However, in very thin crystals where the ability to form domains may be limited, some other mechanism must exist which allows the electrostatic boundary conditions to be satisfied. Such a mechanism has been proposed and involves the formation of a surface layer in which the surface polarization is reduced. Binder *et al.* proposed and modeled a ferroelectric surface which had compensated for the polarization boundary conditions [Binder, 1981]. Two conditions were proposed, virgin and electroded surfaces. The following figure shows the polarization distribution in the dielectric slab for both terminations.

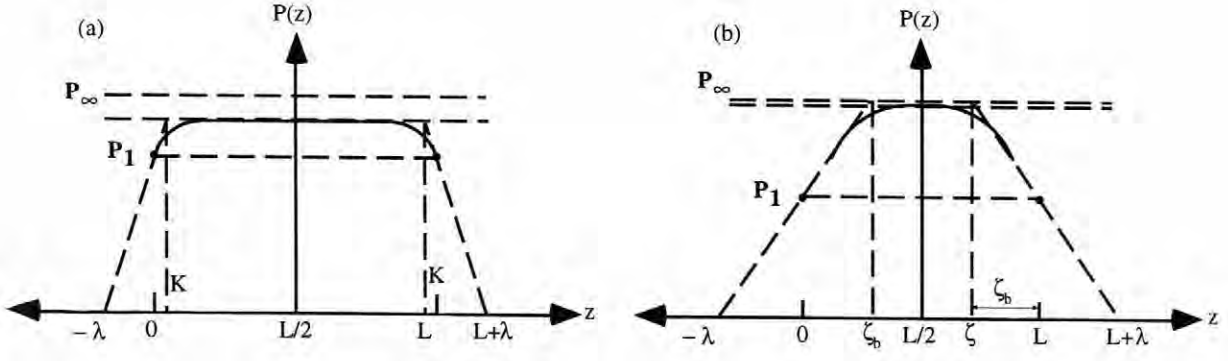

Distribution of polarization across a film of thickness L in the case where depolarizing fields have to be included (a) or not included (b), $P_\infty = P_b$.

where:

ζ = correlation length

λ = extrapolation length

P_1 = surface polarization

P_∞ = bulk polarization

Figure 1.10: Polarization distribution of thin ferroelectric crystals [Binder, 1981]

For the case of the plot which includes depolarizing fields (i.e., corresponding to the electroded case), the distribution is nearly uniform, trailing only at the very edges. In the case of no depolarizing fields, the polarization values drop sharply on either end [Binder, 1981]. This explanation of an intrinsic size effect would be consistent with observed trends, but it was not shown whether the surface layer thickness scales with the crystal thickness. Only if the thickness of this surface layer remains constant would this explanation quantify size induced transitions. Furthermore, neither an appropriate physical model nor a definitive experiment has accompanied this theoretical explanation. If the physical analog which accompanied this theory was indeed a tetragonal to cubic transition about the surface, detection of such structure would be very difficult. Structural characterization techniques such as electron diffraction (RHEED and LEED) typically do not have the resolution to detect such small crystallographic differences as is the case of $BaTiO_3$.

Upon examination of fine particle surfaces with electron diffraction, Kanzig *et al.* observed that a surface layer which showed enhanced tetragonality at temperatures well above the bulk Curie transition. This observation does not support a size induced transition, rather the contrary. The powders used were produced by extensive milling, so such a surface is very likely an artifact of the processing [Anliker *et al.*, 1954]. The surface layers of $BaTiO_3$ ceramics were as well examined by diffraction techniques by Goswami, and the unusual surface of the particles was claimed to have disappeared upon firing. It is again unclear as to whether the layer disappeared due to grain growth or surface reconstruction [Goswami, 1969]. The existence of a surface layer for barium titanate has been experimentally proven, but only for crystals of significant thickness. Lezgintseva estimated the thickness of surface layers in $BaTiO_3$ crystals thinned by acid etching. The thinnest crystals were 37 μm thick and shown to have layers of a-domains and anti-parallel c-domains. The thickness of the layers was found to be independent of the total thickness [Lezgintseva, 1965]. English as well studied the surface layers by electron spectroscopy,

determining largely the same results. In addition, English found that the maximum thickness of the surface was 0.7 μm [English, 1968]. Though the existence of surface layers has been proven for thick crystals, its presence and influence on size-induced transitions is as yet unknown.

1.4 Size effects

It has long been recognized that many materials do not follow the symmetry of scale, that is, their specific material properties change as a function of some material dimension. Initially observed in fine grained materials, and more recently in thin film specimens, size effects in ferroelectrics, metals, ferromagnetics, HTSC's (high temperature superconductors), and superfluids have been investigated [Arlt *et al.*, 1985, Fillipovich and Kalinina, 1965, Schlag *et al.*, 1995, Uchino *et al.*, 1989, and Kniepkemp, *Wang et al.*, and Heywang, 1954].

One can appreciate that any property which is cooperative in nature should exhibit such behavior. An excellent example of this occurs in the HTSC $YBa_2Cu_3O_{7-\partial}$ [Wang *et al.*, 1991], where in thin film stacked heterostructures, it was observed that although even one unit cell thick layers would exhibit superconductivity, the cooperation of several unit cells was necessary to obtain the bulk value of the superconducting transition temperature.

The size effects in ferroelectric materials are somewhat more complicated than those observed in other areas due to the intimate coupling of the elastic and electrical properties of ferroelectric materials. Given the obvious differences in the elastic boundary conditions for different physical material geometries and their potential influence on ferroelectricity, different size effects may be observed in small particles, fine grains, and thin films. In the following section, the size effects in thin film materials will be discussed along with a brief mention of size effects in the other systems.

1.4.1 Size effects in small particles

Small particles and very small single crystals may exhibit the purest form of size effects in ferroelectrics. The fewest number of external forces act upon free particles as they are not bound to a substrate, which dominates the film's mechanical behavior, or confined in three dimensions by a stiff matrix as in a ceramic. Many of the difficulties encountered when studying small particle size effects are associated with producing them. Grinding is one technique of producing small particles, but grinding artifacts such as amorphous surfaces can make interpretation difficult. Many barium titanate fine powders have been fabricated by chemical precursors, but as such, insurance of stoichiometry and chemical homogeneity is non-trivial. Given the assumption that stoichiometric fine particle barium titanate powders are produced, the size distribution of the material may add difficulty since ceramic particle specimens are rarely monodispersed. These particle size distributions make determination of a critical size difficult. Though structural measurement of small particles may be easily done by x-ray methods, meaningful electrical property values are difficult to obtain. Typically, a sufficiently dense compact is required (~60%) for measurements of permittivity or hysteresis, but in producing such a compact, the characteristics of the material may change, i.e., elastic stresses produced by pressing a pellet may significantly affect the measurements. Also, in measuring a powder compact, an appropriate model must be constructed which accounts for the fact that a significant portion of the specimen is air. Other methods such as Raman scattering and second harmonic generation are possible, but weak signal intensities and diffuse transitions can make interpretation difficult.

The following table lists several researchers who have studied small particle barium titanate, their fabrication methods, characterization techniques, and the critical sizes below which paraelectric $BaTiO_3$ was observed.

Table 2: Size effects observed in small particle barium titanate

Investigators	Powder Synthesis	Characterization	Critical Size
Schlag *et al.*	Sol-Gel	Raman scattering Diffraction Calorimetry	50 nm
Anliker *et al.*	Milling	X-ray diffraction	15 nm
Uchino *et al.*	Hydrothermal and co-precipatated	X-ray diffraction	120 nm

As can be appreciated from this brief list, the critical size for ferroelectricity is not well defined. Given the small magnitude of the spontaneous strain in tetragonal barium titanate, the lower limit of ferroelectricity, as judged by structural measurements, may depend heavily upon the resolution and sensitivity of the characterization instrument. For this reason, the presence of a ferroelectric phase may best be judged by electrical property measurements where quantities such as dielectric constant and remanant polarization between the para and ferroelectric states change by orders of magnitude rather then several percent. It should also be mentioned that the possibility of processing artifacts must always be considered. Anliker, who produced fine particles by milling alone undoubtedly imparted significant damage to the small particle surfaces. Thus, structural probes of the surface layers may indicate tetragonality, or likewise amorphous material; either of these features could be caused by surface damage or residual stress rather than an intrinsic size effect.

In order to explain size effects in small particles, Uchino *et al.* suggested that as the size of a particle decreases, the radius of curvature and the effective surface tension increase. This surface tension was then treated as hydrostatic pressure and added to the free energy summation for the phenomenological treatment of ferroelectricity, following the work of Samara [1966], who measured the dependence of the transition temperature on applied hydrostatic stress. The appropriate surface tension value would then result in total loss of the ferroelectric phase just as hydrostatic pressure did in Samara's work. However,

if the surface energy were back calculated assuming 120 nm as the critical size and that all pressure was due to surface tension, an unreasonably large value results.

1.4.2 Size effects in fine grained ceramics

Two size effects exist for polycrystalline barium titanate ceramics: anomalous dielectric properties and the apparent loss of ferroelectricity. The result of the two effects together is a maximum in the electrical property values at a grain size of approximately 1 μm.

1.4.2.1 Anomalous room temperature dielectric constant

First reported by Kniepkemp and Heywang in 1954, an increase in dielectric constant was observed for ceramic bodies with decreasing grain sizes [Kniepkemp and Heywang, 1954]. The room temperature dielectric constant reached a maximum of ~ 5000 at an average grain size of about 1 μm. This was most unusual given that the room temperature value of the permittivity or dielectric constant along the a-axis of $BaTiO_3$ has been measured at 4000 and 160 along c, and no amount of grain directional averaging could result in such a value without external influence.

Arlt and co-workers proposed a domain wall theory to explain this dielectric anomaly. The theory proposes that at grain sizes less than 10 μm, the domain size decreases in response to increasing stress in the grains. It was also proposed that a stress exists at the termination of a domain by a grain boundary. Following these propositions it could be determined that as the domain wall density increased the intrinsic termination stress per unit volume increases as well. The consequence of this increase in domain walls and domain wall stresses is an enhancement of the domain wall contribution to the dielectric constant. Arlt confirmed this by experimentally showing that the domain density increases with decreasing grain size, and that the measured dielectric constant reaches a maximum value at grain sizes near 0.7 μm, then quickly falls as the average size decreases further [Arlt *et al.*, 1985].

1.4.2.2 Loss of ferroelectricity

In ceramic bodies, as the average grain size is decreases below ~ 0.7 μm, the observed dielectric constant decreases, and the tetragonality of the crystals decreases until ultimately a paraelectric material results. Uchino *et al.* reported this behavior for barium titanate ceramic bodies and determined by x-ray diffraction that the critical grain size for tetragonality was 0.12 μm. Models proposing that the loss of tetragonality with decreasing grain size was due to increased amounts of internal or residual strains produced upon cooling through the transition pose an interesting question since the same stresses are used to explain the anomalously large room temperature dielectric constant observed in ~1 μm ceramic grains. Such a contradiction reinforces the complicated nature of this problem and the difficulties encountered in constructing an appropriate model or explanation.

1.5 Barium titanate thin films

Barium titanate has been deposited by nearly every modern deposition technique. The first recorded deposition of barium titanate occurred in 1963 by researchers at the Philco Scientific Laboratory in Blue Bell Pennsylvania. Müller *et al.* used a grain by grain sublimation technique to deposit barium titanate directly onto heated lithium fluoride crystals. Epitaxy of the barium titanate films was demonstrated by reflection electron diffraction [Müller *et al.*, 1963]. Table 3 lists several groups and the methods used to prepare barium titanate films along with their substrate choices. This list is by no means a complete reference for $BaTiO_3$ depositions, but it demonstrates the wide variety of depositions techniques used for growth of this fascinating material.

Table 3: $BaTiO_3$ thin film deposition methods

Researchers	Deposition Methods	Substrate Material
Müller, Nicholson and Turner	Grain-by-grain evaporation	Lithium Fluoride (epitaxy)
Terauchi, Watanabe, Kasatani, Kamagaki, Yano, and Terashima	Activated reactive evaporation	MgO and $SrTiO_3$ (epitaxy)
Norton and Carter	Pulsed laser ablation	MgO (epitaxy)
Abe and Komatsu	R.F. sputtering	MgO and $SrTiO_3$ (oriented)
Frey and Payne	Spin-coated sol-gel	Pt-Silicon
Pilleux and Fuenzalida	Hydrothermal deposition	Ti-Silicon
Van Buskirk, Stauf, Gardiner, Kirlin, Kumar, and Gallatin	Chemical vapor deposition	MgO (oriented)
Zhang, Cui, Gordon, Van Buskirk, and Steinbeck	Plasma enhanced MOCVD	$LaAlO_3$ (oriented)
Wills, Lu, Wessels, Zhan, Helfrich, and Ketterson	Metal organic CVD	Pt-MgO (oriented)
McKee	Molecular beam epitaxy	MgO-Silicon (epitaxial)

Through careful transmission electron microscopy analysis (TEM), Norton and Carter showed that on MgO single crystal substrates, pulsed laser deposited barium titanate grew by island nucleation. Nucleation was initiated preferentially at substrate steps with the discrete islands eventually converging to form continuous layers. Dislocations were also observed parallel to the [100] direction and were found to repeat approximately every 40 angstroms [Norton and Carter, 1990]. In addition to the growth study, compositional analysis was performed, and it was found through Rutherford backscattering spectrometry (RBS) that the deposition temperature had an undetectable effect on the final film stoichiometry in the temperature range of 600 to 850°C.

Few electrical property measurements have been reported for epitaxial barium titanate films. The unusually large dielectric loss of the barium titanate crystallites and the absence of insulating grain boundaries to confine space charges make reliable electrical properties difficult to measure. Epitaxial barium titanate films exhibiting bulk electrical properties have not been reported. For polycrystalline barium titanate films, most often

deposited from solution precursors, excellent electrical measurements have been made. Values of saturation polarization as large as 21 $\mu C/cm^2$, room temperature relative dielectric constants as large as 1000 and dielectric loss tangents of 0.07 have been reported. Such sol-gel derived films typically exhibit sub-micron grain sizes [Kamalasan *et al.*, 1993, and Hayashi *et al.*, 1993].

Thin film specimens represent a new class of materials where the properties of the film can differ appreciably from those observed in the bulk. More often than not, great care must be taken to extract bulk properties from thin film samples. For this reason, thin films represent an ideal medium for the investigation of size induced transitions in ferroics since the effects of material scale are often quite pronounced.

Thin film preparation techniques afford acute control of the physical and chemical properties of materials. When deposited from a vacuum environment, the film's properties may be tailored intimately by careful control of the deposition parameters, while a high degree of compositional purity is maintained. No other processing technique can offer the same level of control or reproducibility. As an example, during sputter deposition, grain size in ferroelectric films may be modulated by several orders of magnitude simply by changing the growth temperature and bombardment conditions. As well, the ability to produce crystallographically textured or single crystal materials is available. *In-situ* measurements, which are a relatively new area of interest, offer a new dimension in materials characterization in that properties of interest can be monitored as a function of time such that the properties and their evolution during growth may be known.

Thin films are not, however, without their drawbacks, the most obvious of which being the great expense associated with vacuum equipment. A constant concern with thin film preparation and evaluation lies in the selection of a suitable substrate and its chemical and mechanical influence. Prudent substrate selection must be made, as the mechanical behavior of the film, with the exception of the very thickest samples, will be dominated by the substrate. Residual stresses or other such deposition artifacts, like texturing, must

always be considered when interpreting experimental results. When materials are deposited at elevated temperatures, the possibility of a reaction layer between the film and its support must always be considered. Such reaction layers are often undetectable by x-ray diffraction, but may have a serious impact on the electrical properties of the sample. A final difficulty associated with thin film science is the difficulty in characterization due to the very small sample size. The following section is intended to describe several methods for measuring size effects as they may be somewhat different for thin films as compared to bulk samples.

1.5.1 Pertinent thin film characterization techniques

1.5.1.1 X-ray diffraction

Characterization of the crystalline structure of a sample is typically straightforward and involves measuring a powder diffraction pattern. For thin films, however, the supposition of an infinite array of x-ray scatterers may not be satisfied; this may result in peak broadening. This peak broadening, in addition to the weak diffracted signal, as compared to bulk samples, often limits the available resolution, making the detection of split peaks difficult. The presence of substrate reflections as well as substrate artifacts (ghost peaks) can also confuse interpretation. For epitaxial films where the substrate's structure and lattice are purposely closely matched, overlapping x-ray reflections hinder observation of the film structure. The problems associated with x-ray diffraction are relieved somewhat for polycrystalline samples where the grain size can be independent of film thickness, but for epitaxial films where the overall film thickness is small, determination of the structure may be non-trivial.

1.5.1.2 Raman scattering

Even though the spontaneous strain in barium titanate is ~ 1% and often difficult to detect by x-ray analysis, the result of this very small structural change is quite dramatic on the material's vibrational spectra. Strong features indicative of the non-cubic phases exist

for barium titanate, but once again, for thin film samples, the interference from the substrate as well as the weak signal from a thin sample make direct measurement difficult [Robins *et al.*, 1994]. If the film is deposited upon an optically opaque substrate, like platinum, which has no first order Raman spectrum, the measurement is simplified. Alternatively, when the film has been deposited upon a more complex material, like conductive oxides or oxide substrates, all layers will contribute and obfuscate the spectrum. For this reason, the materials system used can limit the applicability of Raman scattering. Since the probe is a visible laser, Raman scattering experiments can be very useful because they allow a structural measurement to be made as a function of some experimental parameter like temperature or pressure relatively simply.

1.5.1.3 Composition analysis

Though measuring composition is not a direct indicator of size effects, the structure and properties of ferroelectric materials are quite sensitive to small deviations from stoichiometry. Confirmation of composition is especially important for epitaxial thin films where more opportunity may exist for the presence of a metastable phase. That is, the material composition may be considerably off-stoichiometry, but the crystalline structure may be stabilized by the substrate. Again, composition can be difficult and expensive to determine. If the condensate can be efficiently removed from the substrate by etching, then photochemical analysis can be used. If however, this is not the case, but the film is very thick, an electron microprobe may be appropriate. Since this situation is often not observed, composition by characteristic x-ray emission is typically performed only on thin films in a TEM. Secondary ion mass spectrometry (SIMS) or Auger electronic spectroscopy (AES) can be used, but artifacts stemming from preferential sputtering rates and large experimental errors must be accounted for.

1.5.1.4 Electrical property measurements

Undoubtedly, the best confirmation of the ferroelectric nature of a thin film sample is the presence of a measurable hysteresis or maximum in the dielectric constant as measured with temperature. There are, however practical limitations to making such measurements, most importantly being the ability to deposit thin layers which are continuous and free of physical defects which result in shorting between the counterelectrodes. For techniques such as pulsed laser deposition which are plagued with the problem of particulate generation, construction of such structures can be difficult.

1.5.1.5 Transmission electron microscopy

Convergent beam electron diffraction in the TEM is a reliable method for judging point group symmetry of a barium titanate thin film specimen, especially due to the ability to observe high index reflections where the angular separation between the reflections is large. The time consuming nature of specimen preparation does, however, limit TEM investigations. Consideration must be taken as to the integrity of the sample and whether the characteristics change as a result of the thinning process, continuous bombardment by high energy electrons, or local beam heating.

1.5.2 Experimental observations of size effects in thin films

1.5.2.1 Polycrystalline thin films

The observed size effects in ferroelectric polycrystalline films can be both similar and dissimilar to those observed in fine grained ceramics depending upon the morphology of the ferroelectric film. In polycrystalline films grown both at room and elevated temperatures the possibility for anisometric morphologies always exists. The question is then posed as to what the actual grain size is. In a plan view SEM image, the grains in a textured thin film may look to be equiaxed and 10's of nm in dimension, whereas in reality, the image may represent the tops of columns which are considerably taller than they are wide. In such a system, it is difficult to know how to assign a dimension or critical size for ferroelectricity. Given the appropriate growth conditions, polycrystalline films with truly

equiaxed grains may be synthesized, and in such a case, the assignment of a grain size would be more meaningful.

For the interpretation of polycrystalline films, as compared to ceramics, an extra parameter must be considered, that being the residual strain induced by the substrate. In both high and low temperature depositions the substrate will constrain the film in two ways. In low temperature deposited films, the amorphous ferroelectric layer can grow in either a relaxed or strained state, this depending upon the bombardment during deposition. Upon crystallization, the volume change of the layer will typically result in the generation of tensile stresses in the film, assuming the interface retains its mechanical integrity. Assuming that crystallization occurs completely at the anneal temperature, during cooldown, in addition to the strain induced by volume change upon crystallization, the thermal expansion mismatch between the film and substrate will result in additional film stress, the sign of which is, of course, dependent upon the relative mismatch [Nix, 1989]. The stresses generated by volume change during crystallization can be minimized by depositing amorphous material of the same density as the bulk crystals, but the thermal expansion stresses cannot be avoided. The thermal expansion mismatch-induced strain may be quantified by the following relationship [Nix, 1989]:

$$\varepsilon = -\left(\alpha_f - \alpha_s\right)\left(T - T_o\right) = -\Delta\alpha\Delta T$$

where ε is the strain, α's are the thermal expansion coefficients, and T and T_o are the growth and ambient temperatures respectively. One can easily realize that for film-substrate systems where a typical value for the thermal expansion mismatch between film and substrate is 1 ppm/°C, and a typical growth or crystallization temperature for oxides is 650°C, the residual stresses would be 100's of MPa.

Given these potential sources of residual strains, the possibility of a textured microstructure, and the spontaneous strains from the Curie transition, the interpretation and

identification of size effects in thin films may be considerably more involved than for the bulk ceramic system.

Radio frequency (RF) sputtering has by far been the most popular method of producing barium titanate thin films, most likely due to the fact that large ceramic targets are inexpensive and readily available, and that the composition of barium titanate is relatively insensitive to long anneals at growth temperatures of 600 - 700 °C. Many of the researchers included $SrTiO_3$ in their compositions, so these film will be treated as well. Gitel'son *et al.* deposited barium strontium titanate, (BST) films by RF sputtering and determined that a critical film thickness existed for ferroelectricity of approximately 100 nm as judged by the temperature dependence of the dielectric constant. They noticed a diffusion of the maxima of the permittivity with decreasing film thickness, but unlike some other researchers, witnessed no or negligible shift in T_c. This behavior was attributed to the presence of surface layers, interfacial layers, and residual strain. Unfortunately, the reported grain size changed as a function of thickness as well, so it is unclear as to what the appropriate crystal dimension is. Uchino *et al.* also produced barium titanate film by RF sputtering and investigated the size effects by structure measurements via x-ray diffraction. Uchino reported a critical grain size of 120 nm for high temperature deposited films; the grain size was controlled by the deposition temperature [Uchino *et-al*, 1992]. It is interesting to note, however that all films exhibited swelled lattice constants, most likely owing to energetic bombardment during deposition. The observed size effects were attributed to the pre-existing hydrostatic pressure model, and although the critical size was in close agreement to that observed for small particles, the explanation is unlikely since it depends upon surface tension, but ignores significant stresses due to the residual thermal expansion mismatch strains, which would have been tensile for such a system. Such an explanation also cannot account for the swelled lattice, as its volume is considerably larger than even the bulk barium titanate value. Mikami *et al.* again produced RF sputtered films at a variety of substrate temperatures. Their findings, however indicate that the

ferroelectricity of the films depended upon the film morphology, such that as the deposition temperature increased, the morphology changed to columnar, and the permittivity rose. For the columnar films, the permittivity scaled with column height, with column width presumably constant, while for the equiaxed films the permittivity scaled with grain size. This behavior was attributed to the presence of a low K layer at the substrate [Mikami *et al.*, 1990]. Again the presence of residual strain was ignored. In such a system, where grain size is controlled by substrate temperature, the increased levels of strain due to an increased temperature differential between ambient and deposition should not be ignored. Dudkevich *et al.* also produced barium titanate thin films by RF sputtering and studied the size effects, but did so by depositing films of a constant thickness. Deposition parameters such as gas pressure were used to control the microcrystallite size. Dudkevich explained that the morphology changed continuously as the film thickness increased, so measuring size effects as a function of film thickness was unreasonable [Dudkevich *et-al*, 1981]. Specifically, when columnar structures evolve, the coherent crystal length across the column scales with thickness. Noting these coupled parameters, the control variable was the coherent crystal length, which was estimated by the width of the 110 diffraction peak. The size effects were determined by electrical property measurements, including the temperature dependence of the permittivity. As such, the critical sub-crystallite size was determined to be 300 Å, and independent of grain size. Residual stresses are automatically accounted for by this measurement since the coherent lattice size is strongly influenced by strains and crystal defects. The size effects were determined to be due to changes in the lattice vibration spectrum as a function of the distance that a phonon can travel in the lattice previous to being scattered. From their calculations, the critical size for ferroelectric behavior, following their model, would be 50 Å. Differences between their experimental observation and calculations were attributed to constants in the model which assumed isotropy.

Deposition of $BaTiO_3$ from solution precursors has also been experimentally demonstrated. Frey *et al.* deposited very fine grained barium titanate, all of which was below the ferroelectric size limit. They found 25 nm grain barium titanate to be stabilized in the paraelectric state with a dielectric constant stable with temperature [Frey and Payne, 1993]. Hayashi *et al.* also deposited $BaTiO_3$ films by sol-gel methods. Films with 50 nm grains were reported to be ferroelectric with permittivities near 1000. They attributed this lower than bulk value of the dielectric constant to stresses in the film. Minor amounts of ordering were observed in these films, which were deposited on [111] oriented platinum electrodes [Hayashi *et al.*, 1993].

Desu conducted a study of RF diode sputtered films on several substrates at high temperatures in order to study the effects of thermal expansion mismatch and internal stresses on the film's electrical properties. The film stresses were calculated from wafer curvature measurements taken by a scanning laser technique. Two samples were characterized; both were polycrystalline $BaTiO_3$, one deposited on silicon, nearly stress free, while the other on sapphire showed approximately 400 MPa of residual compressive stress. The film on silicon exhibited near bulk properties, while the latter showed a diffuse transition, bulk permittivity values, a remnant polarization of only 3 $\mu C/cm^2$, and a coercive field 17 times greater than observed in the bulk. These unusual values were attributed to pinning of the ferroic domains [Desu *et al.*, 1993]. Whether or not residual stress plays a role in the size effects observed in $BaTiO_3$, these experiments clearly show that their effects on the measured electrical properties cannot be ignored and may make interpretation of size induced transitions very difficult.

1.5.2.2 Epitaxial thin films

An epitaxial growth process may be defined as one in which the crystalline structure of some substrate material is translated into that of the growing film. The result of such a growth process, to a first approximation would be a single crystal film. In reality, however, the condensate will exhibit some degree of mosaic structure. Though grain

boundaries, in the traditional sense, will not be present in the film, low angle boundaries will exist and reflect themselves in the crystal's diffraction patterns. Very often the degree of epitaxy, or the crystalline quality of the film will be judged by the widths of peaks produced by x-ray or electron diffraction.

The most common examples of epitaxial growth may be found in semiconductor junction devices. Such structures typically show extremely good epitaxy, that is, the deposited film possesses a structure very similar to that of a bulk crystal. Many times, homoepitaxy is used to describe these situations where the only difference between the substrate and the layer is small concentrations of dopants which perturb the lattice very little. In oxide systems, the differences between film and substrate are considerably larger. Heteroepitaxy is used to describe these situations where the film and substrate may be very different materials.

The factors which are most important in achieving epitaxy are the lattice constants of the materials, the crystalline structures, and chemical compatibility. Chemical compatibility is a very important consideration since to achieve epitaxy, in most cases, elevated temperatures in the neighborhood of 700°C are required. It is, of course, always desirable to have the film and substrate of the same crystal structure, such as rocksalt, diamond, or perovskite, but more importantly, the oxygen sub-lattice spacings should be very close. In the case of mixed oxide systems, there is nearly always some lattice mismatch which can be accommodated in two ways by the growing film. A coherent system refers to a film/substrate system where both lattices are completely continuous across the interface. In such a case, the lattice misfit is accommodated by simple strain in the film. Such an interface could only occur when the mismatch is very small. The second, and more common type of interface would be labeled incoherent [Smith, D. L., 1995]. This time, the interface is locally coherent, accommodating mismatch with strain, but periodically, a dislocation will nucleate as a strain relief mechanism.

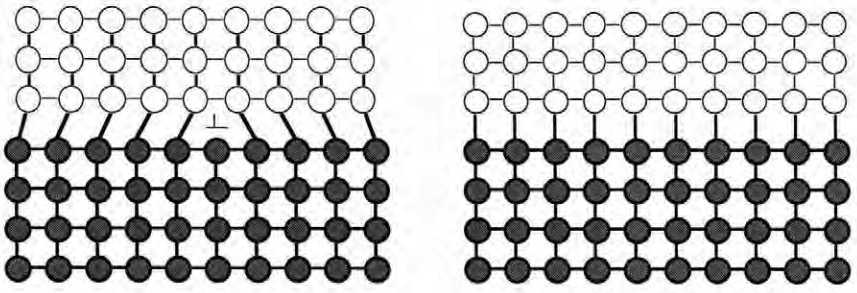

Figure 1.11: Epitaxial interfaces

A specific amount of energy is needed for the nucleation of a thermodynamically stable dislocation, but the favorability of such a dislocation is increased with the level of strain in the film. Since the stress level of the film increases with thickness, for a given growth temperature, a critical thickness for dislocation nucleation is often observed. Following this, it can be seen that a film which initially grows coherently can, upon the nucleation of defects, becomes incoherent [Smith, D. L., 1995].

For a barium titanate thin film deposited at high temperatures, is would appear that the strain associated with epitaxial arrangement would contribute to the already complex mechanical behavior of the system. However, if the growth temperature is large enough, the film can be assumed to grow in a relaxed state, stress free [Nix, 1989].

For high quality epitaxial films, little morphology should be present. That is not to say that the surfaces will be atomically smooth, since films most often grow by island coalescence. The presence of in-plane epitaxy strongly limits the possibility of independent column growth.

High quality epitaxial barium titanate films have been grown by several researchers for the study of size-induced phase transitions. Terauchi *et al.* conducted studies of ultra-thin films of $BaTiO_3$ on $SrTiO_3$ substrates deposited by activated reactive evaporation.

After depositing films between 67 and 1500Å in thickness, a structural study of the epitaxial films was conducted by x-ray diffraction. The initial conclusion of the study was that for the very thin films, the substrate dominated the $BaTiO_3$ structure. Both in and out-of-plane lattice constants were measured by normal and grazing incidence x-ray diffraction respectively. For very thin films, the in-plane constant exactly matched the substrate value, while the out-of-plane constant was measured at 4.15 Å. The large tetragonality was attributed to unrelaxed epitaxial strain. As the films were grown thicker, the substrate-induced tetragonality faded, until cubic films were obtained at thicknesses of 600 and 1500Å. Thicker films were not deposited and no explanation of the cubic barium titanate was given. The same group then went on to deposit $BaTiO_3$ films by the same technique on epitaxial platinum on MgO. Films as thick as 4000Å were grown. Electrical properties for the 4000Å film were given where a P_r of 4.8μC/cm^2, an E_c of 28kV/cm was measured, and a diffuse transition at ~ 135°C was observed. No explanations for these values were given. High temperature x-ray diffraction was reported, but the ferroelectric to paraelectric transition was not observed structurally [Yoneda *et al.*, 1993]. A thickness dependence of the dielectric constant was observed for films on platinum electrodes. The permittivity plateaued for films ~400Å and thicker at a value of ~700, while for the thinnest 100Å film, the permittivity was measured to be ~ 100. The differences were attributed to thickness-induced strain producing an anomalously large dielectric constant in the c direction, but the possibility of twinning with increasing thickness and an averaging of the a and c-axis permittivity values remains unanswered. It was then proposed that the reason the $BaTiO_3$ films on $SrTiO_3$ substrates did not show a transition was that the close lattice match between the two resulted in no misfit dislocations, so the film properties were dominated entirely by the substrate, hence no transition. In contrast, for films on MgO, where the mismatch is approximately double that experienced upon $SrTiO_3$, the transition occurred because sufficient numbers of dislocations nucleated on the substrate, effectively

de-coupling the two. As a result the film properties were not swamped by the substrate and a transition was realized [Yoneda, *et al.*, 1995].

Given the strong interest in DRAM structures, much work has been completed on the BST system and its size effects. Abe *et al.* reported that in BST compositions which in the bulk would be paraelectric, when deposited as epitaxial thin films, showed an induced tetragonality and ferroelectricity. For 2000Å thick films, the out-of-plane lattice constant was larger than the bulk value, and increased with decreasing film thickness, the in-plane constant was not reported. The tetragonality was however assumed to increase with decreasing thickness. Contradicting this observation was the trend of decreasing permittivity and remnant polarization with decreasing thickness. If indeed the substrate induced the tetragonality, then the ferroelectric properties would also be expected to enlarge, assuming that the polarization was switchable. The induced ferroelectricity was attributed to ionic displacements, but the thickness trend was unexplained [Abe and Komatsu, 1994]. Abe as well discussed the unusually large dielectric loss observed in perovskite epitaxial films. The large losses, as compared to polycrystalline films of the same composition was attributed to the lack of grain boundaries. The grain boundaries in polycrystalline films were suspected to act as charge depletion layers [Abe and Komatsu, 1993]. Tabata *et al.* also studied this system by depositing superlattices via laser MBE. The total thickness of their superlattices was kept constant at 2000Å, but the layer periodicity was modified. At the smallest periodicity value of approximately 2 unit cells, the barium titanate was tetragonal with an elongated c-axis and a constricted a-axis. The strontium titanate displayed an elongated a with a constricted c at short periodicities. Both material's lattices approached their bulk values at large layer thicknesses. It was observed that the temperature dependence of the dielectric constant diminished with increased periodicity distances, as did its magnitude at room temperature. The tetragonality and temperature dependence of the dielectric constant at low periodicities was accounted for by assuming a freezing of the soft mode vibrations under the superlattice strains resulting in

"super-dielectric" properties [Tabata *et al.*, 1994]. Tabata *et al.* went on to explain that the critical periodicity values for the observation of anomalous dielectric behavior were between 100 and 1000 Å's. They argue that in this region, the lattice strains may not relax, so tetragonality and dielectric properties are enhanced. As periodicities increase, dislocations nucleate and the lattices relax. At very small periodicities it is argued that the perovskite structures are not complete due to the lack of long range order, therefore the dielectric property values are reduced [Tabata *et al.*, 1994]. Nose *et al.* deposited barium titanate thin films by pulsed laser deposition and found the maximum in the dielectric to be diffuse and shifted to ~150°C. Both of these observations were attributed to the presence of inhomogeneous strain arising from lattice mismatch. Residual strains from thermal expansion mismatch were however ignored in the discussion. Reported also was the presence of the tetragonal to orthorhombic transition. The orthorhombic transition was found to be displaced to a lower temperature [Nose *et al.*, 1994].

Though currently, no large scale processes make use of $BaTiO_3$ thin films, several attractive applications exist. It is very likely that in the future $BaTiO_3$ will be incorporated into non-volatile memory elements a well as electro optic devices. In both of these applications the required size for the $BaTiO_3$ element would be quite small, certainly encroaching the regime where intrinsic size effects would be observed. If $BaTiO_3$ is to be used is such ways, a thorough understanding these anomalies would be required.

Chapter 2

EXPERIMENTAL PROCEDURE

2.1 Vacuum system

A high vacuum chamber designed by Maffei (1993) for pulsed laser deposition of oxide thin films was used in this study. Before deposition of barium titanate thin films, several improvements to the system were necessary. Initially, a thorough cleaning and leak inspection was performed, a new target rotation mechanism was designed and installed, and a high temperature substrate furnace enabling epitaxial growth was added. Midway through the study, an ozone generator capable of 8% ozone in a molecular oxygen balance was installed.

2.1.1 Vacuum chamber

All thin film samples used in this study were deposited in a high vacuum chamber with a base pressure of 8.0×10^{-8} Torr manufactured by Huntington laboratories (see figure 2.1). The system was pumped by a Varian model M6 diffusion pump running with Corning Si-70 silicone oil. Though equipped with a liquid nitrogen trap, use of this oil allowed the base pressure to be achieved without capture pumping. Deposition of oxide films in the presence of ozone also inhibited use of the liquid nitrogen trap as liquid ozone would condense on the cold trap surface, resulting in an explosion hazard. The diffusion pump had a pumping speed of 1200 l/s. The deposition system was backed and roughed with an Alcatel model 2033CP+ rotary pump operating at 33 cubic feet per minute (cfm). The rotary pump was filled with a fluorinated polymer oil to protect against oxidation by ozone. Separating the growth chamber from the high vacuum pump was an MDC Vacuum Products manual gate valve.

Three gauges were incorporated into the system for pressure maintenance. In the low vacuum regime convectron gages measured pressures in both the growth chamber and the backing lines, while in the high vacuum range, a Bayard-Alpert ion gauge with a

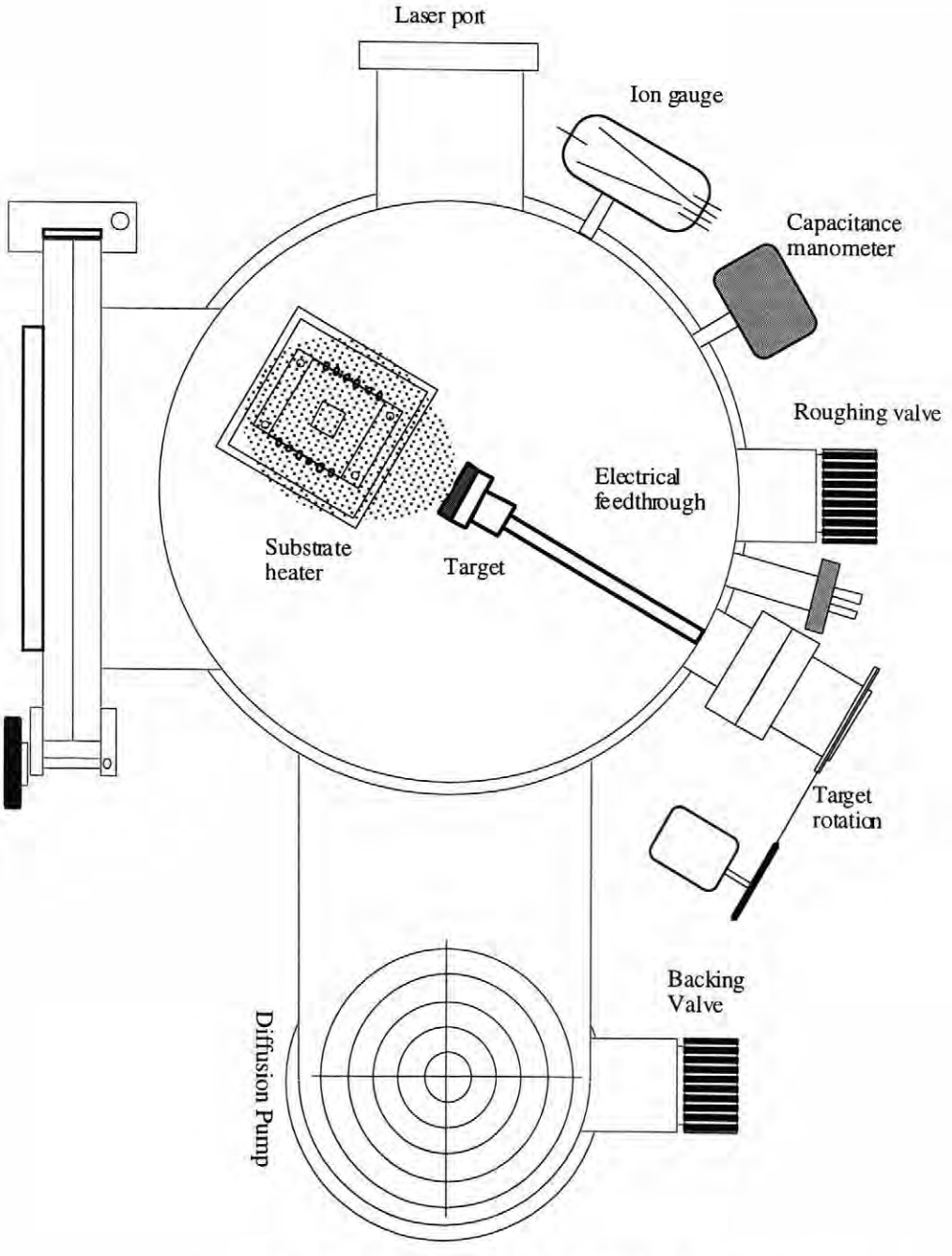

Figure 2.1: PSU MRL PLD chamber schematic

thoriated iridium filament was used. Given the low accuracy of convectron gauges in the medium vacuum range where laser ablated films are grown, a capacitance manometer (1 Torr full scale) from MKS instruments was added to the chamber. With this style of gauge, an accuracy of 1% in the measured pressure value was enabled, with the measured pressure independent of the ambient.

2.1.2 Gas delivery

When materials were deposited in either molecular oxygen or argon ambients, the gas flow into the chamber was introduced via mass flow control devices from MKS instruments. When the ozone/oxygen mix was desired, mass flow controllers were inappropriate due to seals which would degrade in the presence of this powerful oxidant. In order to introduce the appropriate amounts of ozone/oxygen mix accurately and reproducibly in to the chamber, the gas mix was bled through an all stainless welded seal bellows micro-metering valve from Nupro Products. The precise construction of this valve allowed small flow rate values to be achieved with stability near that of a mass flow controller. All gasses were introduced into the growth chamber 9 inches away from the substrate.

Ozone was supplied by a PCI-G1 ozone generator capable of producing a mixture of 8% ozone with a balance of molecular oxygen. The ozone generator contains an ozonator cell and a high frequency inverter for ozone production. The gas is produced by passing dry oxygen between a silver plated glass and a stainless steel electrode, between which a high frequency a.c. 8,000 volt potential is maintained. The ozone generator cell was operated at 15 psi for maximum operating efficiency, requiring a 5 cfm minimum throughput. Since the output from the generator was much larger than the necessary amount bled into the chamber, a T-style fitting was placed on the output line from the generator with one side venting directly to the chamber and the other to the building exhaust. Between the "T" and the chamber, an all stainless check valve was located in order to prevent backstreaming from the building exhaust. Before the bulk of the ozone

mix was introduced into the building exhaust, it was passed through an ozone destroyer consisting of a stainless steel canister filled with zeolite pellets.

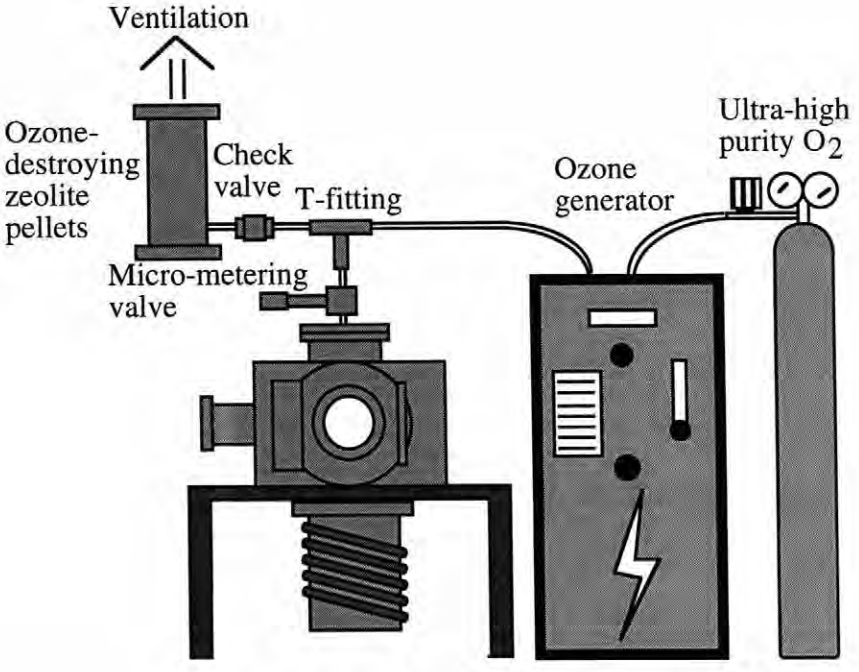

Figure 2.2: Ozone delivery schematic

Interaction of the ozone with the massive surface area of the zeolite resulted in sufficient gas/surface collisions to decompose the ozone into molecular oxygen.

2.1.3 Substrate heating

In order to deposit epitaxial oxide films, the substrates needed to be elevated to temperatures in excess of 700°C. To accomplish this, a block style heater wound with a resistive element was designed and fabricated.

The block heater was constructed from type 304 stainless steel stock. Type 304 stainless was chosen for its oxidation resistance at high temperatures and its low concentration of molybdenum (which forms a volatile oxide at elevated temperatures in the

presence of oxygen). The size of the uniform hot zone on the heater surface was approximately 6.5 cm^2. By examination of the surface with an optical pyrometer the temperature uniformity was confirmed. The hot portions of the heater were designed purposely small in order to minimize radiative losses. Minimizing heat transfer from the block resulted in lower watt density requirements from the resistive element, increasing lifetime and maximum operating temperature. This block had a practical maximum temperature of 750°C, at which point the uninsulated lead ends were within 100°C of the manufacturer's suggested maximum temperature of 1000°C. Thermocoax, the resistive heating element purchased through Phillips electronics, consisted of a nickel-chrome alloy wire surrounded by fine grained magnesia powder, the two of which being swaged into an inconel jacket. The diameter of the element was 1.5 mm. The element was strung through the block 14 times. By winding the block very densely, the watt density necessary from the element was kept to less than 200 W/linear cm. Figure 2.3 provides a schematic of the heater block.

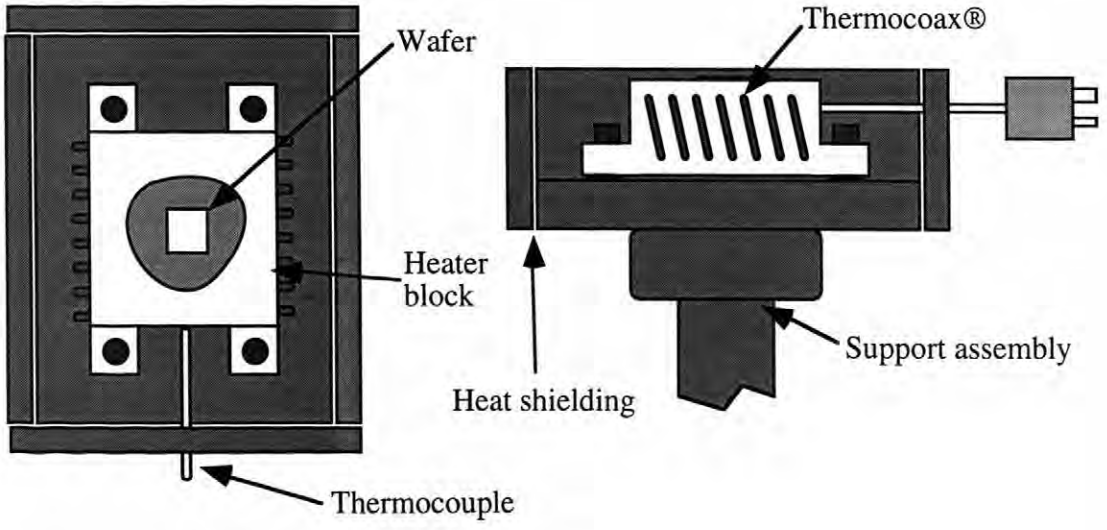

Figure 2.3: Substrate heater

Electricity was supplied to the heater through a Hewlett Packard direct current power supply. Typical power consumption of the heater at temperatures near 650°C was ~120 watts (20 volts and 6 amps).

To insure good thermal contact between sample and heater, the oxide wafers were mounted with silver paint. Previous investigators have shown that by bonding the substrate to the block with a conductive medium, a temperature difference of about 5 degrees is maintained between the block and wafer. The deposition temperatures given refer to values measured with an inconel sheathed K-type thermocouple imbedded into the stainless steel block. During the deposition of emissive materials such as $SrRuO_3$, the temperature of the block would drop during the deposition, and needed to be compensated by supplying more power.

2.1.4 Target rotation

Polycrystalline targets 1" in diameter were used as the film source material. Barium titanate and strontium ruthenate targets were purchased from Target Materials Incorporated. Both materials were 98% dense and 99.99% pure. Targets were refaced after each deposition using aluminum oxide abrasive paper, rinsed with isopropanol, and blown dry with compressed dry nitrogen. The targets were mounted onto stainless steel holders with commercially available nickel print. The freshly mounted targets were placed in a 150°C drying oven for 20 minutes prior to installation to insure complete solvent removal.

2.2 Substrates

Four substrate materials were used for this study; MgO, $SrTiO_3$, $LaAlO_3$, and LiF. The MgO and LiF were purchase from Commercial Crystal Labs, the $LaAlO_3$ from AT&T, and the $SrTiO_3$ from Marketech International. All substrates were [001] oriented with miscuts averaging ~ 0.5°. Using the following procedure, all substrates were cleaned prior to deposition:

5 min sonication in Microclean all purpose laboratory cleaner (Fisher Scientific),

5 min. sonication in deionized water,

5 min. sonication in acetone,

5 min. sonication in ethanol,

5 min. sonication in isopropanol,

Dry with compressed nitrogen jet,

2.3 Excimer laser

The laser used in this study was a 1986 model EMG-150 excimer laser from Lambda Physik Incorporated. The laser was run with a krypton fluorine gas mixture which emits radiation in the ultraviolet at 248 nm upon excitation from a short duration voltage discharge. The laser was a two stage model with oscillator and amplifier tubes. The oscillator tube provides a seed pulse of approximately 100 mJ that is passed to a second tube which amplifies the beam to a maximum energy of about 800 mJ. The pulse length is 30 ns, with a maximum repetition rate of 25 Hz [Lambda Physik, Acton Mass.]. The spatial and temporal distributions of the beam were both near gaussian, which made accurate energy density measurements difficult. The beam also had considerable divergence, so an aluminum aperture was placed at the beam exit such that after diverging, the entire beam fit through the optics components. Cutting down the beam size also served to exclude lower energy density portions of the beam, giving a more uniform beam profile at the expense of reduced fluence.

The laser was operated using both neon and helium as the buffer gas. The laser operated with similar power output using both gasses, but the gas lifetime using neon was about twice that of helium.

2.4 Laser optics

In order to introduce the laser beam into the chamber, a 2 inch diameter Suprasil [Heraeus Inc.] fused quartz window was mounted to a chamber flange by means of an O-ring seal. This allowed for complete removal of the window for thorough cleaning. Though the window was greater than 15 inches from the target surface, on it were deposited significant amounts of ablatant. The window was periodically cleaned by etching with 30% concentrated nitric acid. To focus the laser beam and subsequently control the energy density at the target surface, a plano-convex fused quartz lens was used. Accounting for reflection and absorption losses, the optics train of the system operated with a 76% calculated efficiency.

The laser was focused onto the target at an incident angle of 60°, with the laser spot size having a minimum area of ~ $1mm^2$ at maximum focus. The spot size was determined by measuring the dimensions of the area on the targets which darkened after a laser incidence. In doing so, it was found that for the same laser lens configuration, the spot size was different for different target materials. Since the laser beam had a spatial flux distribution, and different materials have different thresholds of ablation, it was concluded that the lower the target ablation threshold, the larger the effective laser spot size. The laser pulse energy was measured with silicon energy meter allowing individual pulse energies to be determined. The pulse-to-pulse energy variations were within the manufacturer's specifications of 10 %.

2.5 Deposition of barium titanate films

Barium titanate films as well as epitaxial bottom electrodes were deposited in both the on and off-axis deposition geometry; the substrate heater could be rotated 90° to accommodate both. In the on-axis geometry, the substrate face and the target face are parallel, while in the off-axis geometry they are perpendicular. After thoroughly cleaning the substrates with the above mentioned process, the wafers were fixed to the block heater

using silver paint. Several drops of silver paint were placed on the heater surface onto which the wafer was placed. The paint was allowed to dry for about 5 minutes, then the heater was placed in the chamber. Under atmospheric conditions, the heater was turned on and a temperature of 100°C was reached. At this temperature, the wafer was allowed to sit for 5 minutes. By doing this, all of the solvent was extracted from the paint, leaving no pockets trapped beneath. Following this step, the chamber was pumped down to ~ 5 x 10^{-6} Torr prior to deposition. For the first layer of deposition, the chamber was pumped with the heater on, but for second layer depositions, the chamber was evacuated and filled with the appropriate amount of gas prior to heating. The correct deposition pressure was achieved by first establishing a flow rate, typically 100 sccm, then throttling the gate valve, effectively lowering the system conductance. The targets were rotated at a rate of 1 Hz while the laser was typically pulsed at a rate between 5 and 10 Hz. After completion of the deposition, the chamber was flooded with the ozone/oxygen mixture to a pressure of 100 Torr, at which point, the heater was shut off. The film was then allowed to cool to a temperature below 200°C then removed from the chamber. The substrates were removed from the heater by gently prying with a sharp razor. The substrate heater was sanded clean after each deposition.

When film masking was necessary, a thin glass slide was placed on top of the area desired. The masks could not be simply rested upon the substrates in the off-axis geometry since the high local pressures imposed by the plasma would displace them. In these cases, the masks were held fast with a steel weight.

Thickness and roughness measurements on the laser ablated films were made with an Alpha-step 2000 surface profilometer with a 25 μm diamond tip.

2.6 Structural characterization

The crystallinity of the barium titanate films was measured with a Picker 4-circle x-ray diffractometer utilizing $Cu_{K\alpha}$ radiation, an incident beam graphite monochromator, and

a scintillator crystal detector. The tube was driven at 1200 watts, and scans were taken stepwise, typically using 0.1° steps, counting for 5 seconds at each. The diffractometer was controlled by a workstation running "super" which commanded the stepper motors for each circle. The two-theta, omega, phi, and chi circles had the following angular resolutions respectively; 0.15°, 0.24°, 0.35°, and 1.8°. The angular resolutions of the 4 circles and the beam alignment were determined by measuring silicon single crystals.

2.7 Morphological characterization

The surface morphology of the laser deposited films was characterized by optical microscopy. A Reichert-Jung Polyvar Met optical microscope with a Nomarski interference microscopy attachment was used to investigate the films. The microscope had a maximum magnification of 3,000x, making lateral features such as boulders or macroparticles readily visible. Using the Nomarski attachment, the vertical resolution was ~100Å, allowing fine surface morphology to be investigated.

2.8 Compositional characterization

Two methods of characterization were employed to determine the stoichiometry of the barium titanate films. Rutherford backscattering spectroscopy was performed on the films at the University of Arizona's Department of Physics, while absorption spectroscopy was performed in-house using a dc plasma emission spectrometer. A hydrofluoric acid solution was used to dissolve the barium titanate films for DCP measurements.

2.9 Electrical property measurements

The electrical properties of the laser deposited barium titanate films were made by measurement of tiny capacitors deposited by a combination of laser ablation and sputtering as seen in figure 2.4.

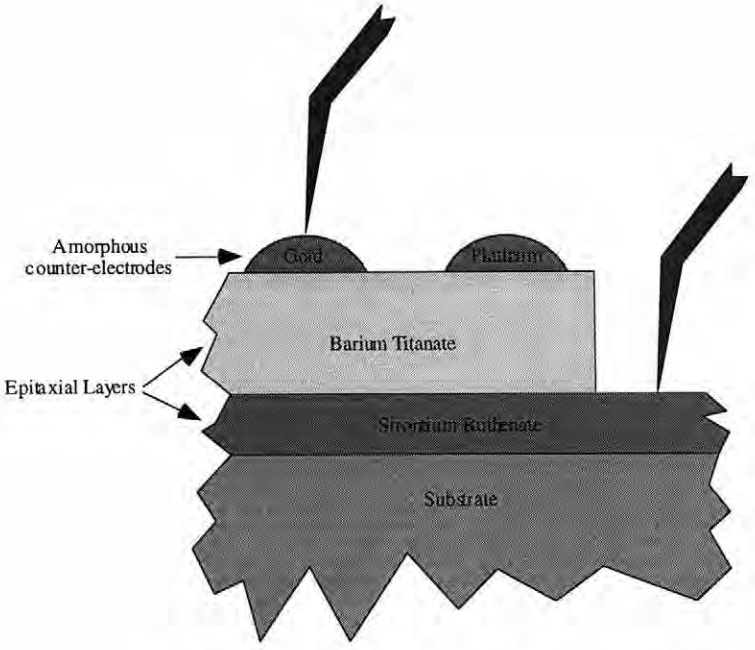

Figure 2.4: Schematic of thin film capacitors

Epitaxial strontium ruthenate was deposited on polished substrates as a conductive oxide bottom electrode, on top of this, the epitaxial barium titanate layer was next deposited. Both epitaxial layers were grown by pulsed laser deposition. The top counter electrodes which completed the capacitor structure were either gold or platinum, deposited through a metal shadow mask. The area of the top electrodes was 0.00114 cm^2. The gold was deposited by d.c. magnetron sputtering and the platinum by pulsed laser deposition. Both metal top electrodes were grown at room temperature.

Ferroelectric properties were measured with an RT66A standard ferroelectric test apparatus [Radiant Technologies]. Using this apparatus and a pair of point probes, hysteresis, resistivity, and leakage current were measured. The RT66A was capable of applying a maximum of 20.0 volts. When masking at high temperatures and gas pressures was too complicated, a portion of the bottom electrode was revealed by etching. A 30% concentrated solution of HF in water proved effective in removing the barium titanate layer, while leaving the strontium ruthenate undamaged.

Capacitance and dielectric loss were measured using a Hewlett Packard LCR bridge, model 4274A. The temperature dependence of these properties were measured using the same bridge in conjunction with an in-house designed convection oven with a temperature range of -175°C to 270°C. For these measurements point probes proved insufficient, so films were mounted and aluminum wire bonded to 16 pin chip carriers.

Chapter 3

Deposition Parameter Study

The spatial distribution of the ablated material is very sensitive to laser spot size, gas pressure, the target to substrate distance and the geometry of substrate holder. When all parameters were adjusted properly in the on-axis geometry, films with thickness uniform regions one inch in diameter were deposited.

The thickness uniformity study was performed by depositing strontium ruthenate at room temperature onto rectangular glass slides. Strontium ruthenate was chosen for its optical opacity, which rendered films deposited on transparent substrates easily observable and measurable. Measurements of thickness were made with a mechanical profilometer (Alpha-step 2000) with 25 Å resolution. The thickness study was performed in both the on and off-axis deposition geometries.

3.1 On-axis deposition

The first parameter investigated in the study of thicknesses uniformity in on-axis deposited laser ablated films was pressure. At a constant target to substrate separation distance of 7.5 cm, amorphous-$SrRuO_3$ (a-SRO) was deposited at a laser repetition rate of 10 Hz for ten minutes with a constant laser intensity of 225 mJ/pulse and a spot size of ~ 8 mm^2. The pressure values used were vacuum (~10^{-6} Torr), 10 mTorr, 50 mTorr, 100 mTorr, 200 mTorr, and 250 mTorr ozone/oxygen mix.

Substrates consisted of 1" by 1.5" standard microscope slides which were cleaned using the previously described 5 step process. The substrates were masked around all edges using a permanent marker to facilitate thickness measurements. After deposition, the mask material was removed by soaking in acetone.

After deposition and thickness distribution measurement, it was found that the maximum amount of material deposited, for these deposition parameters, occurred between 100 and 50 mTorr background pressure. The distribution of thickness laterally across the substrate varied by approximately a factor of 2 in all cases with the exception of deposition in vacuum, where the gradient was larger.

Clearly, a maxima exists for film thickness when deposited as a function of deposition pressure. This can be attributed to the two components of the laser plasma, their relative energies, and the rates at which they exit the target surface. To explain this activity, consider the three following cases: deposition at high pressures ~ 250 mTorr, medium pressures ~ 50 mTorr, and vacuum ($< 10^{-6}$ Torr). Consider also that the plume is known to consist of two components (i), a higher energy ablated portion which expands following a $\cos^n\theta$ distribution and (ii), a lower energy thermally evaporated portion which expands in a less directed distribution [Chrisey and Hubler, 1994].

At any pressure, before scattering or thermalization occurs, the energies of ablated plume species range from tens to thousands of electron volts. The typical plume temperature , as measured by emission spectroscopy has been reported to be in excess of 10,000 K [Chrisey and Hubler, 1994]. In vacuum, as the ablated and evaporated material exits the target surface it travels largely uninhibited, with the exception of inter-plume species collisions. As such, material expands in both the forward and radial directions. The expansion in this and all other cases is governed by pressure gradients.

Consider next the medium pressure case of ~ 50 mTorr. At these pressures, the visible portion of the plume is dramatically reduced in size owing to confinement by the background gas. When deposition in the presence of a background gas is imaged by ICCD photography, a shock front evolving normally to the target surface is found [Goehegan, 1992]. This shock front has been explained by a "snowplow" model which will be used by the current authors to explain the maximum in deposition rate with pressure. The "snowplow" model proposes that when deposition occurs in a gas ambient, the energetic

ablated material, initially travelling at supersonic speeds, acts as a plow, effectively pushing the gas forward, leaving in its wake a region of lower pressure than that of the original ambient. This occurs very rapidly due to the large kinetic energies of the ablated matter. Effectively, the evaporated portion of the plasma has not yet left the target surface by the time that the shock front has formed. When the evaporated material leaves the target, as before, its travel will be determined by local pressure gradients. If the pressure immediately in front of the target is smaller than the pressure to the sides, the material will effectively be radially confined as it will choose to propagate in the path of least resistance; normal to the target. Eventually, the evaporated material catches up to the shock front, by which time, under standard ablation conditions, the substrate is nearly reached. In addition to the effective confinement of the evaporated component, the distribution of the ablated component, hence the shockfront, narrows as the pressure increases [Geohegan, 1992]. It is believed that the snowplow becomes more pointed for the same reason as does the evaporant. The portions of the plume which are travelling with a lower velocity eventually fall behind the leading edge of the shockfront hence their resulting lateral expansion is suppressed and the spatial distribution narrows.

When compared to deposition in vacuum, at the plane of the substrate, nearly the same amount of material will pass at 50 mTorr, but the areal density of ablated material is considerably larger due to the lateral confinement, (or similarly, the preferred forward propagation). In vacuum more material will assume a path which will miss the substrate entirely, hence the effective deposition rate increases even though the amount of material removed per pulse is the same.

If the ambient pressures are increased to a large enough value, ~ 250 mTorr, the effective deposition rate is observed to drop. This drop is largely attributed to thermalization of the ejecta resulting in significant reduction of kinetic energy which can be explained by gas phase scattering. The mean free path, (MFP) of a particle in thermal equilibrium with the background gas at 250 mTorr is less than 0.5 mm, so after traveling a

target to substrate separation distance of ~ 5 cm, > 100 collisions would be expected. However, to accurately describe the scattering of ablated, or energetic particles, the kinetic energy must be considered. To do this, the interaction of the particles with the ambient gas is expressed in terms of an effective scattering cross section. Previous investigators [Kurogi et al., 1996] have measured the energy of ablated Ti from PZT ceramic targets and, under similar deposition conditions, reported energy values of ~ 20 eV. It is known that sputtered particles with energies in the range of 10 - 100 eV have an elastic scattering cross section considerably smaller than that of the same particle in thermal equillibrium with the gas [Robinson, 1978]. Robinson also found that in the case of energetic argon in argon ambient, the collision cross section dropped tenfold as the energy of the energetic argon was increased from 0.1 to 1000 eV. Given the approximation that metal atoms scatter similarly to noble gases, a better estimation of the mean free path of laser ablated atoms would be made [Somekh, 1984]. For 20 eV particles, the effective cross section would be reduced by a factor of three [Robinson, 1978]. Given the inversely proportional relationship between MFP and scattering cross section, the effective MFP would now be 1.5 mm. In such a case, is not surprising to expect that much of the material leaving the target either lacks sufficient kinetic energy to reach the film, scatters in a direction which does not intersect the substrate, or redeposits on the target surface as ~ 33 collisions would still be experienced by the molecule. In each case, the effect is to reduce the amount of material, or the areal density of ablatant crossing the plane of the substrate. The result is a drop in the effective deposition rate. The shock front still forms at high pressures, but the point at which the ablated and evaporated material

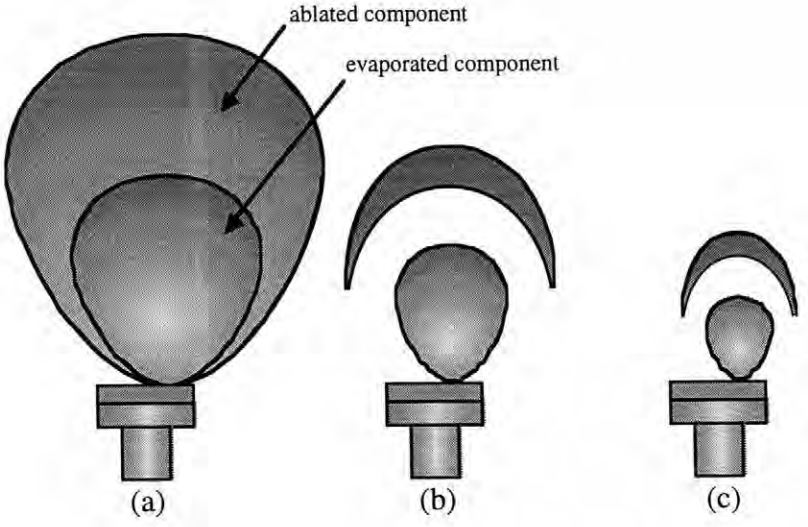

Figure 3.1 Plume behavior as a function of background pressure
(a) ~ 10-6 Torr, (b) ~ 50 mTorr, (c) ~ 250 mTorr

recombines is still a significant distance from the substrate (~ 2 cm @ 100 mTorr) [Geohegan, 1992]. Considerable scattering will occur before the substrate is reached.

Since the a-SRO films were deposited at low temperatures, the evolution of a thin film microstructure was expected to follow the predictions for the low adatom mobility case. The observed morphologies in the a-SRO films were found to be strongly coupled to the background pressure, as was the deposition rate. Very similar to trends observed during sputtering, in laser ablation, the deposition pressure limits the kinetic energy of the advancing plume particles through scattering and thermalization, reducing energetic bombardment. The result of this activity was easily observed by comparison of the films' surface roughness, which was measured mechanically by profilometry. 80 μm scans were performed and an rms surface roughness value was recorded for films deposited at each pressure value. Figure 3.2 shows the pressure dependence of film surface roughness.

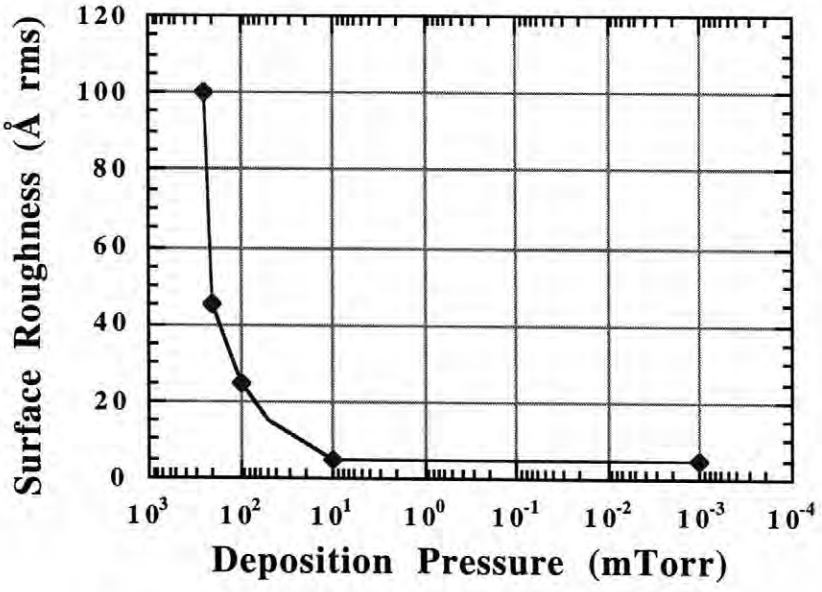

Figure 3.2: a-SRO surface roughness pressure dependence

The surface roughness was also observed by imaging with an optical microscope. When imaged in plan view, film surfaces show a columnar microstructure characterized by dome-like protrusions. The film surfaces were found to become smoother and contrast free as the deposition pressure decreased. These observations, in addition to those obtained by profilometry are easily explained by the structure-zone model which links film microstructure to energetic bombardment and temperature [Messier, 1985]. The additional energy from the incoming species provided by momentum transfer to the film adatoms helps produce smooth homogeneous structures for low pressure depositions where gas phase scattering is rare. At higher pressures where the vapor species undergo multiple collisions prior to deposition, incident atoms have much less kinetic energy to impart to the growing film. Figure 3.3 shows the surface microstructure comparison for films grown at the lowest and highest pressures.

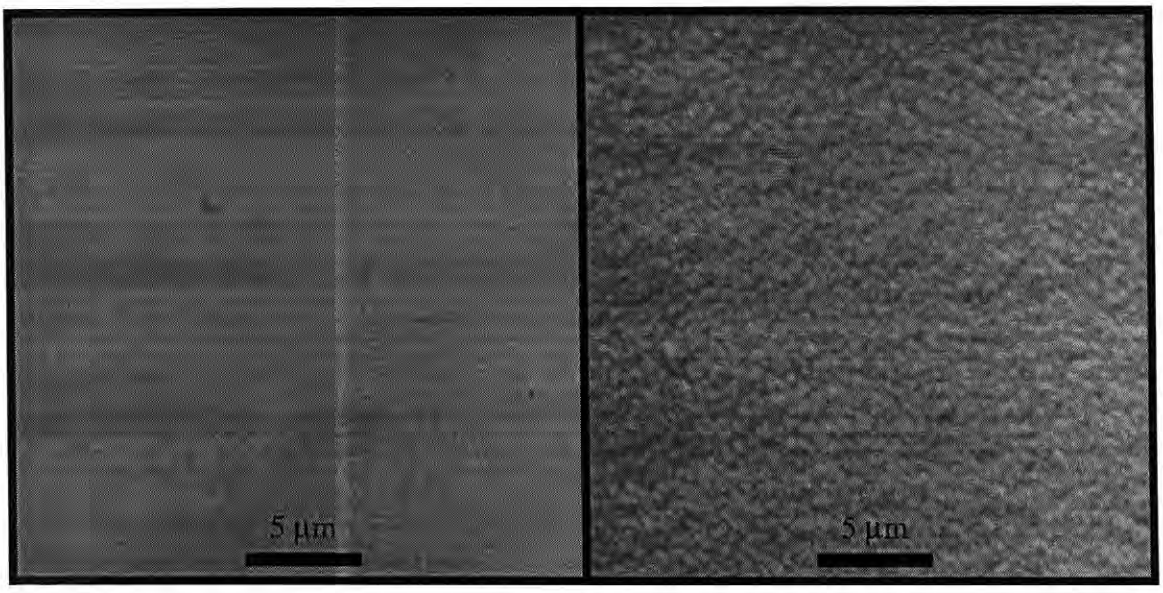

Figure 3.3: Microstructural comparison between films deposited at (a) 250 mTorr and (b) vacuum

For the on-axis case, the effects of target to substrate distance at a constant pressure were also measured. In the case of mixed oxide thin films, a featureless microstructure is most often desired for optimization of optical and electrical properties. For the fulfillment of this prerequisite low pressures would be most often desired during deposition. However, insurance of complete cation oxidation is equally important, suggesting that deposition pressures should be as large as possible. For these reasons a pressure of 50 mTorr was chosen, since it offered an acceptable balance between morphology and oxygen stoichiometry. a-SRO films were deposited under the same conditions as above, but at a constant pressure of 50 mTorr, and at variable target to substrate distances; figure 3.4 illustrates the results.

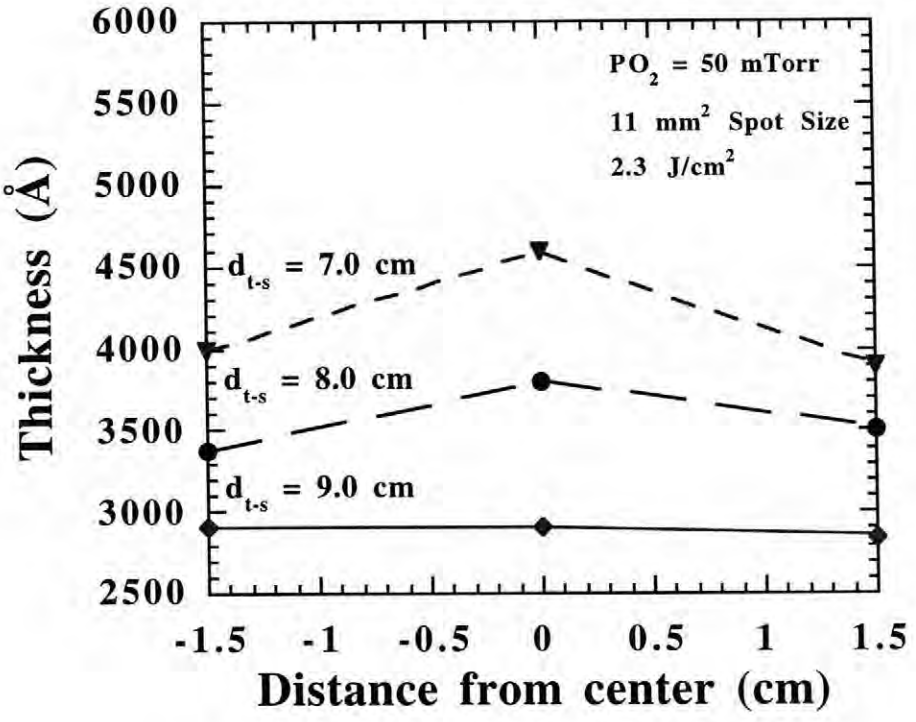

Figure 3.4: Thickness distribution of film as a function of target to substrate distance

The above figure clearly shows that the uniformity of the film thickness improves as the target to substrate distance increases. At a separation distance of 9 cm, the thickness uniformity was similar to the sensitivity of the profilometer. At closer distances the distribution rapidly degenerated; however, the deposition rate rose sharply. Distances greater than 9 cm were not investigated due to geometrical limitations of the chamber.

In all of the above cases the substrates were mounted upon an aluminum block considerably larger than the substrate. Under such conditions, large scale uniformity was possible. When, however, the substrate was mounted on a holder which was smaller than it, the thickness uniformity was considerably poorer, and in every case, limited by the substrate's physical dimension. In the case where an irregularly shaped substrate without a

large backing plate was used, thickness variations always occurred, as evidenced by several optical interference fringes running parallel to the substrate edges. If an identical substrate was fixed to a much larger flat plate and the same amount of material was deposited, the film would be of uniform thickness as judged by the absence of optical interference fringes. If very large substrates were used, uniform thickness regions 1" to 1.5" in dimension were possible. Beyond these dimensions, the thickness rapidly decreased. Slightly elliptical thickness fringes were observed in these cases, where the long axis of the ellipse was parallel to the long axis of the rectangular beam.

These observations indicate that the laser-induced plasma exhibited turbulent flow where the characteristics change dramatically at physical discontinuities such as substrate holders or other chamber fixtures. This would suggest that the pressure in the vicinity of the plasma is larger than the average chamber pressure of ~50 mTorr, at which laminar flow would be expected. Such an observation is consistent with the explanation of the enormous deposition rates achieved by laser ablation. If growth occurs at 1 Å/laser pulse and the plume lifetime is on the order of microseconds, than the instantaneous deposition rate would be in the neighborhood of 1,000-10,000 Å/s. Such a rate would require a large local vapor pressure in the vicinity of the substrate in order to supply such quantities of material.

3.2 Off-axis thickness distribution study

Off-axis deposition by laser ablation has the very positive benefit of significant reduction of boulder densities, but the ability to produce films with uniform thickness distributions over large areas is limited. For most applications, thickness uniformities of $\geq 5\%$ are unacceptable, so the application of off-axis deposition is seldom reported. As in the case for 90° off-axis sputtering, in off-axis ablation, the degree of energetic bombardment is significantly reduced. This can be favorable when depositing on sensitive substrates, but without bombardment, the morphology of thick off-axis grown films suffers.

Substrates consisted of 1" by 1.5" standard microscope slides which were cleaned using the previously described 5 step process. The substrates were masked around all edges using a permanent marker to facilitate thickness measurements. After deposition, the mask material was removed by soaking in acetone.

a-SRO was deposited for 10 minutes at a laser repetition rate of 10 Hz, a pulse energy of 225 mJ, and a spot size of 8 mm^2. The substrate was positioned such that its front edge was 3.5 cm from the target face. Identical experimental conditions were used for all films with the exception of the gas pressure, which ranged from 10 to 175 mTorr.

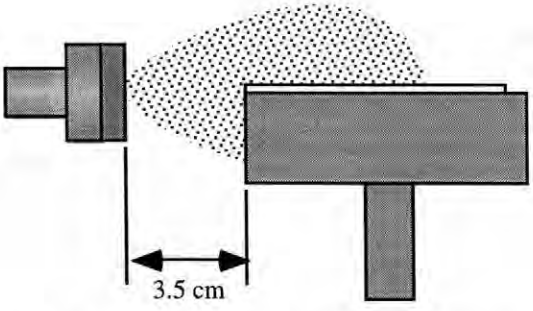

Figure 3.5: Schematic of off-axis ablation arrangement

Figure 3.6 summarizes the results of the off-axis deposition experiments. From this plot of thickness, as measured with a mechanical profilometer, as a function of distance from the substrate front edge, it can be seen that no region or plateau of uniform thickness exists; the thickness of the ablatant decreases monotonically with distance. It is not clear whether the degree of non-uniformity decreases as the target to substrate distance increased due to the fact that the influence of the substrate holder on the material transport is unknown. To determine this, a second set of experiments would need to be performed where the entire substrate holder assembly were moved in and out of the plume.

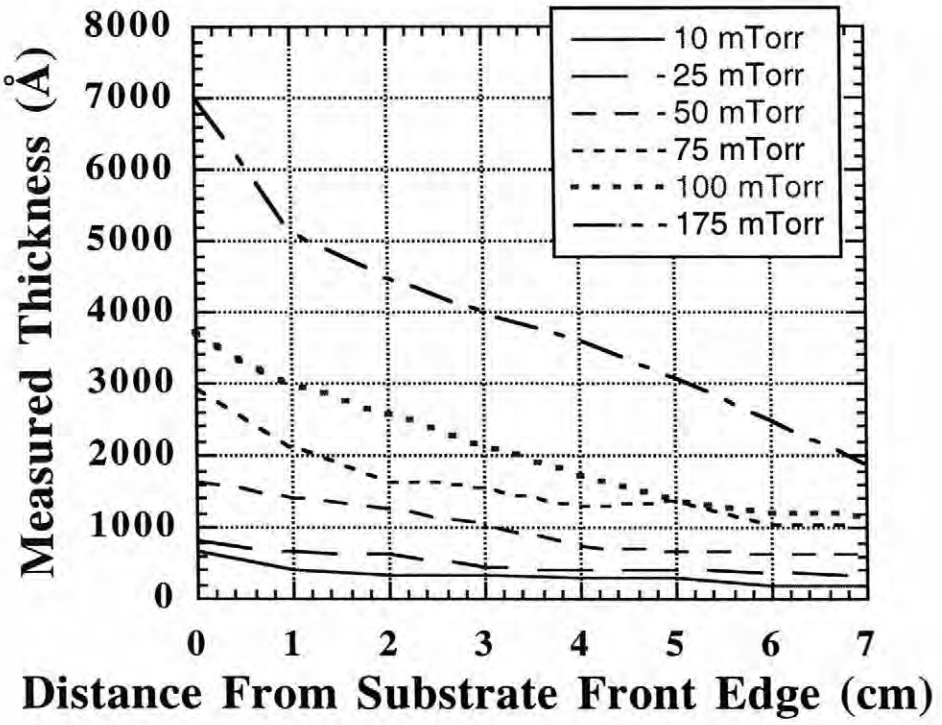

Figure 3.6: Off axis thickness distribution as a function of distance from target face for different background gas pressures

The difference in total thickness with deposition pressure is quite dramatic. At the front of the substrate, the film deposited at 175 mTorr was 7 times thicker than that deposited at 10 mTorr. For the off-axis geometry, assuming that the amount of material removed by each laser strike is independent of background pressure, the action of the background gas must be to scatter the ablatant in such a way as to confine it into an envelope evolving normal to the target surface. A maximum in film thickness at some critical pressure was not observed in the off-axis geometry. This is most likely because the front of the substrate was only 3.5 cm from the target, and the pressure required to impede the forward progression of the ablatant from traveling 3.5 cm would undoubtedly be

considerably larger than for the on-axis case where the separation was nearly 3 times greater.

From figure 3.6 it would appear that the lower pressure deposited films have a greater thickness uniformity, but upon replotting the same data on a thickness normalized scale, figure 3.7, one finds that the relative distribution of ablatant is largely independent of background pressure. This representation of the data indicates more clearly that for films deposited in the off axis geometry, a considerable thickness gradient will exist over relatively short distances.

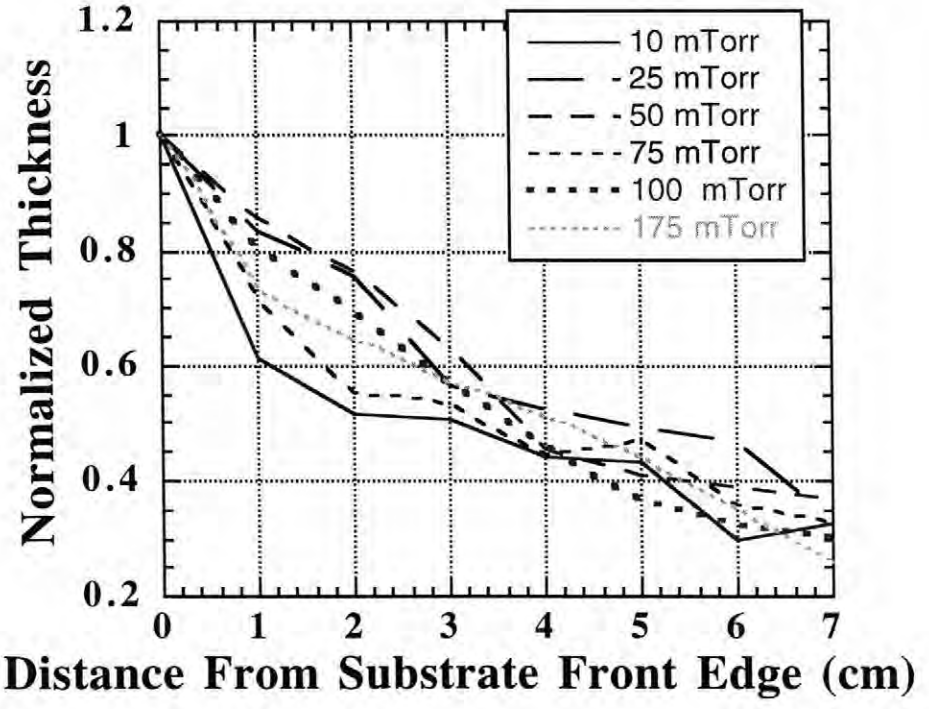

Figure 3.7: Normalized thickness distribution as a function of distance from target

An unexpected result of these experiments was that the position or size of the visible or luminous portion of the plume did not correspond to the position of greatest

thickness. At the highest pressures where the thickest films were observed, the plume was the smallest, barely contacting the very front edge of the substrate. At medium pressure conditions, ~50 mTorr, where the plume was the largest and encompassed most of the substrate, significantly thinner films resulted. If it is assumed that the deposited species consist of ions neutrals, clusters, and molecules which come from the target, then transitions or reactions in the gas ambient, rather than target material, may be responsible for the visible plume since it is not spatially coincident with the thickest sections of the film.

Chapter 4

Epitaxial deposition and optimization of $BaTiO_3$ films

4.1 $BaTiO_3$ deposition on magnesium oxide

Magnesium oxide is a common substrate choice for the deposition of mixed oxide materials. The popularity of magnesium oxide stems from its lattice match with many titanates and cuprates, as well as its availability and low cost. The surface of magnesium oxide crystals can however be quite rough owing to surface steps and supersteps which are commonly found on epipolished crystals [Norton and Carter, 1990]. These surface steps, though detrimental to many device-oriented applications, are beneficial for the achievement of epitaxy as they tend to provide prealigned nucleation sites for the condensing vapor. The refractoriness and chemical stability of MgO have also led to its popularity.

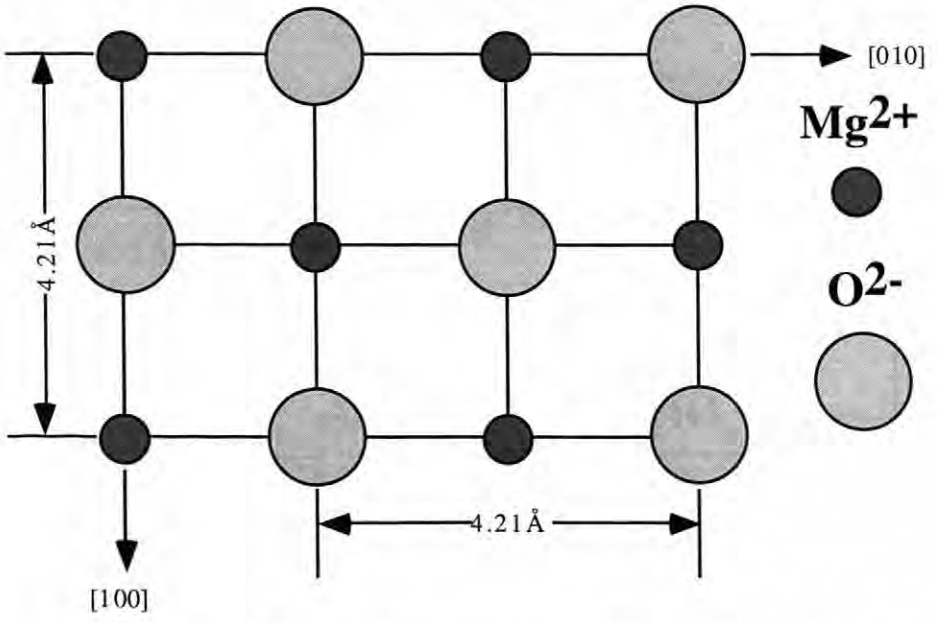

Figure 4.1: (001) surface schematic of magnesium oxide

MgO possesses the rock salt structure which consists of two interleaved face centered cubic sublattices of oxygen and magnesium ions. The most common growth surface of MgO is the (001) plane, which is shown in figure 4.1.

The thermal expansion of behavior of MgO as a function of temperature is shown in figure 4.2. The thermal expansion coefficient of MgO is larger than that of $BaTiO_3$ over the temperature range of interest (RT - 700°C). As would be expected, when deposited at elevated temperatures, c-oriented $BaTiO_3$ grows epitaxially on the MgO {001} plane. For a c-axis oriented film at room temperature, the lattice mismatch between the two structures is 5.4% relative to the barium titanate bulk lattice. As described by Norton and Carter (1990), it is likely that significant concentrations of dislocations are formed at the interface during growth to relieve much of this strain.

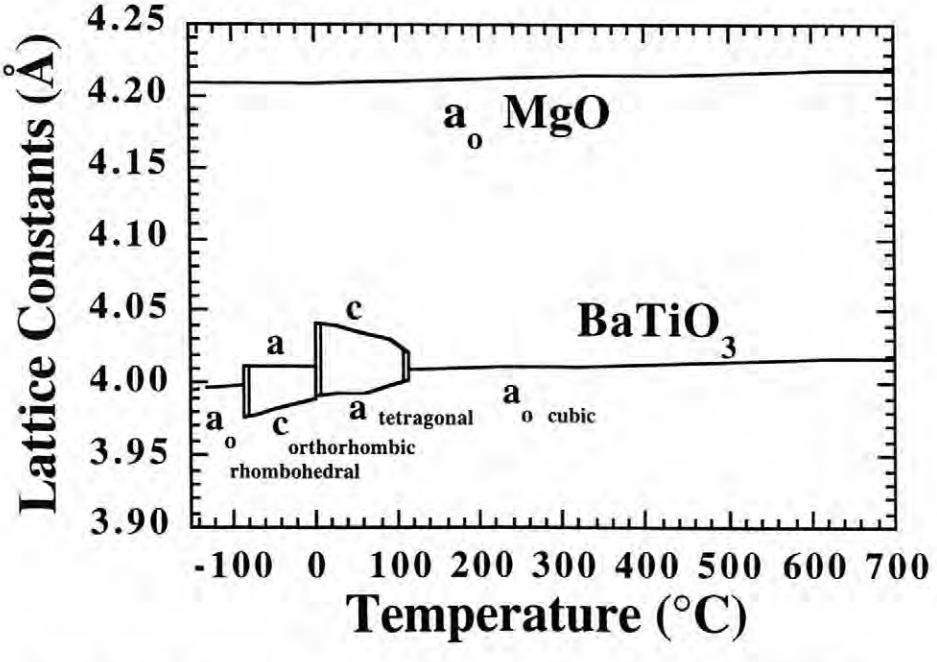

Figure 4.2 Temperature dependence of the lattice constants of MgO and $BaTiO_3$

The temperature dependence of thermal expansion is an important quantity for the determination of residual stress upon cool down from the growth temperature and will be discussed qualitatively later in this section.

Determination of the optimal growth conditions for barium titanate on magnesium oxide was simply a matter of increasing the growth temperature and finding at which point in temperature the crystallinity would not improve. Since no known reactions occur at growth temperatures of interest, crystallinity of the film was the only concern. For barium titanate growth, the best crystallinity was observed at temperatures above 650°C.

Figures 4.3 through 4.5 illustrate the structural characterization of an approximately 750 Å thick barium titanate thin film deposited on MgO by 4-circle x-ray diffraction. Three patterns are shown for each film/substrate combination: theta-two theta, phi, and omega. Theta-two theta scans give information about interplanar spacing and out of plane orientation, phi about in-plane rotational orientation, and omega resolves information as to the mosaic structure of the crystal. Full width half maximum values (FWHM) for barium titanate reflections are reported for each circle and were used to quantify the crystalline perfection. In all diffraction patterns, '*' indicate substrate peaks.

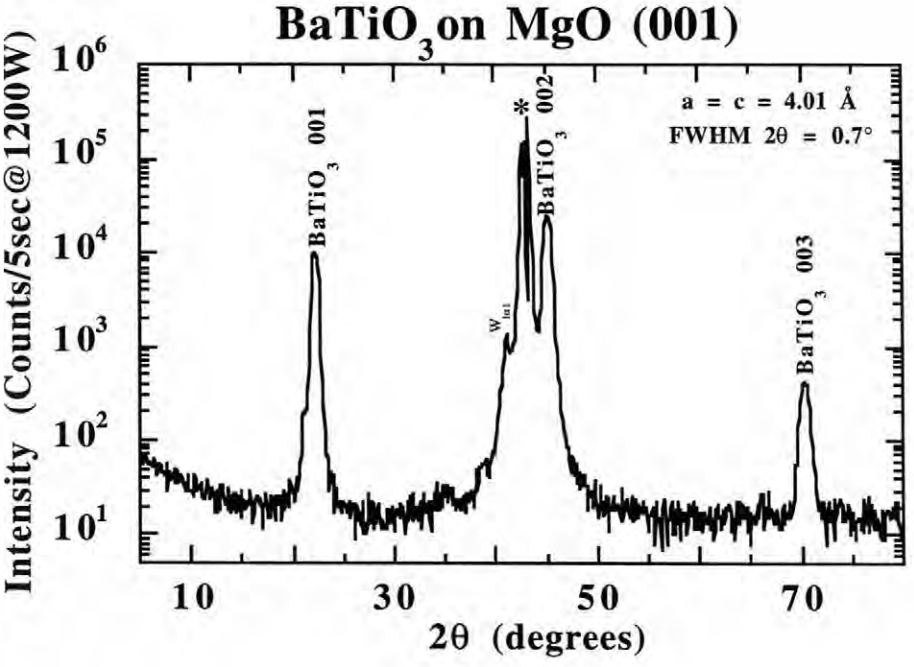

Figure 4.3: θ-2θ scan of $BaTiO_3$ on MgO (001)

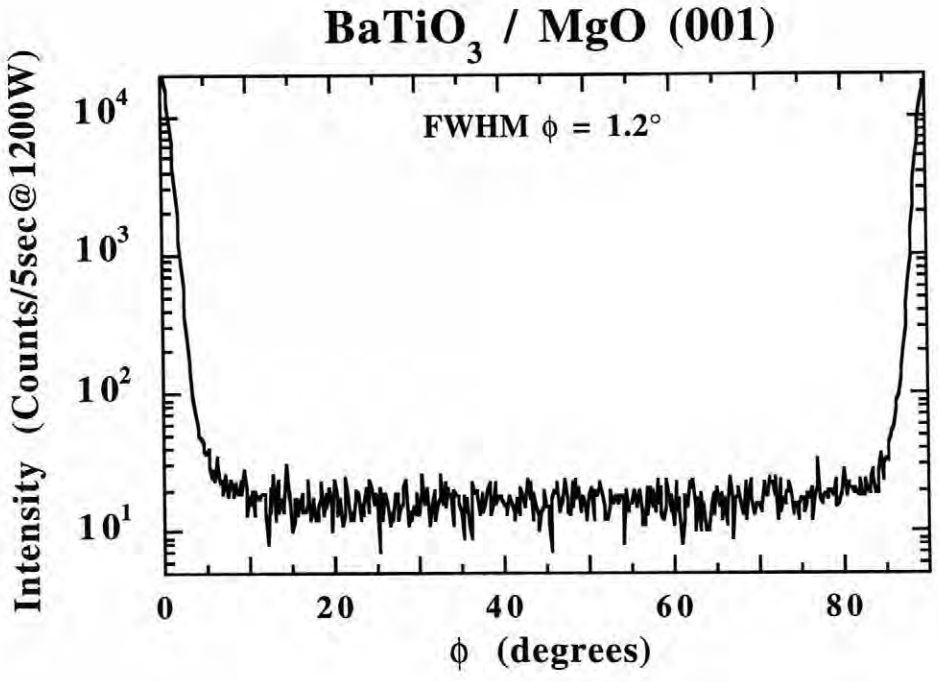

Figure 4.4: Phi-scan of $BaTiO_3$ (101) reflection

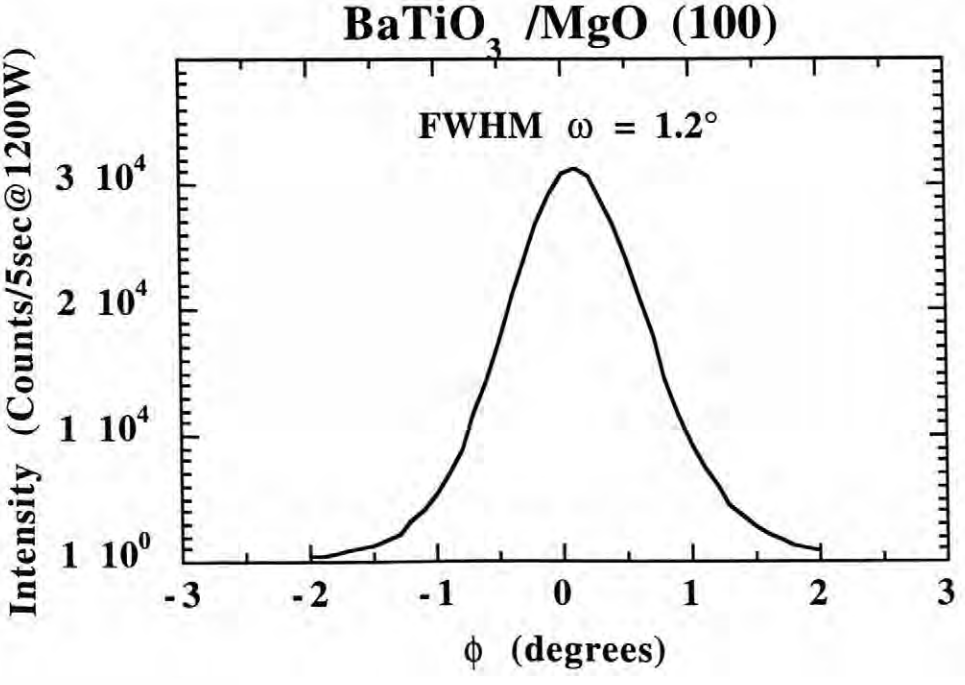

Figure 4.5: Rocking curve of the $BaTiO_3$ (002) reflection

4.2 Barium titanate deposition on lithium fluoride

Since it is isostructural to magnesium oxide, lithium fluoride can also be used as a substrate for epitaxial barium titanate growth. The two face centered cubic sublattices in this instance are composed of lithium and fluorine ions. As in the case of MgO, the {001} family of planes act as the growth surface for $BaTiO_3$ films. The use of LiF has been largely limited by the volatility of fluorine above ~600°C and the very large thermal expansion coefficient. Figure 4.6 illustrates the (001) plane in LiF.

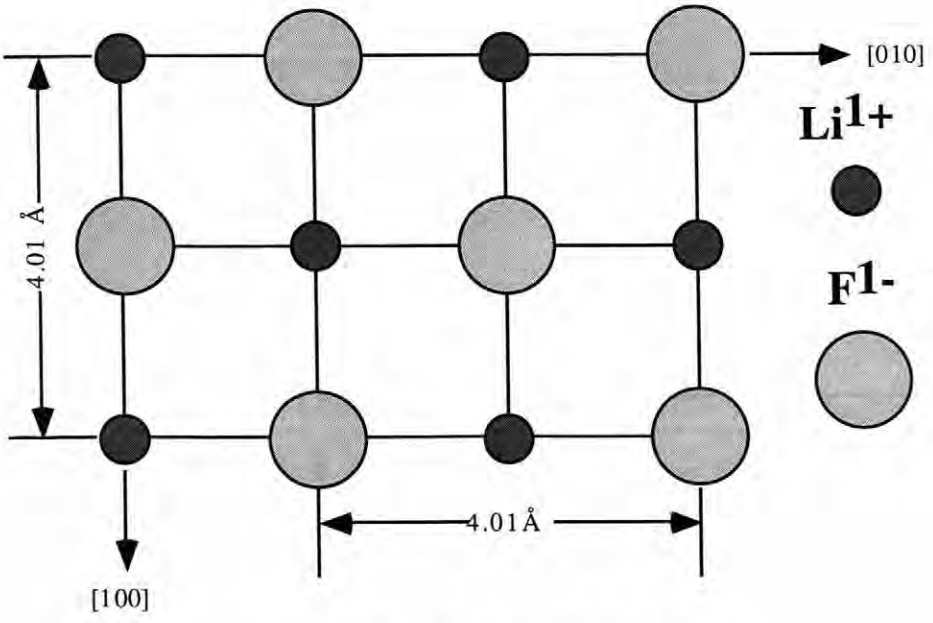

Figure 4.6: LiF (001) crystal surface

If the only criterion for substrate selection were the room temperature lattice match between film and substrate, LiF would be an excellent choice for the deposition of many perovskites. At 25°C, for a c-axis oriented film, the lattice mismatch between LiF and $BaTiO_3$ is only 0.4% with respect to the $BaTiO_3$ bulk lattice.

Several difficulties were observed with lithium fluoride substrates, including fluorine volatility, thermal expansion mismatch, and moisture resistance. In the vicinity of 600°C lithium fluoride crystals begin to volatilize [Muller *et al.*, 1963]. This sublimation effectively limits the maximum temperature at which material can be deposited, given the difficulty for both vapor coalescence and sublimation to occur simultaneously. Barium titanate films deposited at 600°C and above appeared brown and rough. It is possible that the brown color originated from reduction of the titanium by fluorine or generation of color centers in the LiF crystal. For $BaTiO_3$ films, 500°C was found to be a suitable temperature for epitaxial growth. However, this low temperature value resulted in rather poor crystallinity regardless of the small value of lattice mismatch. Figures 4.7, 4.8, and 4.9 illustrate the structure of ~ 1000Å thick c-axis oriented $BaTiO_3$ on LiF.

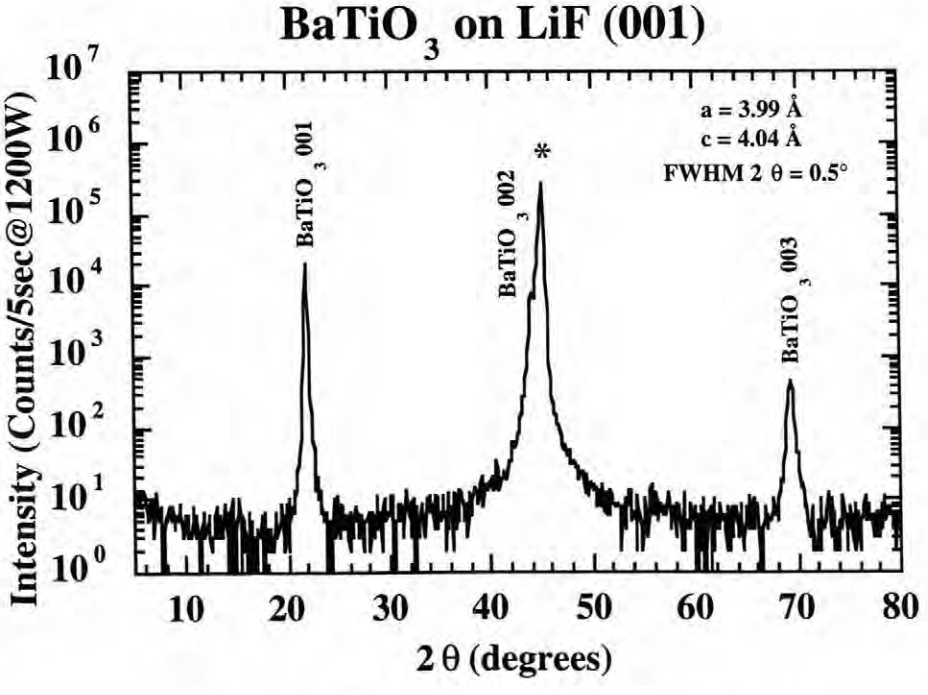

Figure 4.7: θ-2θ scan of $BaTiO_3$ on LiF (001)

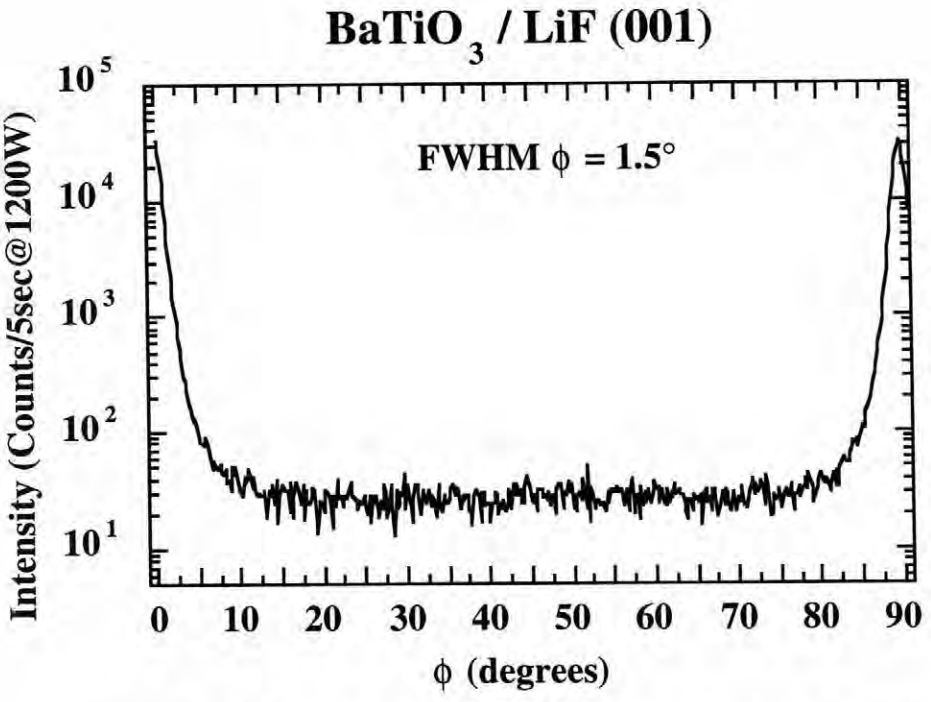

Figure 4.8: Phi-scan of $BaTiO_3$ {101} reflections on LiF (001)

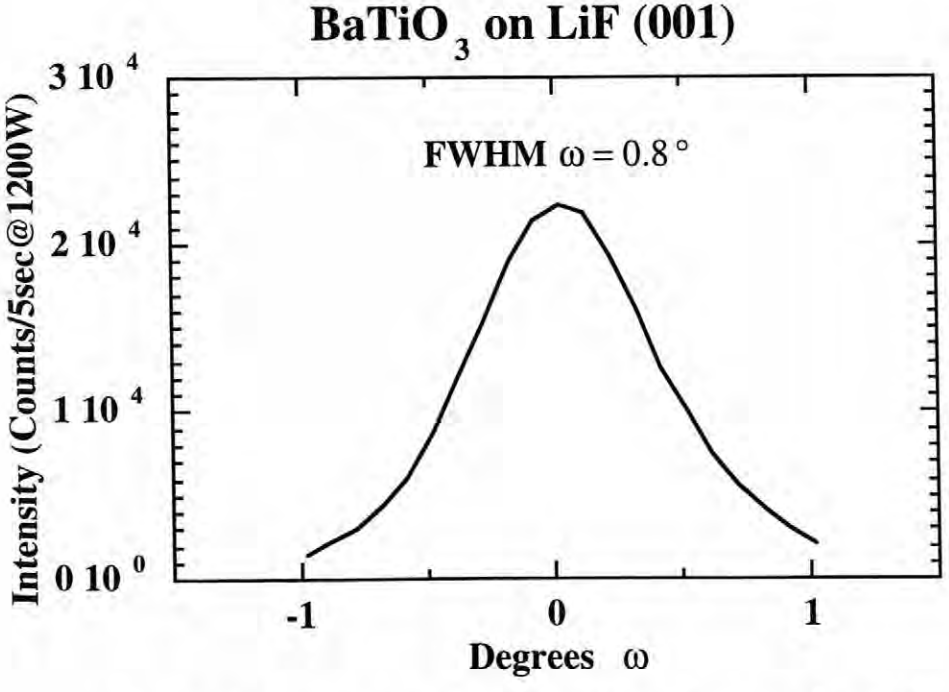

Figure 4.9: Omega-scan of $BaTiO_3$ (003) reflection on LiF (001)

The large thermal expansion coefficient of lithium fluoride also posed a problem for thin film deposition. It is not uncommon for epitaxial films deposited at high temperatures to be stress relieved at the growth temperature. This can occur via nucleation of dislocations whose Burger's vectors lie in the plane of the substrate. Upon cool down, however, if the two materials strain incoherently as a function of temperature, large planar stresses will evolve. If the stresses are large enough, fractures in the film, or even lift-off may occur. Figure 4.10 gives the thermal expansion temperature dependence for LiF. It can be seen that the thermal expansion coefficient of LiF is approximately 3 times larger than that of $BaTiO_3$.

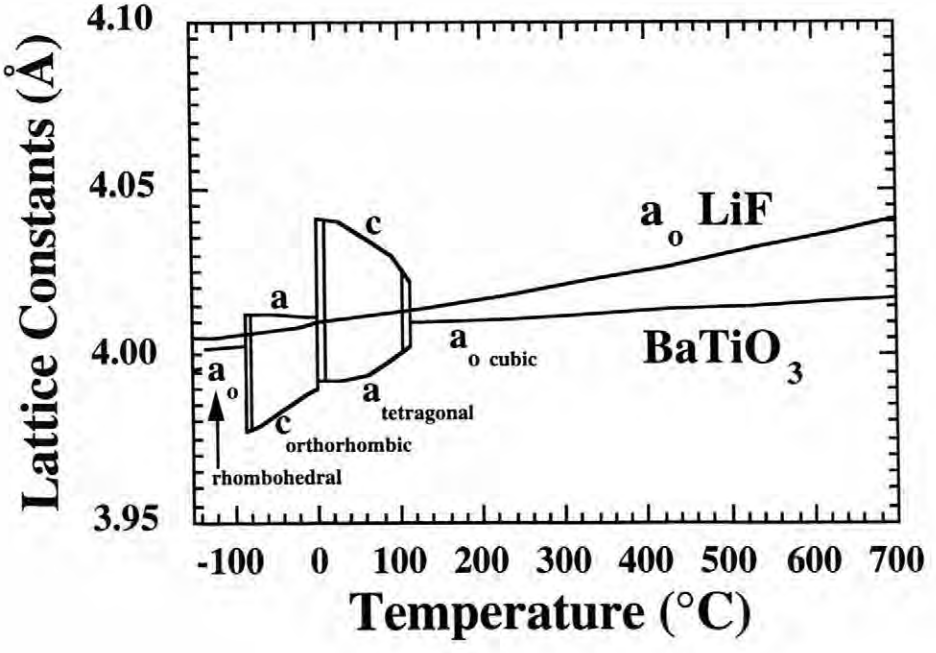

Figure 4.10: Temperature dependence of the lattice constants of LiF and $BaTiO_3$

Both failures were observed for $BaTiO_3$ films deposited on LiF. For a 2000Å thick $BaTiO_3$ film deposited upon LiF, the thermal expansion-induced strains caused delamination. This was not unexpected considering the weak bonding that is likely between oxide and fluoride layers and the large stresses involved. When the film thickness was reduced to approximately 1000 Å, delamination did not occur, however, when the surface was imaged, ubiquitous cracking was observed. Regardless of the cracking, the film was found to be epitaxial. Though film peeling is unacceptable for film fabrication, it may afford a unique sample preparation opportunity for transmission electron microscopy (TEM). It is possible that TEM thin film specimens free of the substrate elastic constraints can be investigated.

4.3 Barium titanate deposition on lanthanum aluminate (001)

Lanthanum aluminate crystals have become a very popular choice for epitaxial growth of materials when it is important to have a low dielectric constant substrate. Microwave devices involving single crystal superconducting films have accounted for the greatest usage of these substrates.

The presence of a ferroic transition in $LaAlO_3$ at approximately 500°C from the cubic to rhombohedral phase leads to the development of twins in the crystal [Yao *et al.*, 1992]. The presence of these twins is somewhat problematic and is reflected in the surface roughness and crystallinity of the deposited films The twin boundaries in $LaAlO_3$ run nearly normal to the {001} surface and as a result, at their surface termination leave a small peak. Owing to these twins, surface roughnesses of ~ 80 Å are commonly found on polished $LaAlO_3$ wafers [Commercial Crystal Labs Inc., Naples, FL]. By x-ray diffraction, the twins are visible by scanning in the theta circle at a constant two-theta value. The twin peaks have been found to be separated by approximately 0.5 ° in omega. The same twins can be detected in high quality barium titanate crystals grown upon $LaAlO_3$.

The crystalline structure of $LaAlO_3$ at room temperature is rhombohedral with the angle α between unit cell edges ~ 60.1°. If the angle were exactly 60°, than the unit cell could be reconstructed as cubic, however the deviation is small enough that classification as pseudo-cubic and pseudo-perovskite with α slightly larger than 90° is suitable. The top half of the pseudo-cubic, pseudo-perovskite unit cell is schematically represented in figure 4.11.

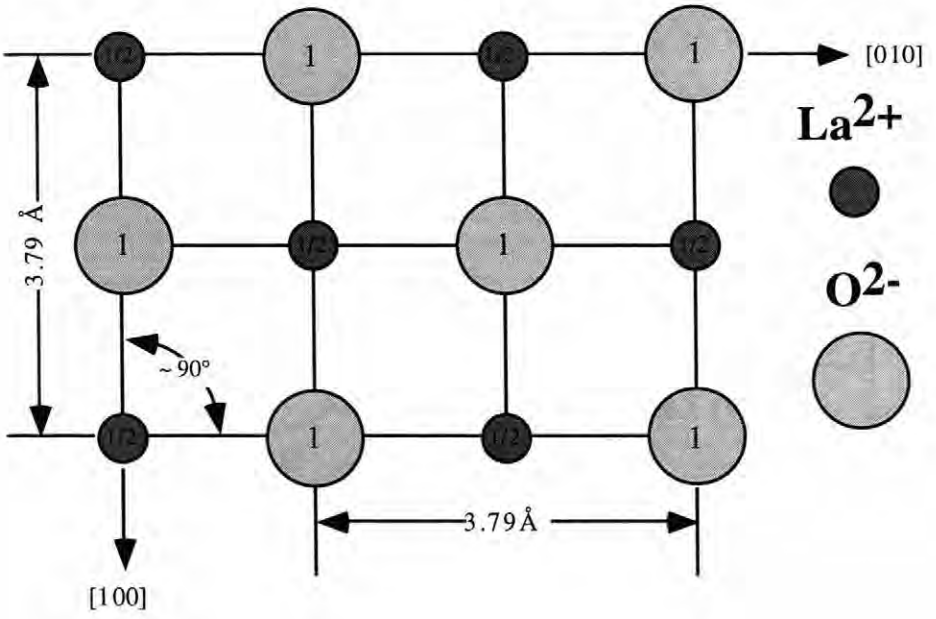

Figure 4.11: (001) surface of $LaAlO_3$, numbers indicate height along [001] in unit cell

Barium titanate crystals align epitaxially with their [001] directions coincident with those of the $LaAlO_3$ substrate. The room temperature lattice mismatch for a c-axis $BaTiO_3$ film is 5.01% with respect to the bulk $BaTiO_3$ lattice parameters. Though the lattice mismatch between $BaTiO_3$ and $LaAlO_3$ is larger than or similar to that found with other substrates, i.e. LiF and MgO, the films grown on $LaAlO_3$ show better crystallinity. This effectively

demonstrates the importance of structure match between film and substrate in addition to the lattice match. Figure 4.12 gives the temperature dependence of the lattice constants of $LaAlO_3$ and $BaTiO_3$. At the growth temperature of ~700°C, the thermal expansion coefficients of $BaTiO_3$ and $LaAlO_3$ are 14.5 and 12 ppm/°C respectively. These differences lead to the generation of a planar residual stress on the order of 110 MPa. Comparatively, the growth stresses due to lattice mismatch between film and substrate are insignificant as they are relieved largely by the nucleation of misfit dislocations [Norton and Carter, 1990]. Figures 4.13 through 4.16 show the structure of an approximately 2000 Å thick $BaTiO_3$ film grown on {001} $LaAlO_3$.

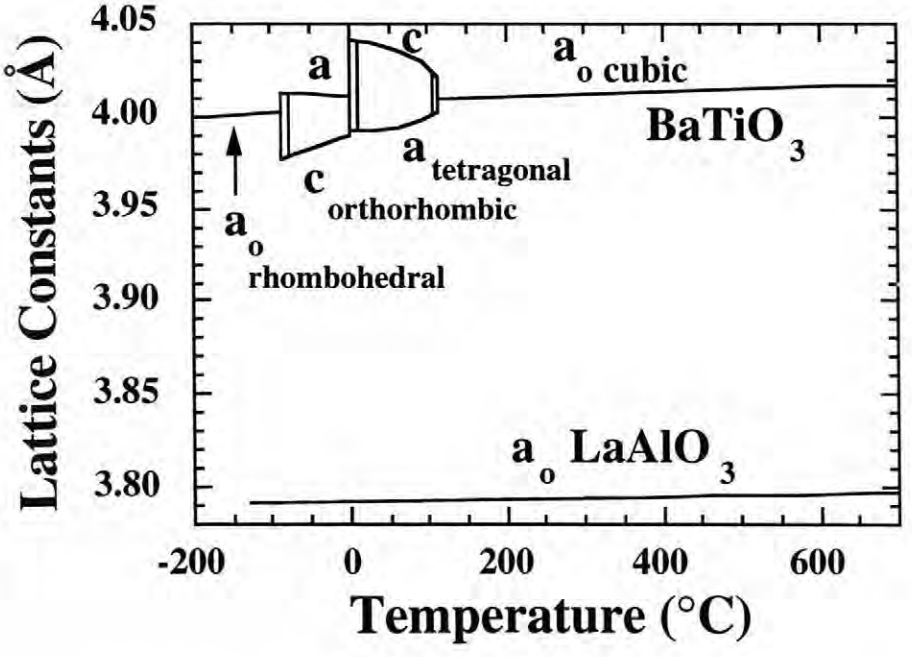

Figure 4.12: Temperature dependence of the lattice constants of $LaAlO_3$ and $BaTiO_3$

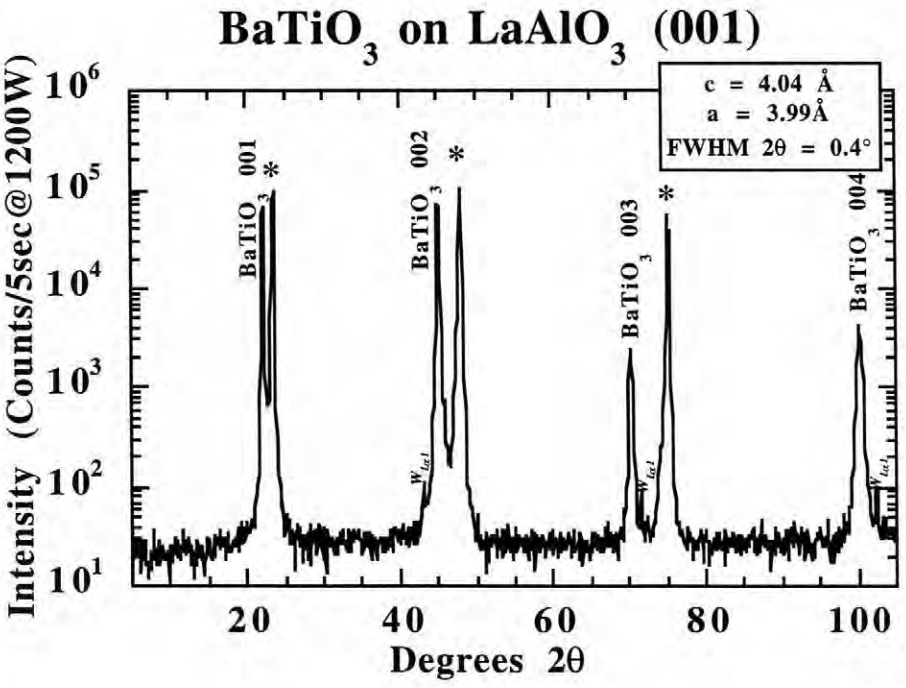

Figure 4.13: θ-2θ scan of $BaTiO_3$ on $LaAlO_3$ (001)

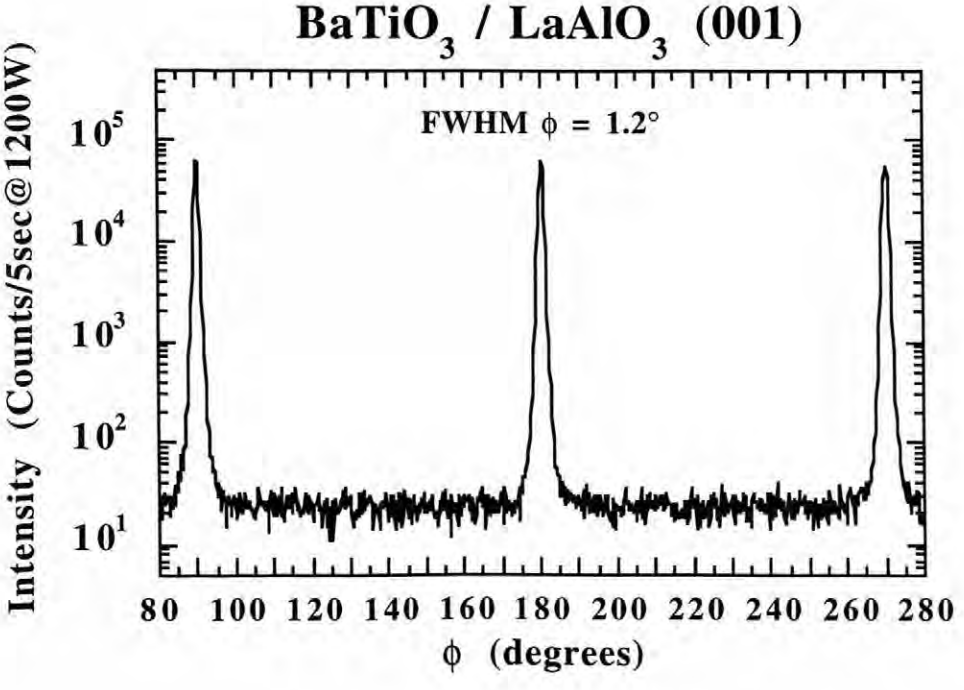

Figure 4.14: Phi-scan of $BaTiO_3$ (101) reflections

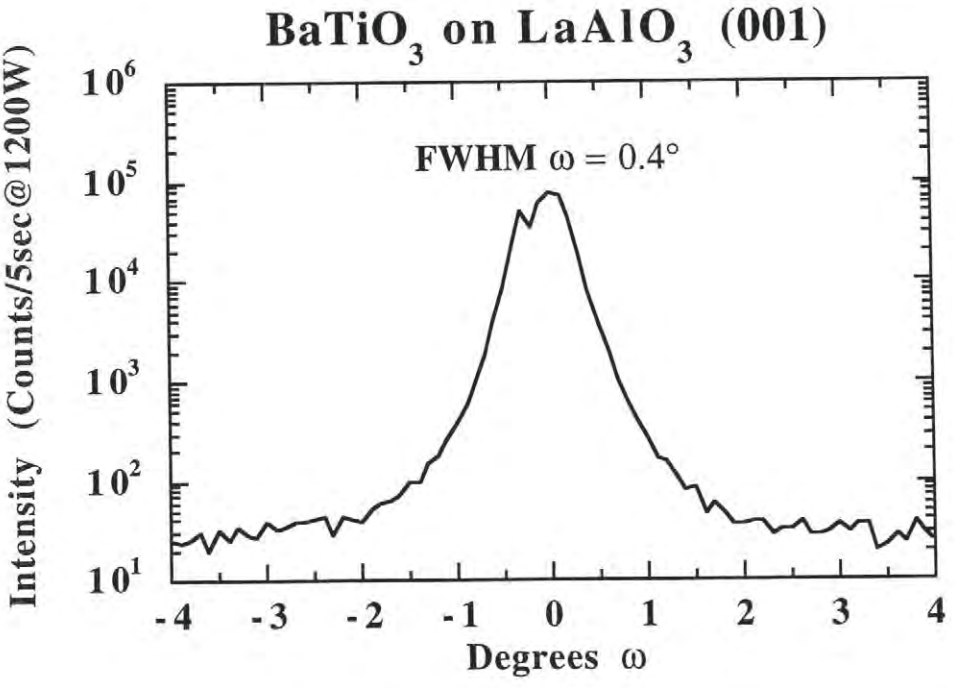

Figure 4.15: Rocking curve of $BaTiO_3$ (002) reflection

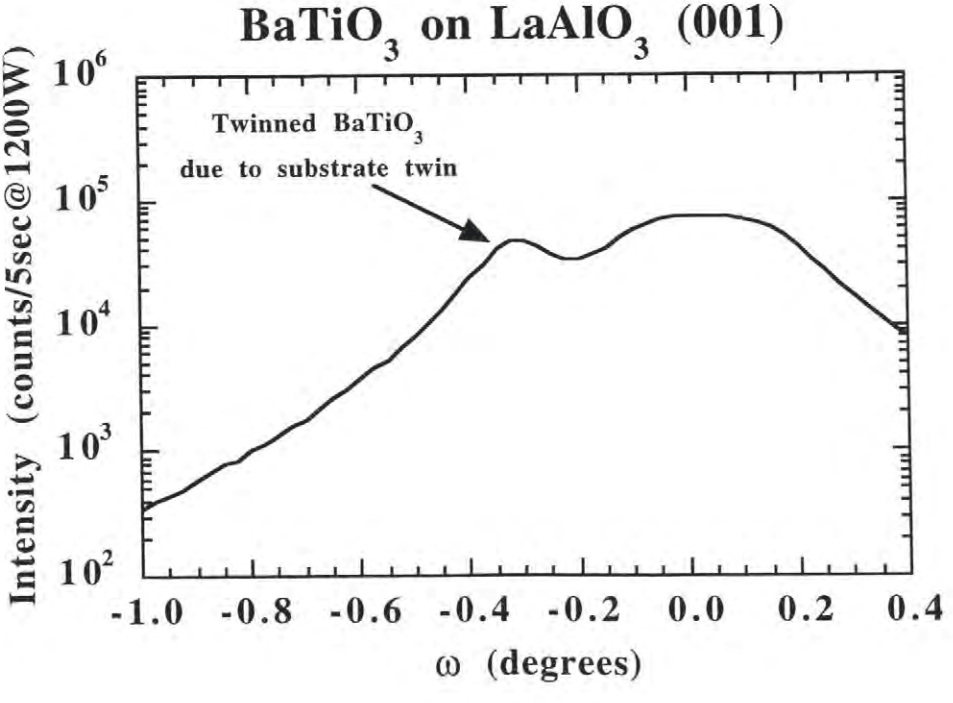

Figure 4.16: Close-up of $BaTiO_3$ (002) rocking curve

In figure 4.16 a finer scan in omega of the $BaTiO_3$ (002) reflection is shown. The small second peak present in this rocking curve reflects the presence of twins in the substrate. Since the $LaAlO_3$ cubic to rhombohedral transition occurs at ~450°C, and the growth temperature of this film was 680°C, the twinning or puckering in the $BaTiO_3$ must occur as a result of rigid clamping to the substrate since at the $LaAlO_3$ transition temperature nucleation of sufficient dislocations to relax out the strain would be unlikely. When the associated substrate peak was rocked upon, the identical twin structure and angular separation was observed. The substrate-induced twin structures were only visible in the $BaTiO_3$ films of the highest crystalline quality, and were only observable at two orientations in the phi circle which were 180° apart. These orientations corresponded to two antiparallel directions in the <100> family.

When very thin $BaTiO_3$ films were deposited on $LaAlO_3$ it was observed that nearly equal amounts of a and c-oriented grains were present. As the film thickness increased, the fraction of c-oriented grains nucleated during the transition increased while the amount of a-oriented grains remained nearly constant. Ultimately, in thick $BaTiO_3$ films (~ 1000 Å), only c-oriented grains were visible by x-ray diffraction. Figure 4.17 shows a close-up in two-theta of two $BaTiO_3$ films which are approximately 250 and 500 Å thick. It is possible that a constant fraction of a-oriented $BaTiO_3$ always exists near the film/substrate interface, with the volume of a-oriented regions limited by the anisotropic lattice strains. For films of greater thickness, 1000Å+, the a-oriented grains were not visible by x-ray diffraction.

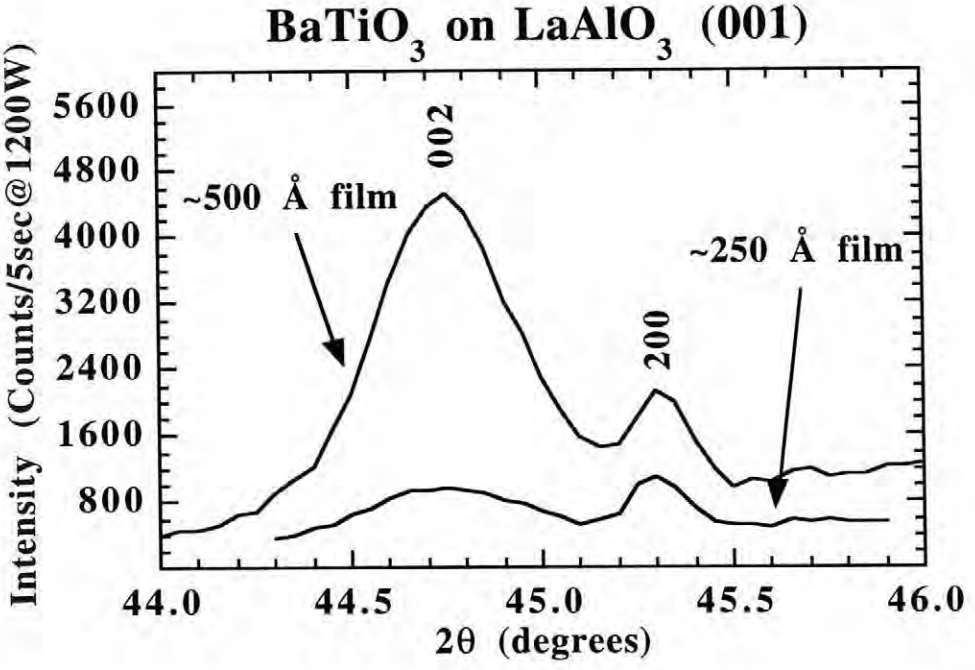

Figure 4.17: Close-up in 2θ of thin $BaTiO_3$ films grown on $LaAlO_3$

4.4 Barium titanate deposition on strontium titanate

Strontium titanate has proven to be the choice substrate for the deposition of $BaTiO_3$ epitaxial films. The two materials, both possessing the perovskite structure, have a room temperature lattice mismatch of 2.2% for a c-axis oriented film with respect to $BaTiO_3$ bulk lattice constants. Figure 4.18 gives a schematic of the {001} growth plane of $SrTiO_3$.

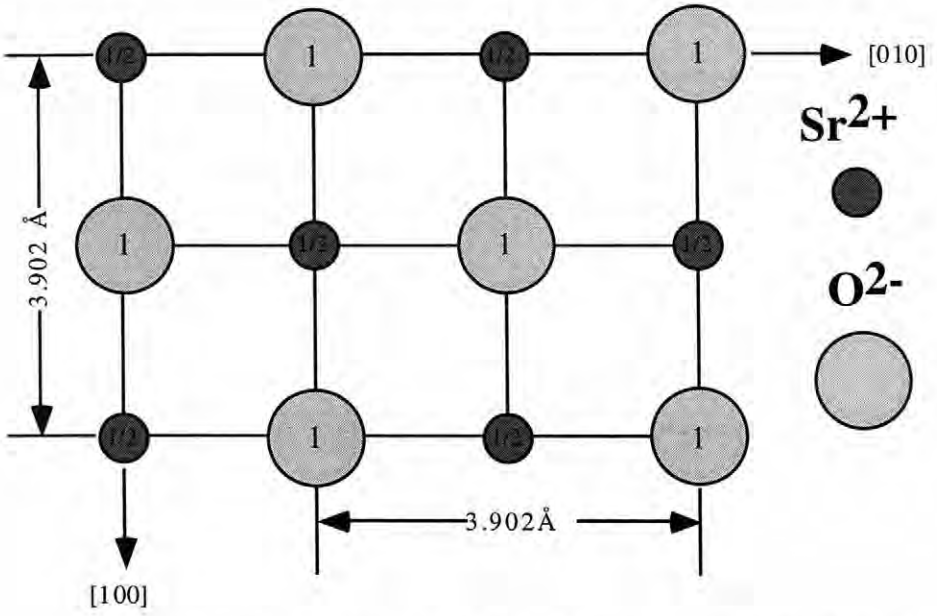

Figure 4.18: (001) surface of $SrTiO_3$, numbers give the heights along [001] in the unit cell

Strontium titanate also boasts one of the smoothest surfaces; as polished substrates exhibit typical roughnesses of 3 Å rms, or 10 Å maximum step height [Commercial Crystal Labs, Naples, FL]. The films with the best crystallinity were deposited near 650°C, showing negligible improvement with increasing temperature. Though $BaTiO_3$ is known to go into solution with $SrTiO_3$, the growth temperatures used during deposition are far too low for significant migration or diffusion to occur at the interface. With small concentrations of dopants, typically neodymium or tantalum, $SrTiO_3$ can be made conductive, thus allowing through-the-thickness electrical property measurements without a bottom electrode layer. Figure 4.19 shows the temperature dependence of the thermal expansion coefficient of $SrTiO_3$. At the growth temperature of ~700°C, the thermal expansion coefficients of $BaTiO_3$ and $LaAlO_3$ are 14.5 and 11.6 ppm/°C respectively. These differences lead to the generation of a planar residual stress on the order of 60 MPa. Comparatively, the growth

stresses due to lattice mismatch between film and substrate are insignificant as they are relieved largely by the nucleation of misfit dislocations [Norton and Carter, 1990]

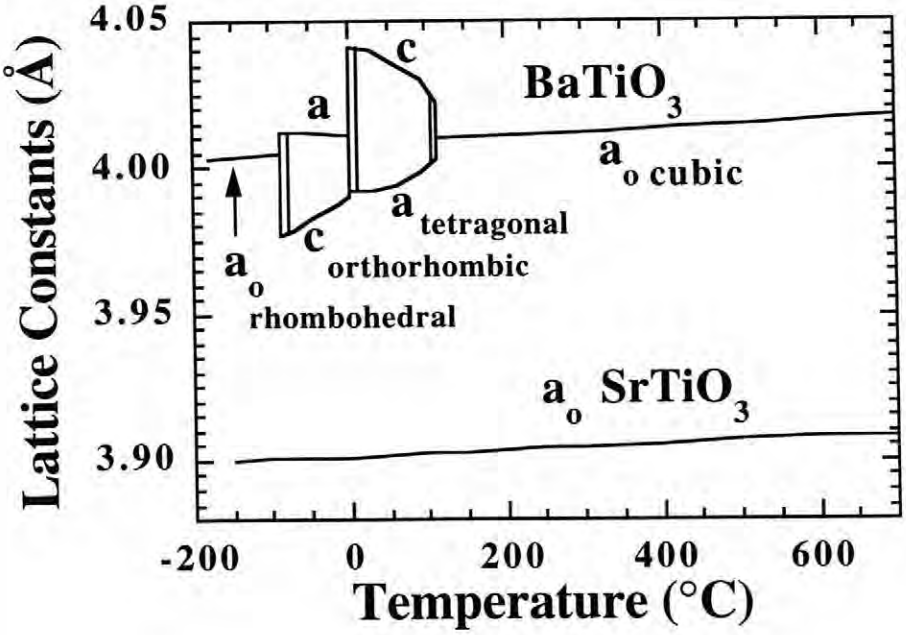

Figure 4.19: Temperature dependence of the thermal expansion coefficient of $SrTiO_3$

Figures 4.20 through 4.22 illustrate the x-ray data for approximately 2000 Å thick $BaTiO_3$ films deposited on (001) $SrTiO_3$.

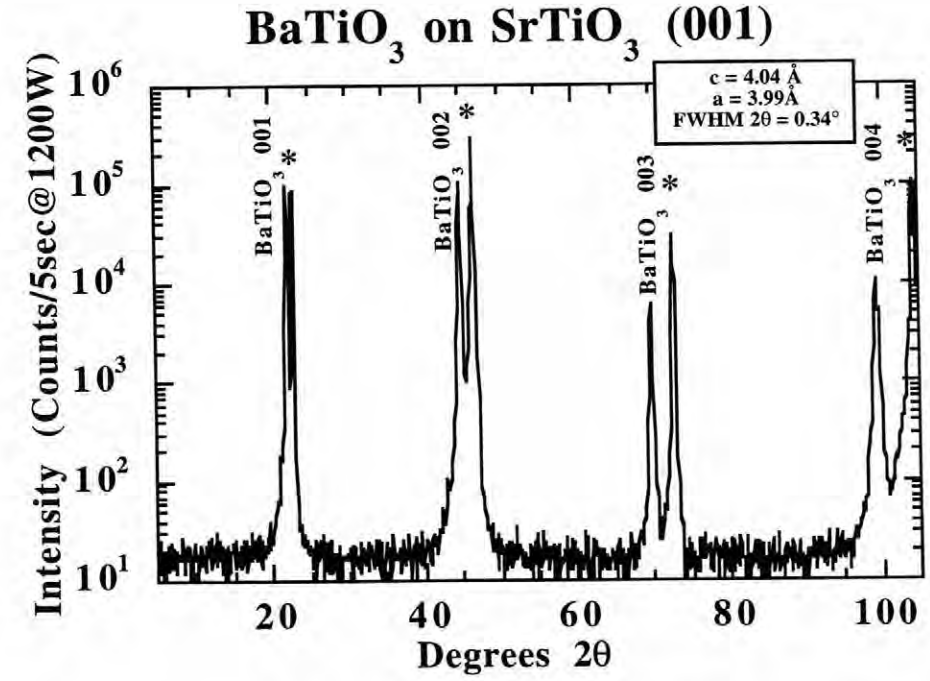

Figure 4.20: θ-2θ scan of $BaTiO_3$ on $SrTiO_3$ (001)

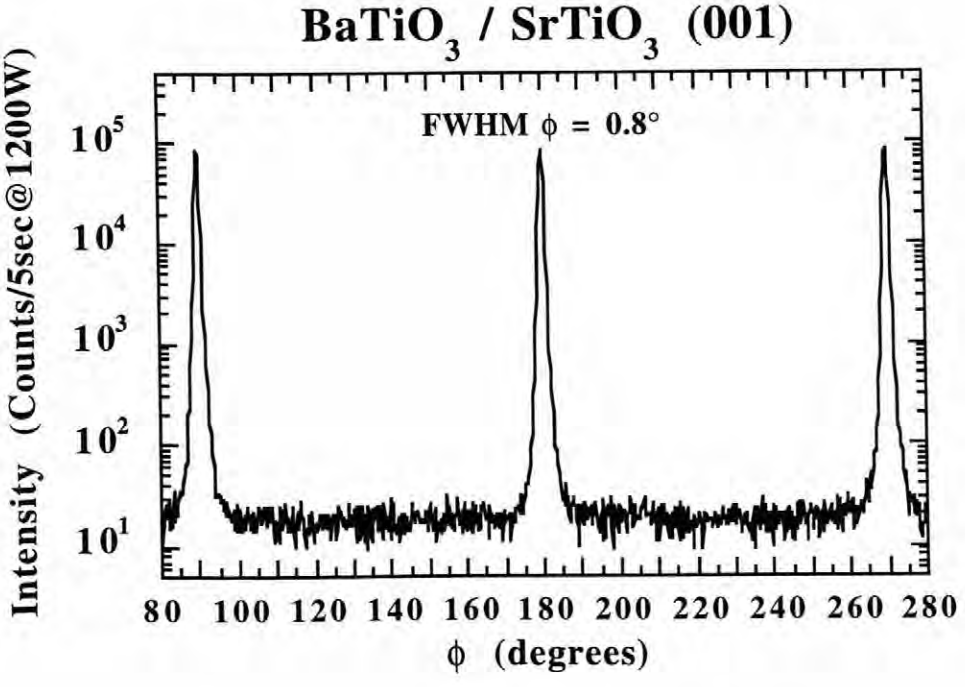

Figure 4.21: Phi-scan of $BaTiO_3$ (101) reflections

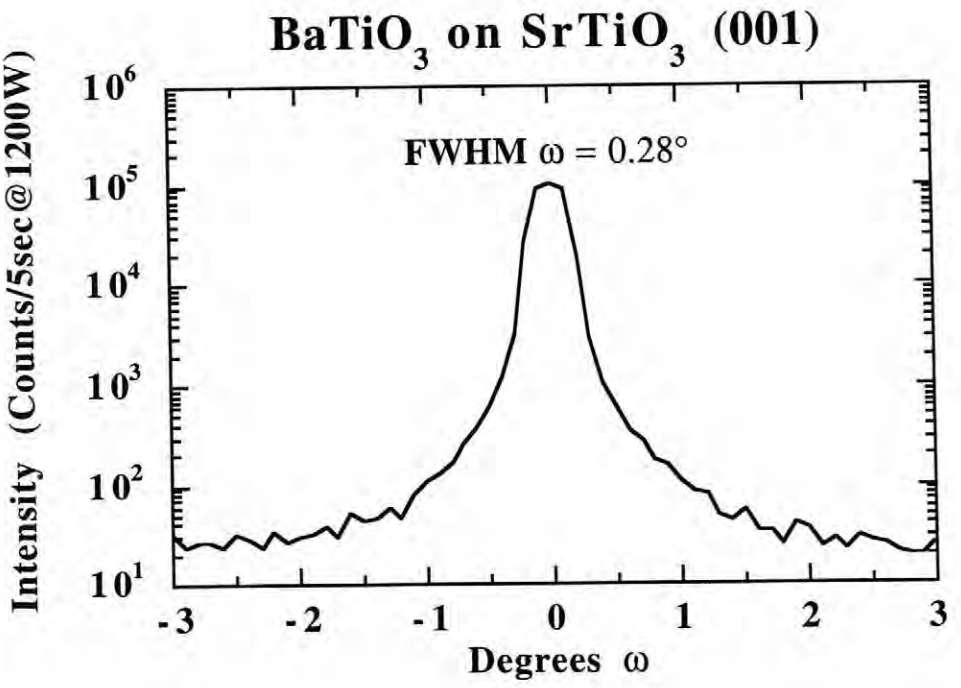

Figure 4.22: Rocking curve of $BaTiO_3$ (002) reflection

From examination of a standard θ-2θ pattern, the primary orientation of the film can be determined by measuring d-spacings and comparing those values to tabulated data in order to determine which planes are parallel to the growth surface. In the case of $BaTiO_3$ where the tetragonal strain is only ~1%, discerning the difference between a and c orientation may be difficult. With relative certainty, the primary orientation may be determined by investigation of high intensity peaks, however, detection of small fractions of twinned material requires additional care. When looking for twin peaks it is desirable to choose those pairs of reflections with large angular separation in one circle only. In doing so, one x-ray scan can detect both orientations, if present, since the small separations in the

other circles are likely beyond the resolution of the diffractometer. Figure 4.23 illustrates such a situation in $BaTiO_3$.

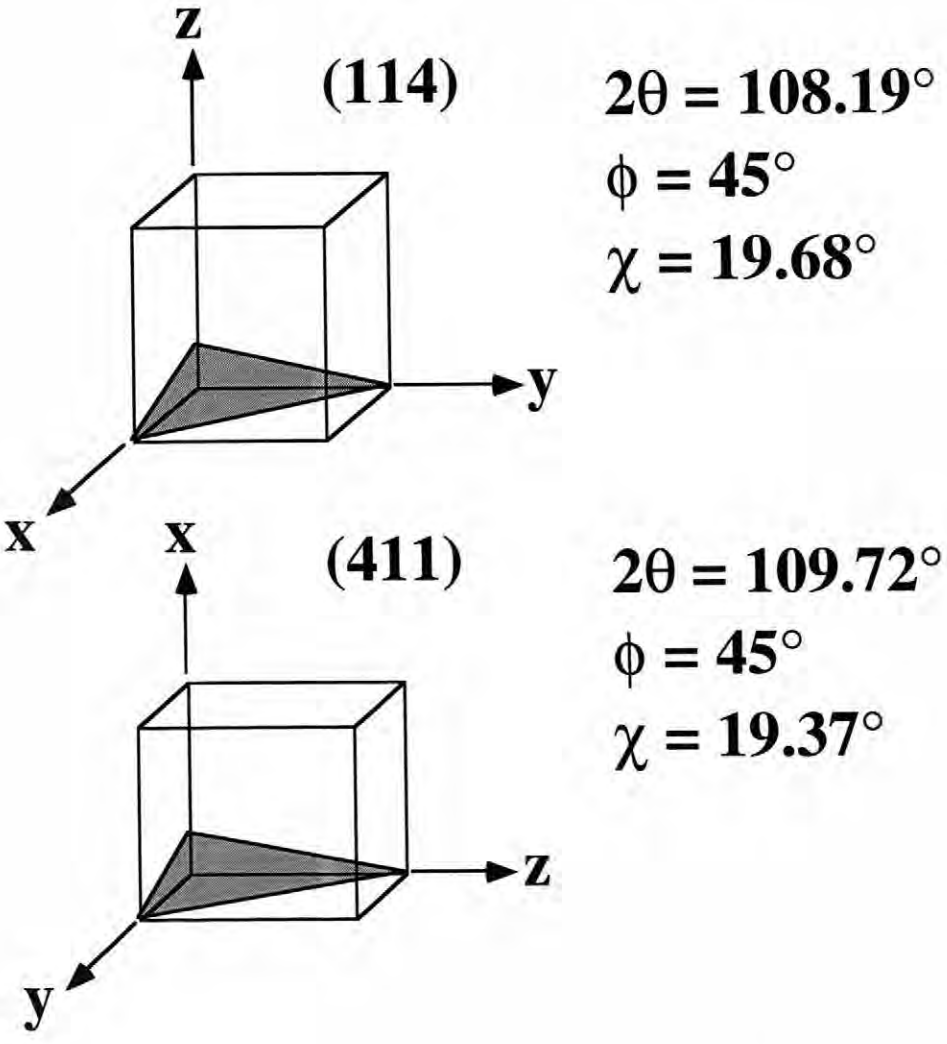

Figure 5.23: Twinned orientations of $BaTiO_3$ and the diffractometer angles which satisfy the Bragg conditions for diffraction

The angular separations in the phi and chi-circles of the two reflections in figure 5.23 are not able to be resolved by the PSU-Picker diffractometer. However, there is a

relatively large separation in the 2θ scan. This condition allows both reflections to be observed in one θ-2θ scan. Figure 5.24 shows such a scan for a $BaTiO_3$ film on $SrTiO_3$.

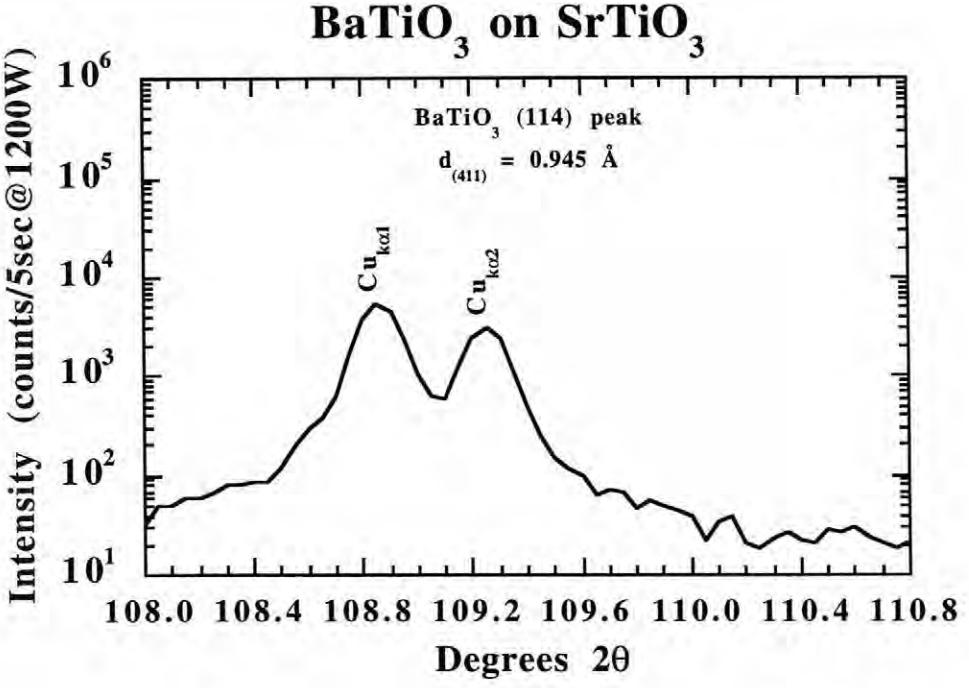

Figure 4.24: θ-2θ scan of $BaTiO_3$ (114) reflection on a $SrTiO_3$ substrate

In this exploded-view diffraction pattern, only one $BaTiO_3$ peak is visible. This indicates that the film is untwinned, at least to the detection limits of our diffractometer. The ability for the diffractometer to resolve the different components of Cu radiation supports that the instrument and film are of sufficient quality to resolve the (114) and (411) reflections.

Chapter 5

Heterostructure fabrication and measurement

5.1 Heterostructure Fabrication

A heterostructure may defined as a multiple layer stack of chemically different materials whose lattices are conserved across the material boundary. For the determination of electrical properties, heterostructure devices offer the advantage of measurement as a function of crystallographic direction, enabling anisotropic relationships to be investigated. For example, the dielectric constant or remanant polarization of a c-axis grown ferroelectric sample can be measured along, or perpendicular to the polar axis using through-the-thickness or strip electrodes respectively.

In our experiments two types of heterostructures were deposited: those of the system $BaTiO_3$ on $SrRuO_3$ on $LaAlO_3$, (BSL-series), and $BaTiO_3$ on $SrRuO_3$ on $SrTiO_3$, (BSS series). All of the samples presented incorporated the $SrRuO_3$ bottom electrode because it was desired to conserve the perovskite, or pseudo-perovskite structure throughout the thin film stack. For completion of the capacitor structures, noble metal electrodes were deposited at room temperature through circular shadow masks (0.0014 cm^2 area). Epitaxial top electrodes were not attempted due to the difficulties encountered with masking fine structures at high temperatures.

5.2 BSL and BSS series heterostructures

Heterostructures on strontium ruthenate bottom electrodes were fabricated with both layers grown off-axis, on-axis, and in mixed arrangements. The structures were optimized for crystallinity, but electrical properties similar to bulk values for barium titanate were not recorded.

Initially, heterostructures were grown with both layers deposited in the off-axis geometry. Reduction of boulder populations was the motive for this, since ultimately very thin films were desired. The most obvious drawback was the large thickness non-uniformity observed along the film and the difficulty in determining reliable thickness values. Boulders were not found to be a problem, as through-the-thickness measurements were made on films as thin as 60 nm without serious shorting problems.

The strontium ruthenate was always observed to grow epitaxially as the first layer, however, in this arrangement, the barium titanate would grow aligned in 2θ but extra orientations in phi were routinely observed. Figures 5.1 through 5.3 show the typical crystalline quality of a BSL series all off-axis grown film. All peaks indexed with "*" indicate substrate reflections. The $BaTiO_3$ lattice parameters are given in the boxes in the θ-2θ scans.

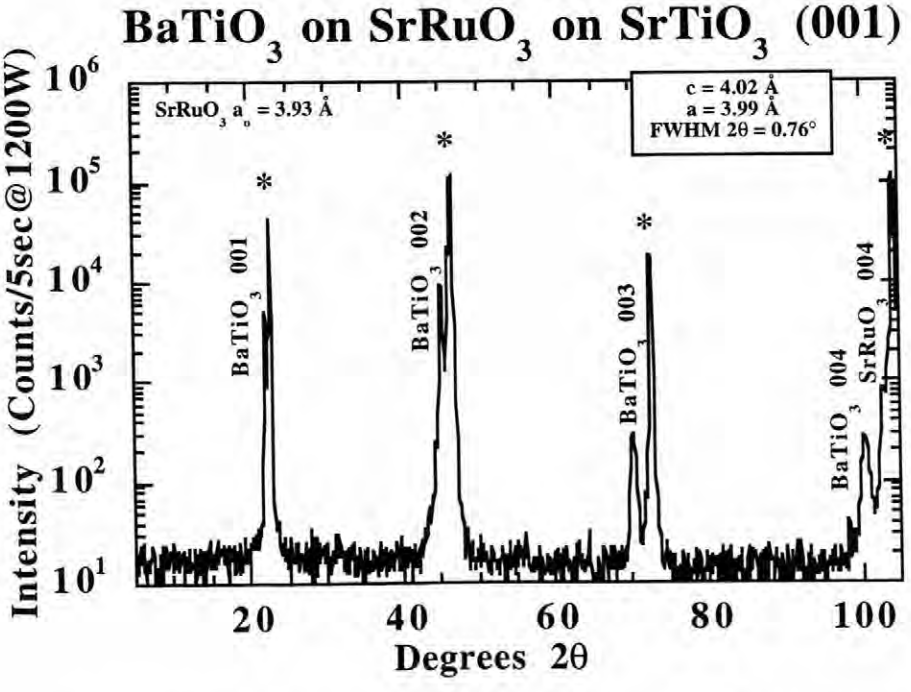

Figure 5.1: θ-2θ scan of BSS-series off-axis grown heterostructure

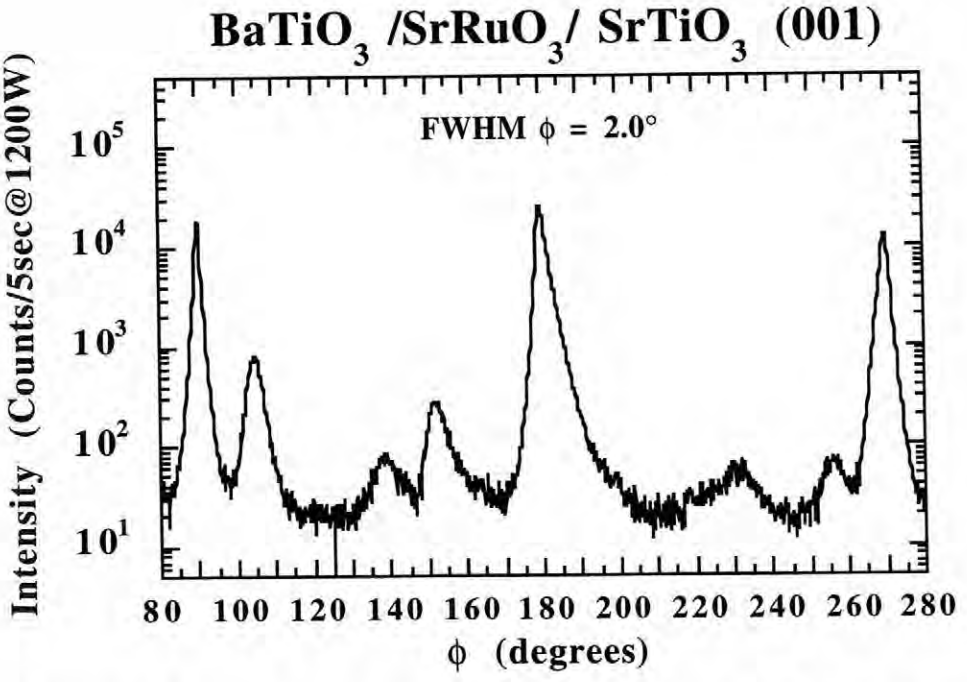

Figure 5.2: ϕ-scan of BSS-series, off-axis $SrRuO_3$ off-axis $BaTiO_3$ (101) peak

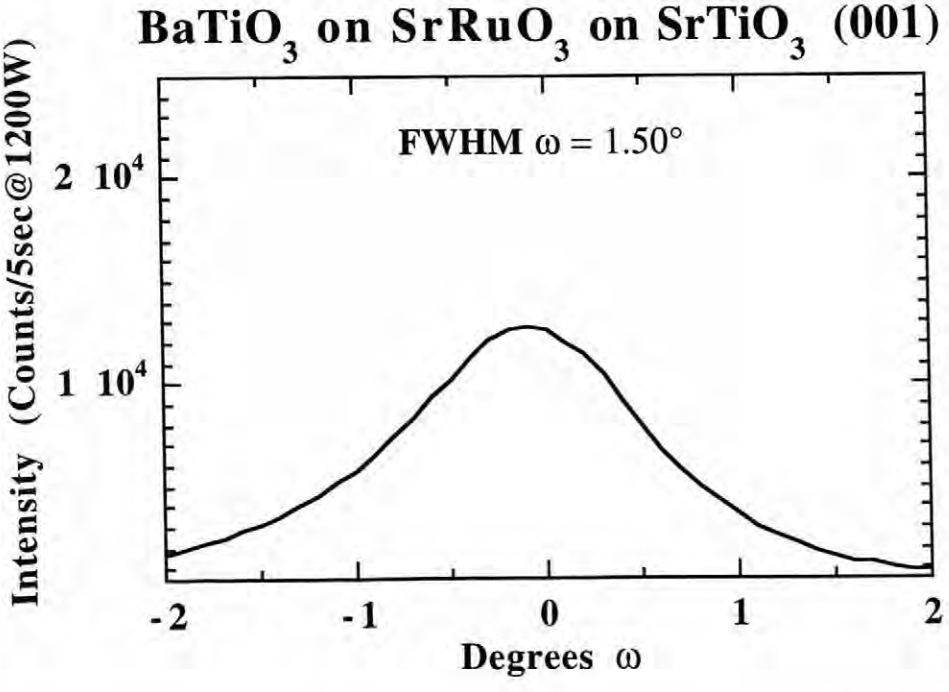

Figure 5.3: ω-scan of BSS-series off-axis $SrRuO_3$ off-axis $BaTiO_3$ (002) peak

As can easily be appreciated from the barium titanate phi-scan, though highly oriented, this film is not epitaxial. It is felt that in the off-axis geometry the lack of energetic bombardment resulted in a loss of epitaxy as well as large peak widths in all circles.

In an attempt to improve the crystallinity and orientation of the barium titanate layer but still minimize the concentration of boulders, the $SrRuO_3$ electrode was deposited off-axis, while the $BaTiO_3$ layer was grown on-axis. The on-axis deposition of $BaTiO_3$ resulted in truly epitaxial films with improved crystallinity. Figures 5.4 through 5.6 demonstrate this. The thickness of the film shown was ~ 2000 Å, which was comparable to the BSL all on-axis film shown in figures 5.7 through 5.9.

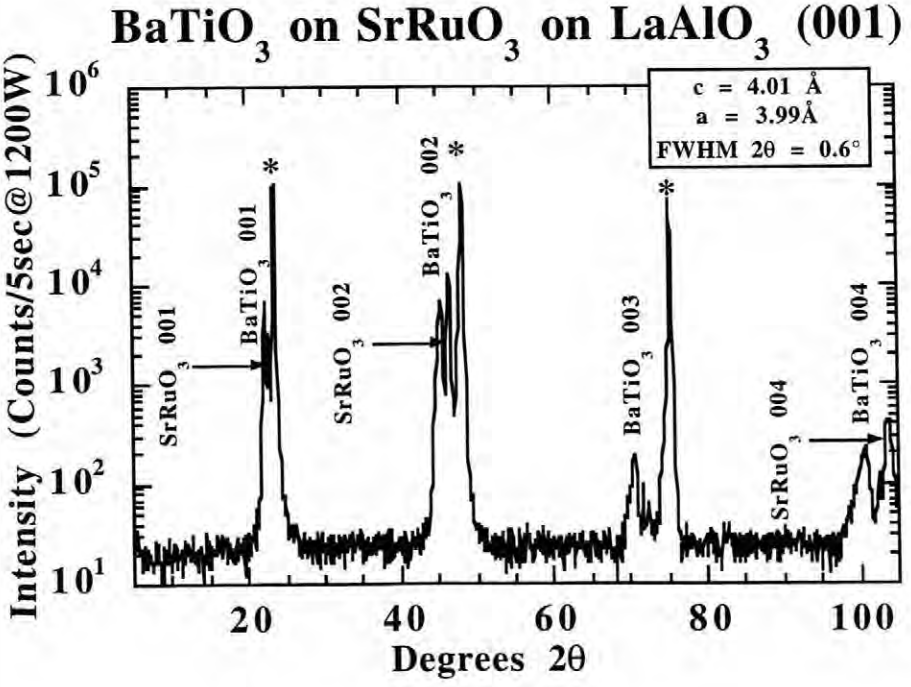

Figure 5.4: θ-2θ scan of BSL-series off-axis $SrRuO_3$ on-axis $BaTiO_3$ heterostructure

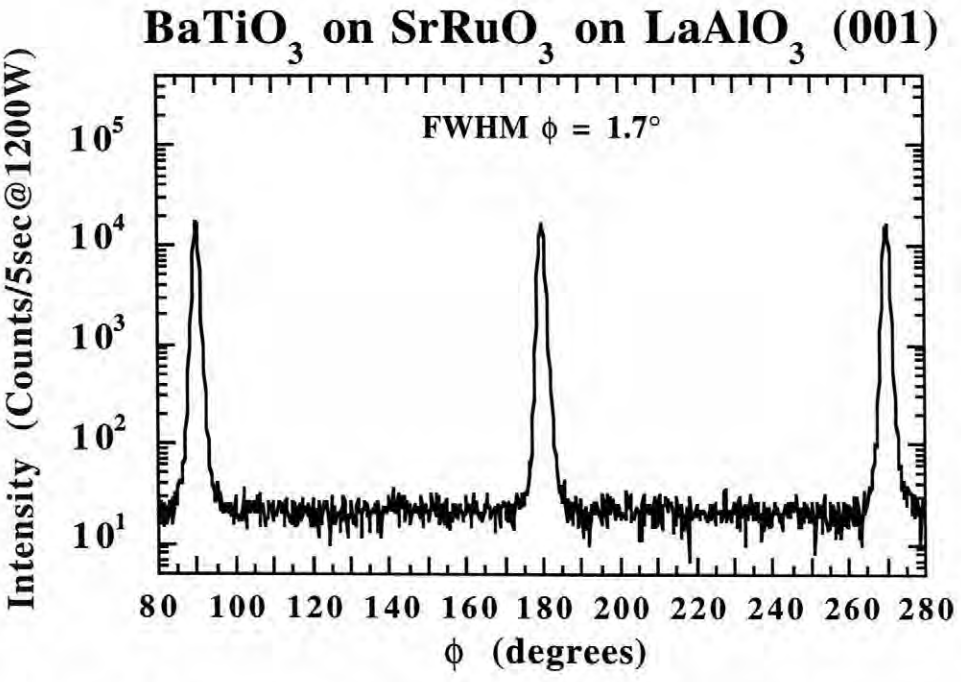

Figure 5.5: ϕ-scan of BSL-series off axis $SrRuO_3$ on-axis $BaTiO_3$ (101) peak

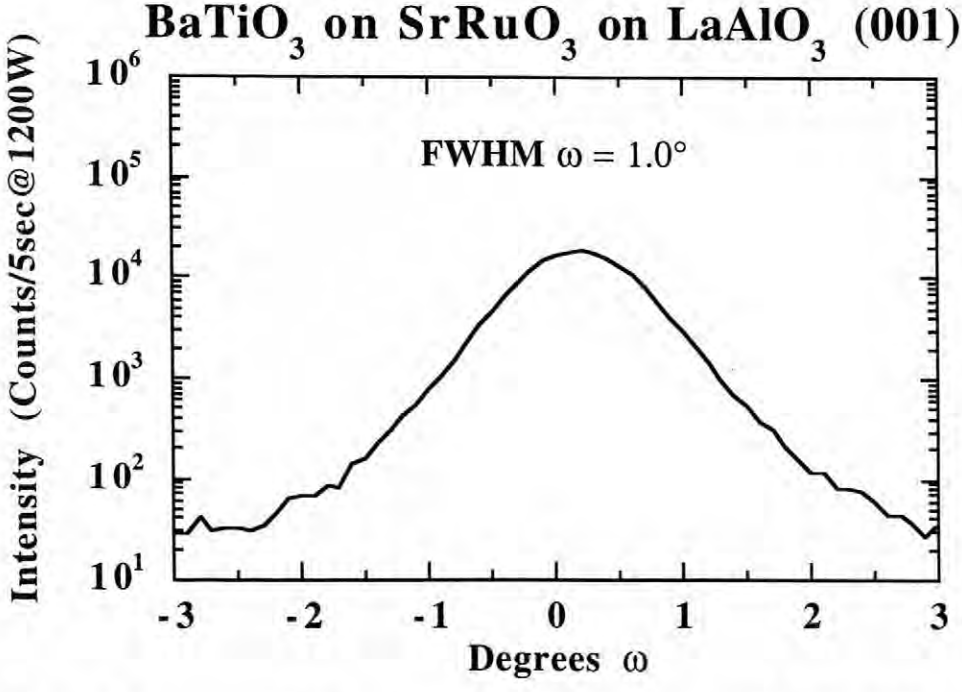

Figure 5.6: ω-scan of BSL-series off-axis $SrRuO_3$ on-axis $BaTiO_3$ (002) reflection

Though the heterostructures deposited using the off-axis electrode, on-axis ferroelectric geometry showed improved crystallinity and true epitaxy, further improvements were desired. Again, shorting during electrical property measurements proved not to be a serious problem, so heterostructures with both layers deposited on-axis were attempted. The benefits and drawbacks of energetic bombardment were clearly illustrated by these experiments. Figures 5.7 through 5.9 show the optimized structure for a BSL-series heterostructure. The thickness of the $BaTiO_3$ layer was ~ 2000 Å. The legend gives data for the $BaTiO_3$ layer.

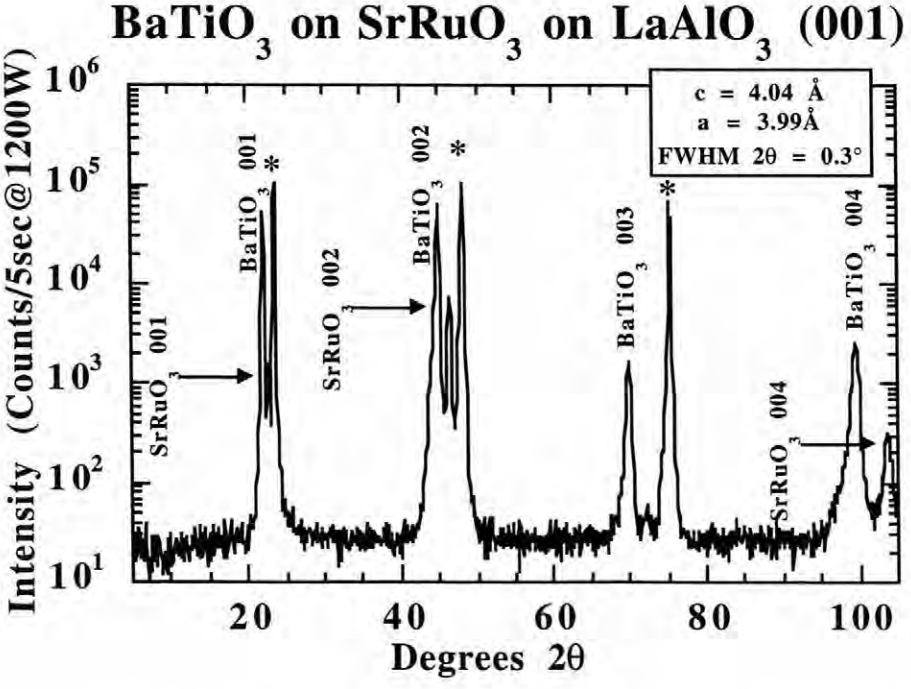

Figure 5.7: θ-2θ scan of BSL-series on-axis $SrRuO_3$ on-axis $BaTiO_3$ heterostructure

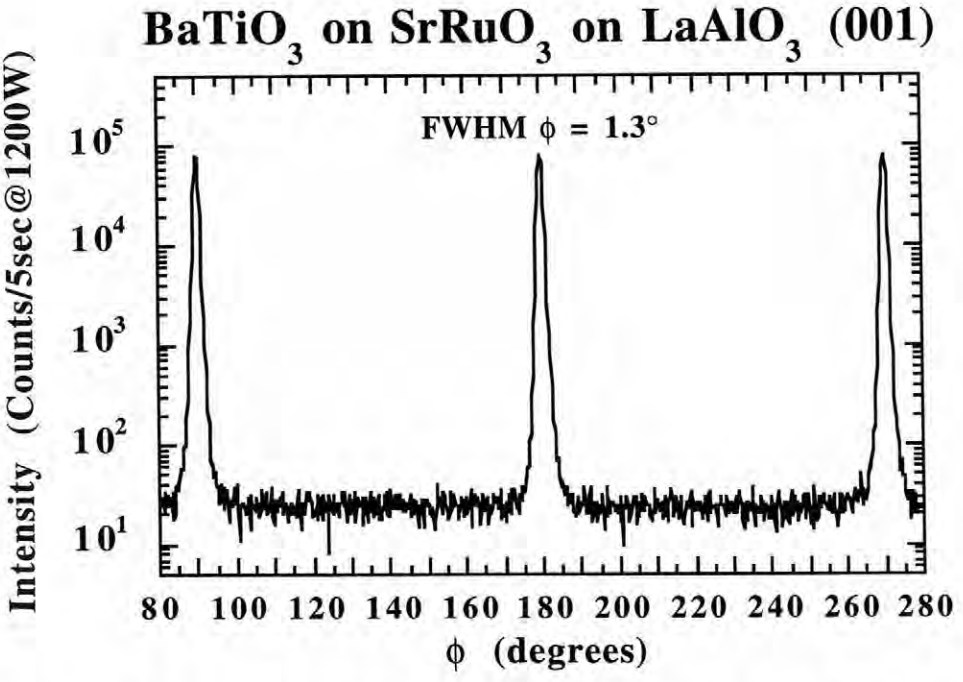

Figure 5.8: ϕ-scan of BSL-series on-axis $SrTiO_3$ on-axis $BaTiO_3$ (101) peak

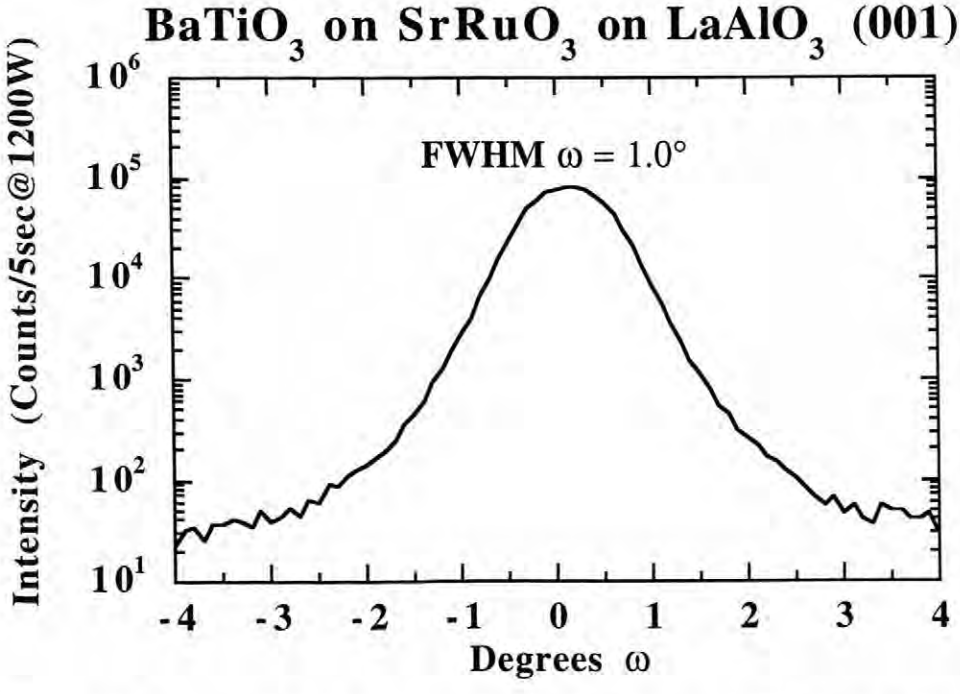

Figure 5.9: ω-scan of BSL-series on-axis $SrRuO_3$ on-axis $BaTiO_3$ (002) reflection

The preceeding series of x-ray diffraction patterns clearly illustrates the differences in crystallinity and epitaxy between laser ablated thin films deposited using both on and off-axis geometries. It should be noted that regardless of the deposition geometry, nearly identical temperature and pressure settings were maintained; approximately 680°C and approximately 150 mTorr oxygen/ozone mixture. In general, for the off axis case, when the pressures were reduced, the energy of the incoming particles increased and the epitaxy improved. However, experimental findings indicated that pressures in excess of 100 mTorr were necessary to increase the resistivity of the $BaTiO_3$ thin films. Thus, for films grown in our PLD system, it may be concluded that in the off-axis geometry the conditions conducive to highly crystalline films with beautiful epitaxial relationship to the substrate crystals may not be consistent with those conditions which produced films with optimized electrical properties. In the on-axis geometry, deposition under greater oxygen pressures could be carried out while conserving crystallinity and epitaxy. In this geometry, the pressure could be used to mediate the bombardment to an acceptable level.

After optimizing the epitaxy and crystallinity of the BSL heterostructures, other influential factors such as pressure and target-to-substrate distance were investigated. When the process conditions were changed such that the level of energetic bombardment was increased, i.e., reduction of pressure or target to substrate distance, the $BaTiO_3$ crystals were found to exhibit an anomalous structure. This anomalous structure was manifested in shifted, broadened and even split $BaTiO_3$ x-ray reflections. In all cases, films deposited under heavy bombardment conditions showed expanded lattice parameters. Figure 5.10 shows a θ-2θ section of a diffraction pattern for several BSS series heterostructures where energetic particle bombardment was varied.

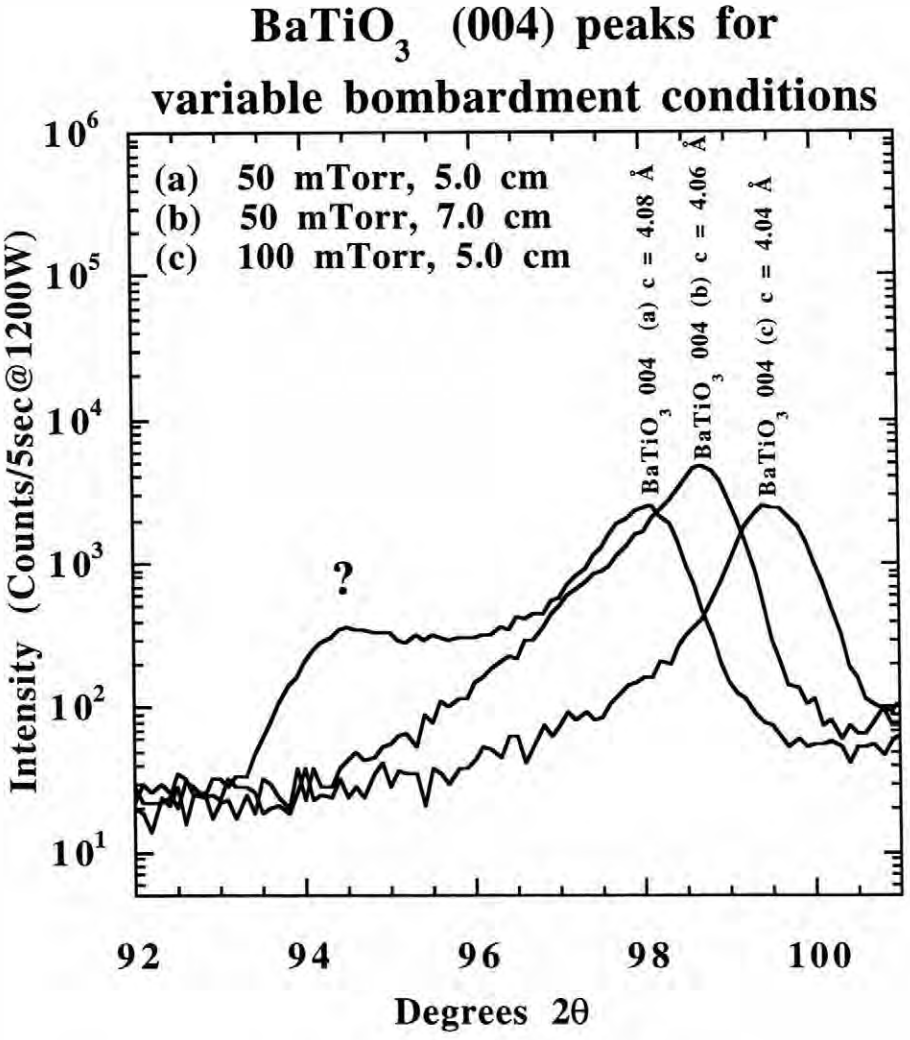

Figure 5.10: Trend in (004) peak position with increasing bombardment for $BaTiO_3$ films

For the $BaTiO_3$ sample prepared at 100 mTorr, (c), it is believed that enough scattering and thermalization of energetic particles occurred to reduce bombardment-induced damage, which allowed growth of $BaTiO_3$ with bulk lattice constants. In the other two samples the deposition conditions were modified to increase the level of bombardment by (b), decreasing pressure while making a small increase in the target to substrate distance, and

(a), decreasing the target to substrate distance while remaining at the reduced pressure. The actual pressure and target-to-substrate distances as well as the effects on the lattice constants and crystallinity are given in figure 5.10.

5.3 Morphology for the BSL and BSS heterostructure systems

The development of a thin film microstructure during low temperature and low energy deposition is a well known phenomena. Typically, when films are deposited at high temperatures, morphology is minimized due to the increased adatom mobility. However, in thicker $BaTiO_3$ (> 2000 Å), heterostructures deposited under low bombardment conditions in the off-axis geometry, microstructure was always observed. Even though the temperatures were high, ~ 0.5 T_m $BaTiO_3$, column-like structures were found and attributed to the enormous instantaneous deposition rate and the resulting lack of adatom mobility. Interestingly, even though the films had a cauliflower-like microstructure, by x-ray measurements, they appeared epitaxial in θ-2θ. Only when scanning in the phi-circle was it apparent that extra orientations existed. It is believed that the films initially grew epitaxially, but due to the large instantaneous particle flux, incoherent re-nucleation occurred and extra identical in-plane orientations evolved while the out-of-plane alignment was conserved.

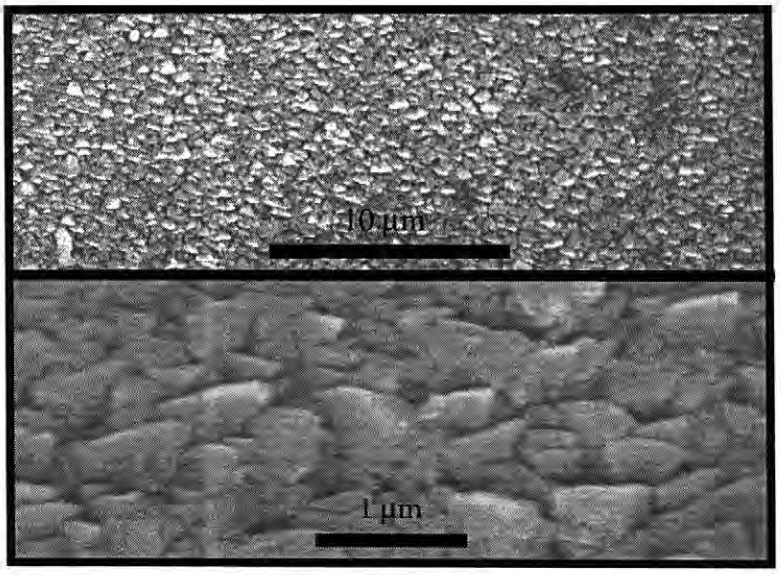

Figure 5.11: SEM image of columnar BSL-series heterostructure, both layers deposited off-axis, thickness ~ 2000 Å

When both heterostructure layers were deposited in the on-axis geometry, very smooth films were observed. The only difference between the growth of these films and the previous was the deposition geometry: temperature and pressure were held constant. The most important change was in the amount of particle bombardment. Both films were of similar thickness, ~ 2000 Å, with the on-axis film grown approximately 2 cm further from the target. This being the case, the well know structure zone model (SZM) can explain the absence of any obvious morphology. Figure 5.12 is an image of a BSL-series heterostructure with both layers deposited on axis.

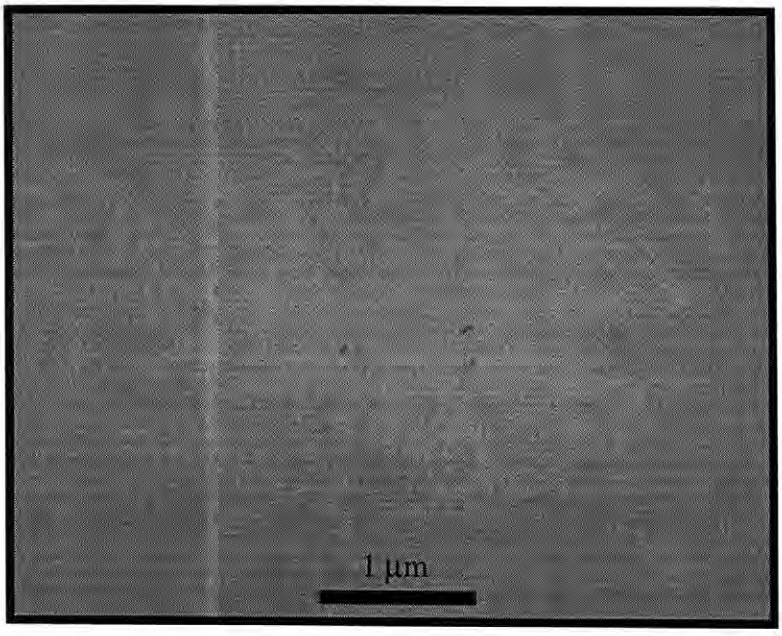

Figure 5.12: SEM image of smooth BSL-series heterostructure with both layers deposited on-axis

In addition, these heterostructures, which were absent of surface morphology detectable by SEM were truly epitaxial. The morphology/epitaxy relationship in laser deposited thin films was found to be quite dramatic.

5.4 Electrical property measurements

For the study of size-induced phase transitions, or the detection of a ferroelectric phase in BaTiO3, electrical property measurements provide the most convincing evidence. Typically, one of two things are required when attempting to verify the presence of ferroelectric: a reversible remanant polarization, (detected by a polarization hysteresis), or a maximum in the temperature dependence of the dielectric constant. In thin film form, measurement of these electrical properties can be quite difficult. From a practical experimental standpoint, physically measuring a thin film capacitor is non-trivial given the extreme thinness of the dielectric and the potential opportunity for shorting. In addition,

the electrodes and their electrical and chemical characteristics can severely influence the measured properties. The type of contact, as well as the electrode conductivity must be appropriate for reliable electrical property measurement and interpretation. In the present study, strontium ruthenate was used as an epitaxial bottom electrode. Many difficulties were encountered when attempting to measure the electrical properties, and it is believed that the electrical behavior of the $SrRuO_3$ was partly responsible.

Through-the-thickness electrical property measurements were performed on all BSS and BSL-series structures. The dielectric constant and its temperature dependence was measured using an HP 4274A LCR bridge in conjunction with an in-house designed conduction refrigerator/oven. Using an RT66A standard ferroelectrics measurement device the sample hysteresis was determined. In most cases, saturated polarization-electric field hysteresis loops were not obtained. Very often the loops were lossy, as indicated by rounded ends which became exaggerated as the driving voltage was increased. At the onset of this study, the exact correlations between electrical property measurements, crystallinity, and epitaxy were not fully understood. It would be expected that those samples with the best crystallinity and highest level of epitaxy would exhibit the best electrical properties given that such samples make the closest approximation to single crystal samples. Primarily through measurements of dielectric loss and resistivity, it was observed that the samples with poor epitaxial relationship to the substrate (which was most often coupled with a consequent decline in overall crystallinity) had the best insulative properties. It is proposed that the development of a thin film morphology including crystalline boundaries aided in the isolation of mobile carriers which were present in all films. The highly crystalline epitaxial films are expected to be more susceptible to such effects given that in such film structures physical boundaries which inhibit transport are not present.

For the discussion of the electrical properties of epitaxial $BaTiO_3$ thin films, three samples will be introduced. Table 4 gives pertinent sample information.

Table 4: Sample designation and description

Sample I.D.	Substrate	Thickness	FWHM (°) 2θ	φ	ω	Morphology	T_c (°C)	R.T. lattice parameters
BSS-12 om-axis	$SrTiO_3$	~ 2000 Å	0.3	0.9	0.5	Smooth	58	a = 4.00 c = 4.03
BSL-10 off-axis	$LaAlO_3$	~ 1000 Å	0.7	1.5	*	Grainy	- 10	a_o = 4.01 (cubic)
BSL-18 on-axis	$LaAlO_3$	~ 1800 Å	0.6	1.9	1.0	Smooth	- 35	a_o = 4.01 (cubic)

* Extra orientations were observed

All samples were electrically characterized with capacitance versus temperature and polarization hysteresis measurements. The field dependence of the resistivity and leakage current was measured for samples BSL-18 and BSS-12. Direct comparisons relating to and explaining size effects will be made between samples BSS-12 and BSL-18. The sample designated BSL-10 is excluded from that discussion since, unlike the other samples, the $BaTiO_3$ layer was deposited in the off-axis geometry, hence the assumption of similar composition and morphology to on-axis deposited sample cannot be substantiated. Compositional measurements by RBS and DCP spectroscopy on $BaTiO_3$ samples grown under conditions similar to BSS-12 and BSS-18 confirm that the stoichiometry was similiar to within the limits of experimental error. For the on-axis deposited material, the barium to titanium ratio was repeatedly found to be less than unity. All compositional measurements indicated an approximate barium deficiency of 3 % (± 5 %). Even though the $BaTiO_3$ samples are non-stoichiometric, the barium deficiency should not affect the size effects interpretation. The Curie point of undoped $BaTiO_3$ has been found to be unaffected by

excess TiO_2. However, significant lowering of the maximum value of the dielectric constant to ~ 2400 has been observed in samples 4% TiO_2 rich [Sharma *et al.*, 1981, and Muratami and Yamaji, 1972]. Undoubtedly, the barium deficiency contributed to the large dielectric loss observed in all samples, since each excess titanium site should be accompanied by both a barium and oxygen vacancy for charge compensation. In theory, if a three percent deficiency were the case, the oxygen vacancy concentration would be ~ 4.65 x 10^{26} $V^{\bullet\bullet}_o/m^3$. Figure 5.13 is a current voltage curve measured with the RT66A ferroelectric test device. For the sake of comparison between measurements, it is important to note that the a.c. frequency used when measuring both hysteresis and leakage current was the same.

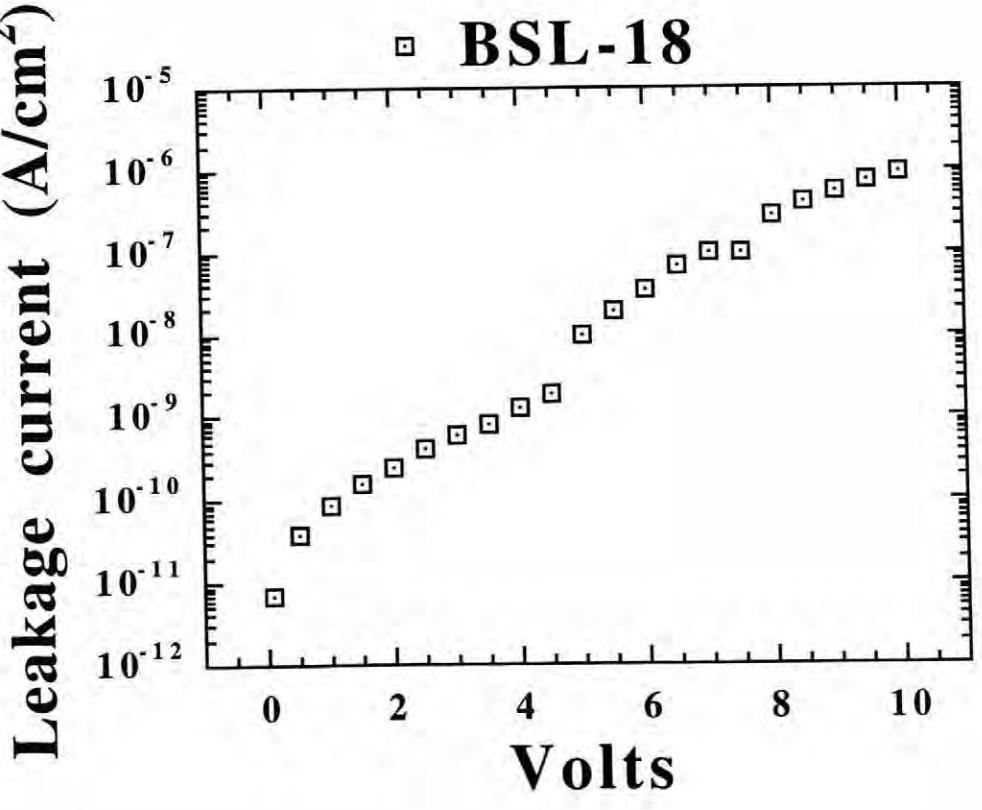

Figure 5.13: Current voltage characteristics for sample BSL-18

Figure 5.13 illustrates the significant voltage dependence of the conductivity which spans > 5 decades of current over 10 applied volts. From comparison to previous work, it is likely that the mode of conductivity in the $BaTiO_3$ samples was a charge hopping mechanism, where field enhanced current is observed [Maffei, 1993, and Kuroiwa *et al.*, 1994]. This mechanism relies upon the presence of electrons in traps, which in the presence of the appropriately strong electric field can hop between sites. The oxygen vacancies in the off-stoichiometry $BaTiO_3$ samples can serve as these traps. Doubly and singly charged vacancy traps are established in the band gap as acceptor levels with energy states 1.3 and 0.3 eV below the conduction band respectively [Daniels and Heardtl, 1976]. Figure 5.14 is a plot showing the best fit linear relationship between Log current and the applied electric field

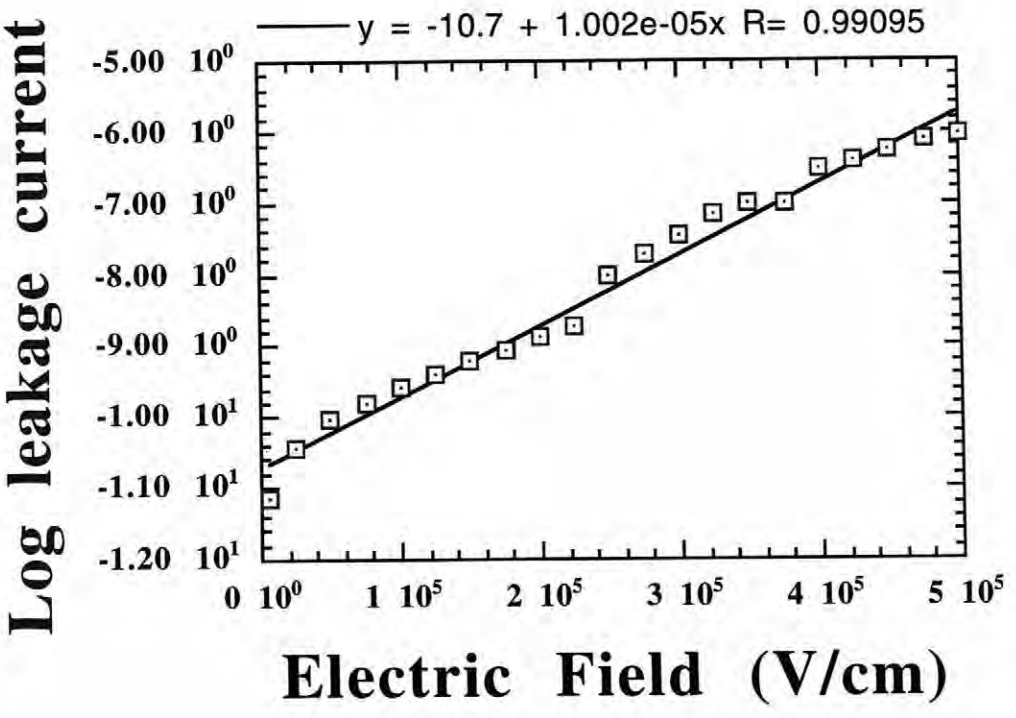

Figure 5.14: Linear relationship between Log leakage current and applied electric field

The hopping current can be expressed by the following equation.

$$J = J_o \exp\left(\frac{\beta_{ES} E}{kT}\right)$$

J = current density

J_o = Initial current density

$\beta_{ES} = (q^3/\pi\varepsilon)^{1/2}$

q = charge on carrier

ε = permittivity

E = applied electric field

k = Boltzmann's constant

T = absolute temperature

Taking the log of both sides reveals the linear relationship demonstrated in figure 5.14. Judging from the close linear fit to the experimental data, it is likely that this mechanism is responsible for conduction in these films. Another possibility for conduction would be a Poole-Frenkel mechanism in which case the linear relation would be between Log current and the square root of the applied electric field. Such a fit was attempted, but the calculated linear fir was not as good as that calculated for the charge hopping mechanism.

Measurements of the dielectric constant and loss as a function of temperature were performed on all three samples. Figure 5.15 shows the temperature dependence of the dielectric constants and loss of BSS-12 and BSL-18.

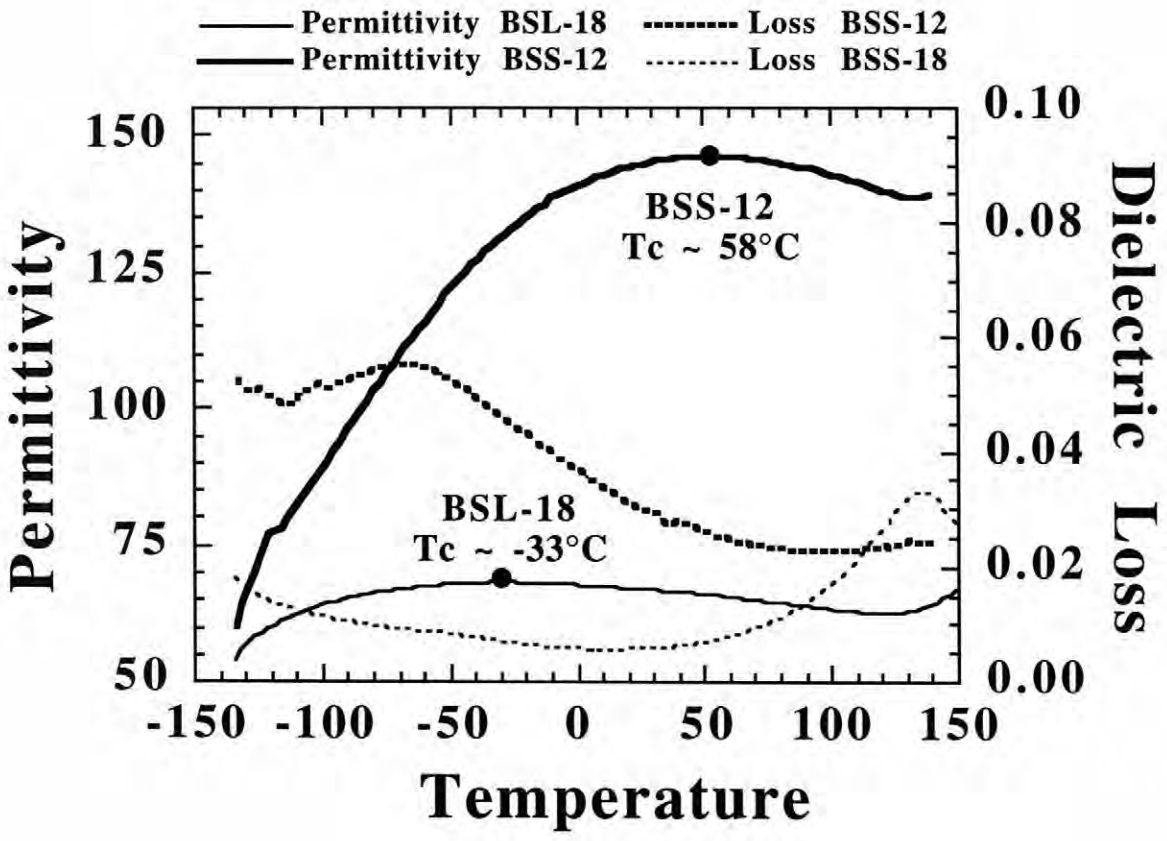

Figure 5.15: Temperature dependence of Permittivity of BSS-12 and BSL-18, measurement taken @ 10 kHz

Neither sample shows a Curie transition at the bulk temperature value of 130°C, however, between the samples a transition temperature difference of 93° exists. Considering all of the differences between the samples, the most striking is the degree of crystallinity and epitaxy. Data quantifying the crystallinity and degree of epitaxy is listed in table 5. The largest influence on the crystallinity and epitaxy of these films is the substrate material. As expected, the $BaTiO_3$ deposited on $SrTiO_3$ should form a much better crystal than that deposited on $LaAlO_3$. Chemically, there should be no difference, as in both cases, the $BaTiO_3$ is separated from the substrate by a layer of $SrRuO_3$.

To further quantify the crystal's quality, the Williamson-Hall method of determining coherent crystal length was applied. The Williamson-Hall method was used since it incorporates a family of reflections and their full width half maximum values, hence accounting for the presence of microstrain and its contribution to x-ray line broadening [Williamson and Hall, 1953]. Table 5 lists the result.

Table 5: Coherence length determination data

Sample Identification	Coherence length (Å)	Microstrain
BSS-12	800	0.43 %
BSL-18	370	0.54 %

While application of the Williamson-Hall method gives information concerning the crystallinity of the film, as well as the crystal's coherent length, for an oriented system, the interpretation is not straightforward. For an epitaxial film, broadening in 2θ is only indicative of the coherence length normal to the substrate. It is possible that disorder exists in a direction perpendicular to the {00l} normal, or in any other non-normal direction which will remain unaccounted for. With these considerations in mind, the calculated values should not be used to establish an absolute size, but certainly do support the trend of decreasing crystallinity. However, given the single crystal nature of the samples and the geometry of the electrodes, the measured electrical properties may also be less sensitive to disorder in directions which are non-normal to the substrate surface. Owing to this, the coherence length determined by the Williamson-Hall method may be indicative of the sizes being probed by the electrical property measurents used.

Considerable differences are present in the epitaxial relationship to the substrate between the two samples, and it can be easily imagined that this type of epitaxy induced disorder can influence the coherent lattice dimension. However, line broadening in x-ray

scans which probe this disorder, i.e., rocking curves and phi-scans, cannot be used to calculate a coherence length since these scans occur at one fixed 2θ value. These measurements, with respect to the substrate crystal, indicate the angular misalignment of subcrystallite blocks present in the film. Figure 5.16 gives a schematic representation of these subcrystallite blocks and how they orient, or misorient with respect to the substrate.

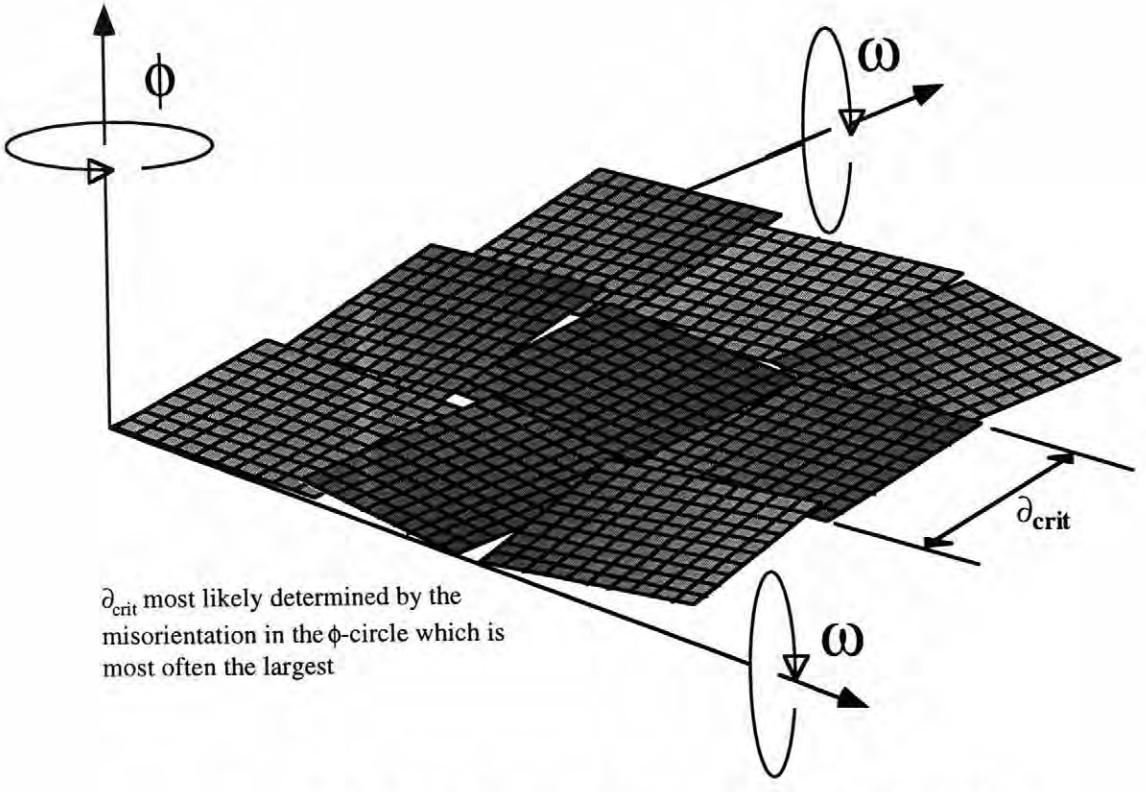

Figure 5.16: Mosaic structure representation in an epitaxial film

Considering a tetragonal film growing with its c-axis normal to the substrate surface, misorientations in ω indicate that the [001] directions of both film and substrate are not parallel, rather they are tilted away from one another. Such misorientations could be thought to contribute to crystalline disorder in both in and out-of-plane directions. For the same system, misorientations in the ϕ-circle represent the case where the [010] or [100]

directions of the film and substrate are non-parallel. This type of crystalline disorder occurs in the plane of the film, hence does not contribute to the peak broadening in 2θ. As shown in table 5.2, the FWHM values in all three circles are narrower for the case of BSS-12. Certainly, by examination of the x-ray data, the case could be made that the crystallinity and epitaxy of BSS-12 is superior to that of BSL-18, hence it displays electrical properties which are closer to bulk values.

From examination of the temperature dependence of the dielectric constant and dielectric loss, the conductivity of the films was observed to increase with temperature. Increasing the temperature supplies the necessary energy to promote trapped electrons into the conduction band. To be certain that the observed transitions in the dielectric constant were not an artifact of the increasing loss, which can cause an artificial rise in K, hysteresis loops were measured as a function of temperature and voltage. Low field hysteresis loops were taken in order to minimize the effects of film conductivity. Figure 5.17 shows the hysteresis data for BSS-12 at high and low fields, as well as at low and room temperatures. The low field data confirms that at room temperature and at 77 K the film is ferroelectric as evidenced by a reversible remanant polarization. The room temperature remanant polarization is lower than the low temperature value for the same low field because of the proximity to the transition. The fact that the polarization decreases with increasing temperature indicates that a transition is being approached. If the observed maxima in the dielectric constant were only due to an increase in the loss, the polarization would tend to increase with temperature rather than get smaller for the same applied field. The determination of the room temperature ferroelectricity by electrical property measurements is consistent with the x-ray data, which found the room temperature lattice constants to be 4.03 Å and 4.00 Å. The higher field, room temperature curve illustrates the inflated loss of the sample under large electric fields. The asymmetry in the hysteresis loop is associated with the fact that the top and bottom electrodes were different materials. This was

confirmed by reversing the asymmetry when the polarity of the electrodes was reversed. The top and bottom electrodes were different in both conductivity and contact potential.

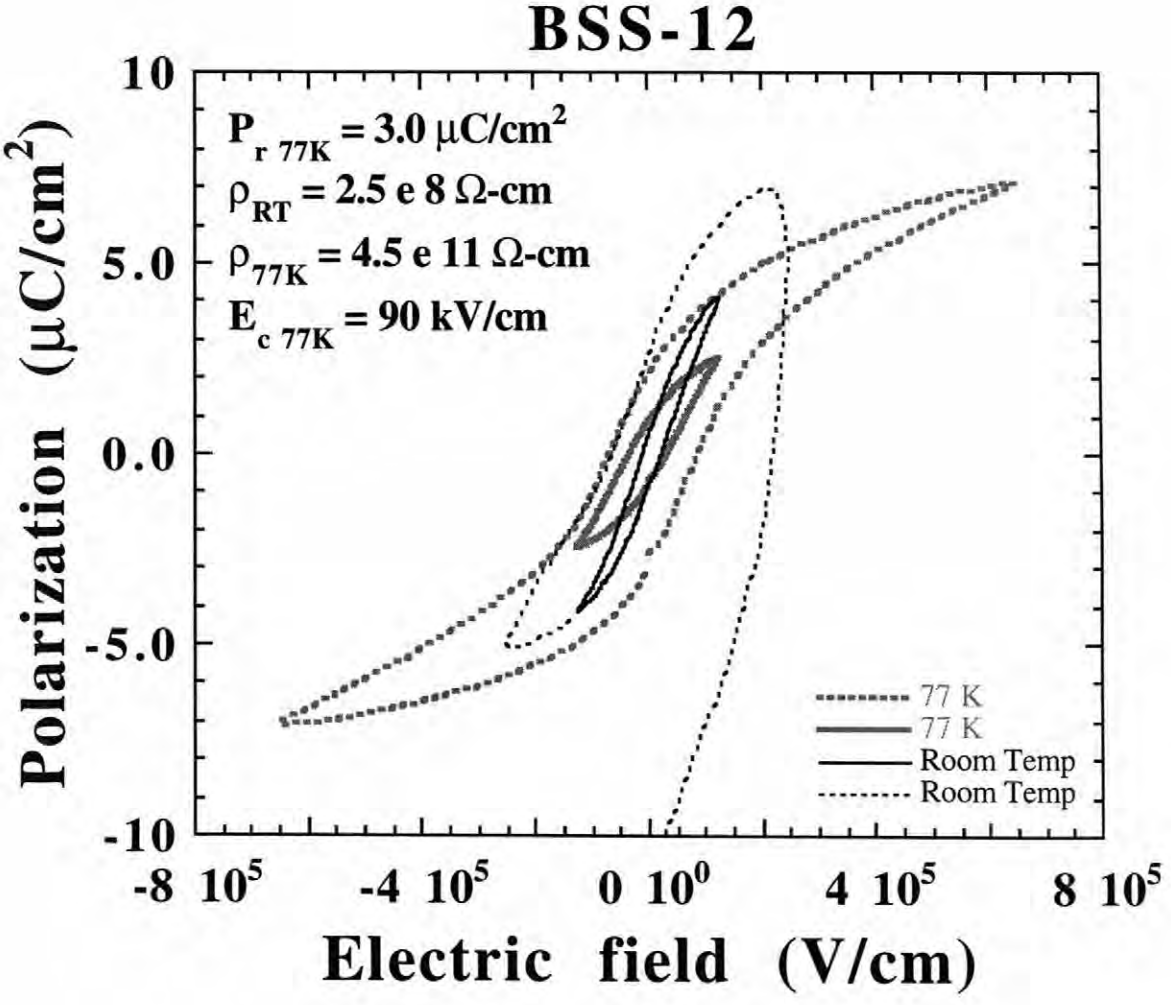

Figure 5.17: Field and temperature dependent polarization hysteresis curves for BSS-12

The same experiments were made for BSL-18 which was found to have a maximum in the dielectric constant at a temperature of ~ -38 °C. Once again, low field polarization hysteresis measurements were performed, confirming the presence of a real transition. At room temperature, no hysteresis was observed for an applied voltage of 5 V. Though very small, differences do exist between the 77 K and room temperature hysteresis curves taken at 5 volts maximum applied voltage. Large differences in polarization were not expected given the relatively small changes in the permittivity with temperature. As compared to BSS-12, the low field low temperature polarization values were found to be considerably smaller given the same applied voltage. This was not unexpected since under the influence of a size induced transition, the coercive field typically increases, thus larger fields are required for the observation of similar values of polarization. Also, since the transition temperature of this sample was depressed even further than in the previous film, larger reductions in the saturation and remanant polarization values would be expected. At 77 K, a hysteresis loop was observed with a remanant polarization of ~ 2 $\mu C/cm^2$. This result is again consistent with the presence of a size induced transition when compared to BSS-12, which had a remanant polarization of ~ 3 $\mu C/cm^2$. The coercive field of BSL-18 was calculated to be 170 kV/cm, which is approximately a factor of two larger than calculated for BSS-18. Figure 5.23 shows the polarization hysteresis curves for BSL-18.

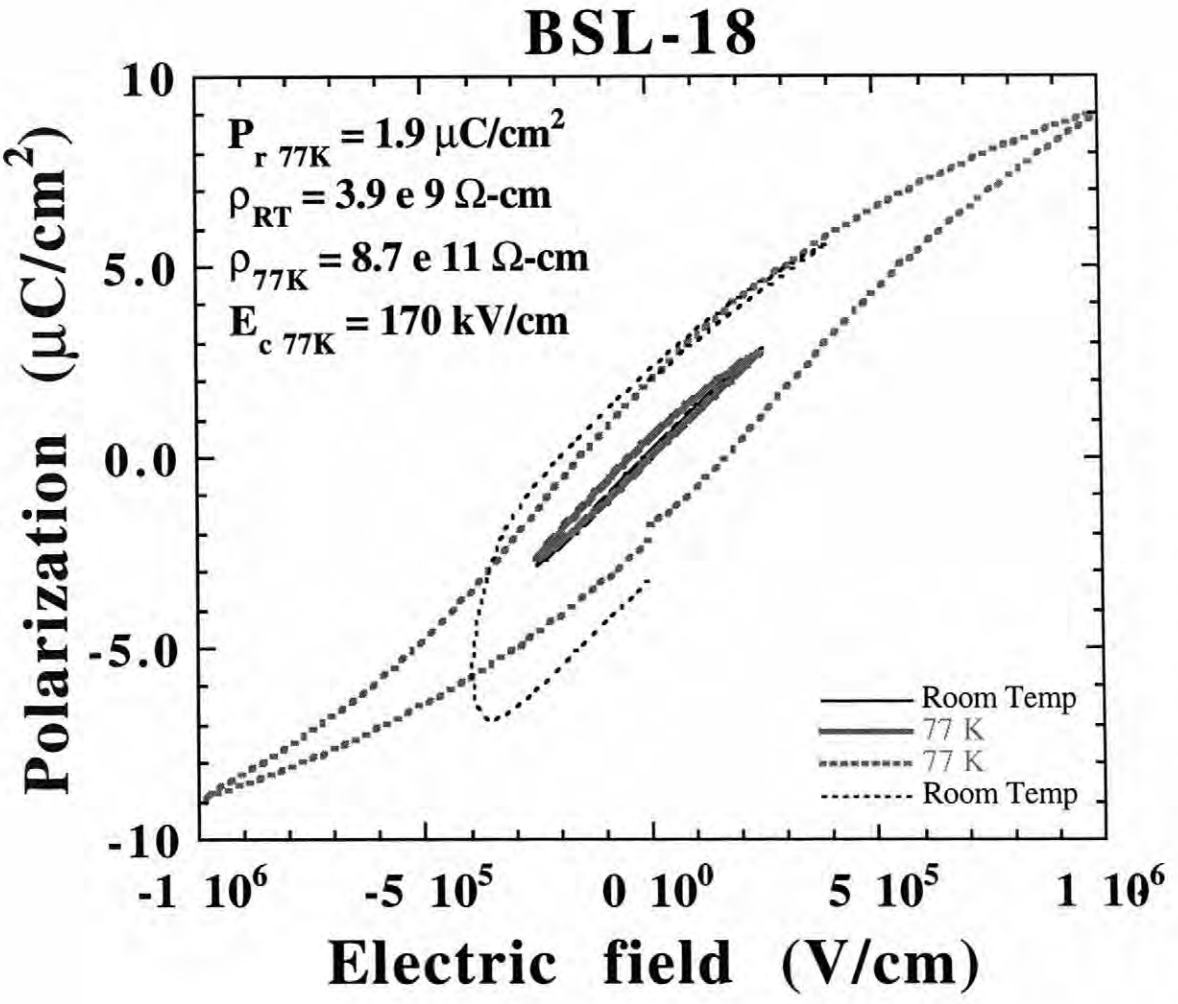

Figure 5.18: Field and temperature dependent polarization hysteresis curves for BSL-18

Table 6: Summary of the electrical property data obtained for BSS-12 and BSL-18.

	BSS-12	BSL-18
T_c	58 °C	- 35 °C
K_{max}	~ 150	~ 65
P_r - Low V, Low T ($\mu C/cm^2$)	0.90	0.4
P_r - Low V, High T ($\mu C/cm^2$)	0.55	0.0
E_c - Low V, Low T (kV/cm)	33	64
E_c - Low V, High T (kV/cm)	23	0.0
P_r - High V, Low T ($\mu C/cm^2$)	3.0	1.9
E_c - High V, Low T (kV/cm)	90	170

Finally, the electrical properties of the third sample, BSL-10 were measured. It is suspected that either the composition of this sample was closer to stoichiometric, or the morphology supressed conductivity since the dielectric constant and loss decreased constantly above the Curie transition (which was found to occur at -10 °C) for the temperature range investigated. Though the temperature dependence below the Curie transition was found to behave similarly to the other samples below the transition, the differences in morphology and deposition conditions preclude direct comparison. Due to the more resistive nature of $BaTiO_3$ and the resultant drop of the measured dielectric constant above T_c, this sample could be modeled for the presence Curie-Weiss behavior. The linear relationship between the inverse permittivity and temperature above the ferroelectric transition is known as Curie-Weiss behavior. The reduction in K is governed by changes in the soft mode lattice vibrations in the crystal, hence, according to Curie-

Weiss theory, the rate of decrease of inverse permittivity with temperature should be well defined. The Curie-Weiss law is expressed in equation form as the following [Herbert, 1985]:

$$K = \left(\frac{C}{T - T_o} \right)^{\gamma}$$

where C = Curie constant

T = Absolute temperature

T_0 = Curie-Weiss temperature

The exponent γ is unity when the material displays true Curie-Weiss behavior. Thus, determination of the gamma coefficient for a material is a reasonable indication of Curie-Weiss behavior. By application of standard scaling theory to the temperature dependence of the dielectric constant above T_c the gamma-exponent may be determined. The following relationship applies:

$$K(T) = K_o \left(\frac{T - T_c}{T_c} \right)^{\gamma}$$

$$Log(K(T)) = \gamma \, Log\left(\frac{T - T_c}{T_c} \right) + Log(K_o)$$

where γ is the slope of the linear portion above T_c

These calculations were performed for sample BSL-10 and a gamma-coefficient of 0.6 was calculated. If the model used to arrive at this value is valid, the implication is that this sample, and possibly all barium titanate samples showing a size-induced transition break from Curie-Weiss behavior. However, if the transition temperature used to calculate the gamma exponent was incorrect a false value will result. In samples such as BSL-10 where

the transition temperature is not well defined, such errrors would be prevalent. A fractional gamma exponent does not necessarily indicate the presence of a size induced transition.

In addition to calculation of gamma, the Curie constant was calculated from the high temperature data. A value of 14,000 K^{-1}resulted, which is approximately one order of magnitude smaller than commonly reported value of 1.6 x 10^5 K^{-1} for $BaTiO_3$ [Cross, 1995]. Figure 5.19 shows the temperature dependence of the dielectric constant.

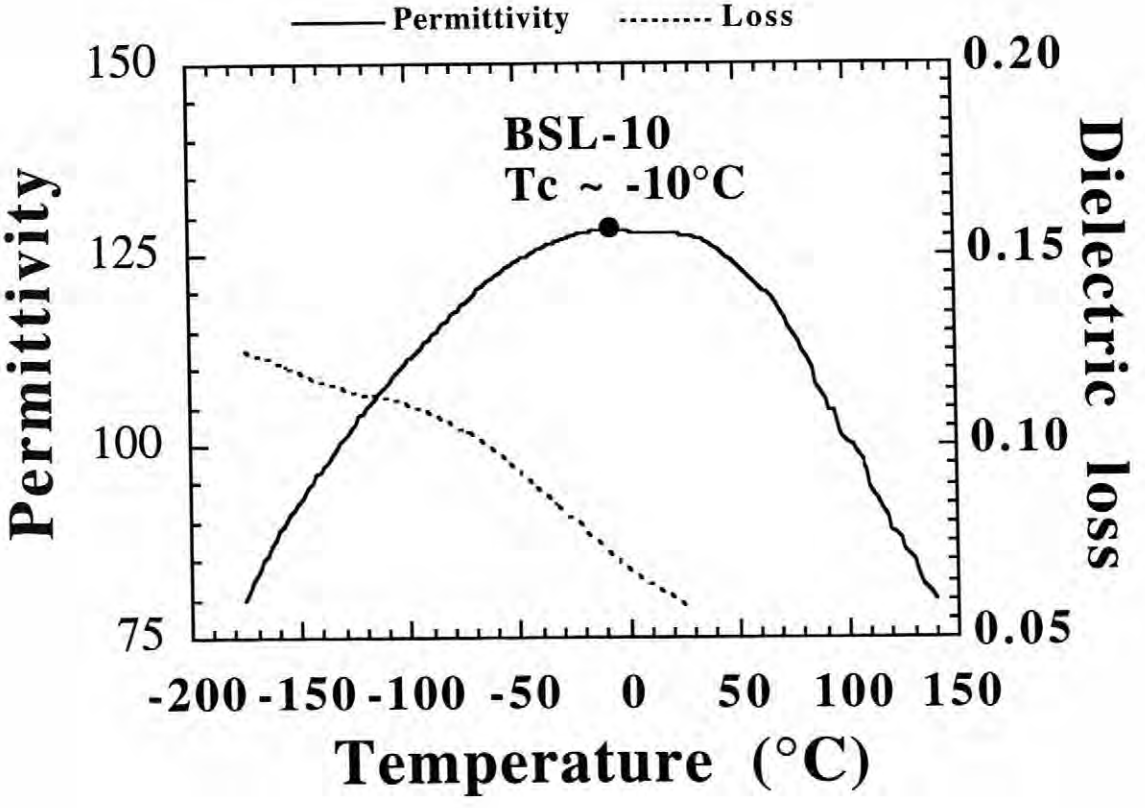

Figure 5.19: Temperature dependence of the dielectric constant of BSL-10 measured @ 10 kHz

Figures 5.20 and 5.21 show the linear fits to the high temperature dielectric constant data for both the Curie-Weiss analysis and the application of standard scaling theory.

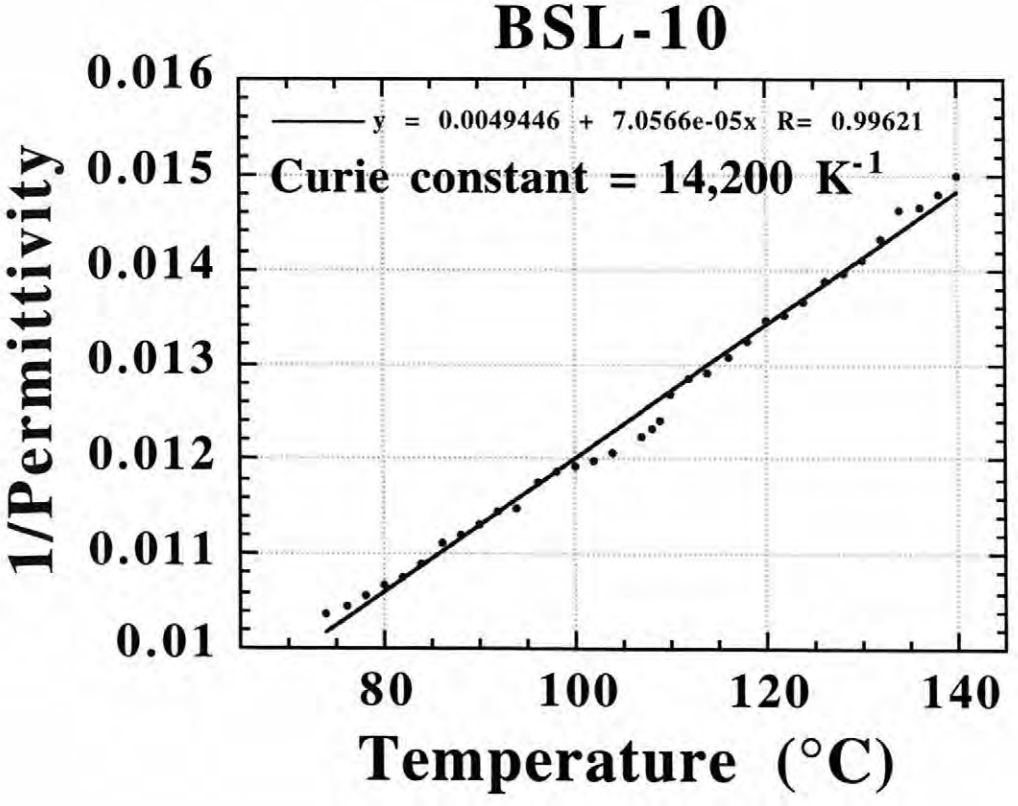

Figure 5.20: Curie-Weiss plot for BSL-10

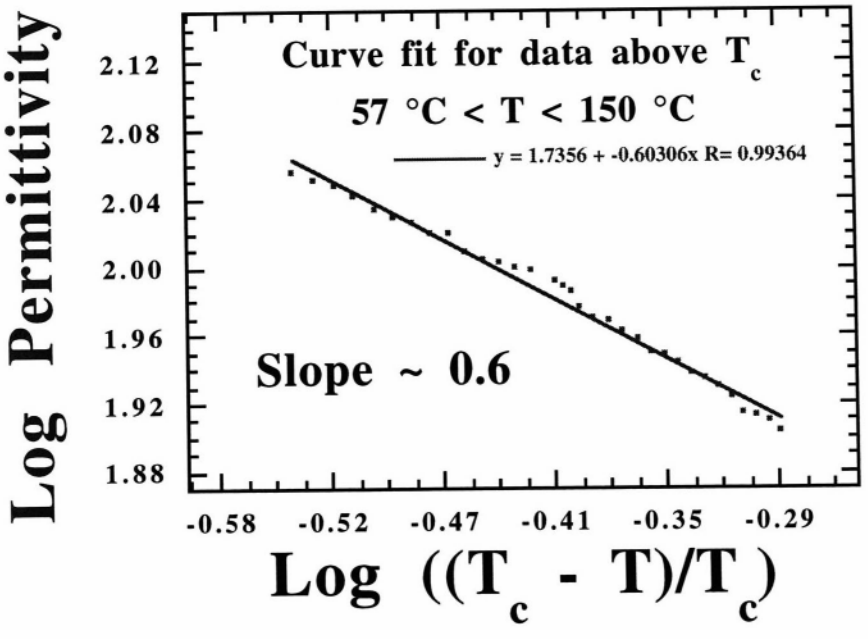

Figure 5.21: Application of scaling theory for the determination of gamma

Upon examination of figures 5.20 and 5.21 it becomes clear that the barium titanate film is not behaving in accordance with classical theory. The calculated Curie-Weiss coefficient is off by an order of magnitude and the critical exponent, gamma, is fractional. In an attempt to explain this, the possibility of a parasitic non-ferroelectric layer between film and substrate with negligible temperature dependence of capacitance was considered. Table 7 shows the results from a simulation of the dielectric response upon addition of a 20 Å thick reaction layer. Though the magnitude of the dielectric constant decreases, as was observed in the experimental data, the shape of the curve and the position (in temperature) of the transition remain unchanged. However, when extrapolating to obtain the Curie-Weiss temperature it is found that the lower the permitivity of the additional layer, or the

greater its volume fraction, the lower T_0 becomes. This is in agreement with the experimental data of BSL-10 where the T_0 was less than T_c by ~ 70°C. The Curie-Weiss constants calculated from the simulated films change neglibly for a layer of constant thickness with variable dielectric constant, and increase for a layer of constant permittivity with increasing thickness. This result, as well, does not support the trends observed in the experimental data. Though it is likely that a layer too thin to be detected by x-ray diffraction is present between the $BaTiO_3$ and the $SrRuO_3$, alone, such a layer cannot account for all of the features observed in the permitivity's temperature dependence. Quite possibly, a thin reaction layer is present in addition to an intrinsic size effect.

Table 7: Simulated dielectric response of $BaTiO_3$ film upon addition of a parasitic capacitive layer of variable permittivity and volume fraction

Volume Fraction Parasitic Layer K = 100	C (K^{-1})	T_0 (°C)	γ	Dielectric Constant Parasitic Layer VF = 1%	C (K^{-1})	T_0 (°C)	γ
0	145412	100	0.62	0	145412	100	0.62
0.01	161576	70	0.20	100	146993	72	0.20
0.02	181765	-270	0.10	50	146993	-230	0.12
0.03	207731	-532	0.07	10	146993	-1524	0.03

Though barium titanate thin films which exhibited bulk properties were not able to be prepared, room temperature ferroelectricity was observed in samples as thin as 2000 Å with crystalline coherence lengths of approximately 75 nm. As well, samples with ferroelectric transitions depressed to temperatures ~ - 35° C were prepared. The critical

differences between the samples seems to be a combination of the crystalline quality and the quality of the epitaxial relationship between the film and substrate.

5.5: $SrRuO_3$ deposition as an oxide bottom electrode:

Because it is believed that the electrodes played some role in the observed properties of films, additional work was undertaken to investigate some characteristics of the conductive oxide electrodes.

Strontium ruthenate is a pseudo-perovskite crystal with a lattice constant a_o of 3.93 Å in the bulk. In single crystal form, $SrRuO_3$ has a resistivity of ~ 270 μΩ-cm, categorizing it as a poor metal [Bouchard and Gillson, 1972]. $SrRuO_3$ conducts as a result of d-orbital overlap between adjacent Ru^{4+} ions via 2p orbitals of the near neighbor oxygens. The effect of this overlapping is a partially filled valence band and metallic conductivity [Burdett, 1995]. Due to its perovskite structure and lattice constants, this material makes an ideal epitaxial electrode for many mixed oxides.

$SrRuO_3$ has been successfully grown on $SrTiO_3$ and $LaAlO_3$. Attempts to deposit $SrRuO_3$ on MgO (001) were made, but only oriented films resulted. Highly crystalline films were easily deposited on $SrTiO_3$ and $LaAlO_3$, with the best structure occurring at temperatures near 680°C. It has been reported that at temperatures greater than 700°C $SrRuO_3$ will evolve Ru, thus those temperatures were not investigated [Eom, 1996].

An unexpected dependence upon deposition pressure was found with $SrRuO_3$ films when deposited in the on-axis geometry. It was observed that at low pressures, typically less than 50 mTorr, the crystallinity and electrical properties of $SrRuO_3$ changed dramatically. The unit cell of strontium ruthenate extended along both axes, but much more so out-of-plane. Accompanying this lattice swelling was a drop in the conductivity. The most important variables which change as a function of pressure during pulsed laser deposition are the supply of oxidant and the degree of energetic bombardment. Certainly, when the pressure is reduced by 130 mTorr, both of these variable change substantially.

The mean free path of a free atom produced by the laser solid interaction can be approximated with the following relationship:

$$l = \frac{1}{\sqrt{2}\pi a^2 n} \quad \text{....} \qquad \text{[Smith, D. L. , 1995]}$$

where:

a = particle diameter

n = gas concentration

l = mean free path

Note that the determination of a true mean free path (MFP) in laser ablation is not as straightforward as in the case of sputtering due to the uncertainty of the actual pressure in the vicinity of the laser plasma. The mean free path calculations below assume that the pertinent pressures in determining a MFP are those of the chamber ambient, however, the actual pressure between the target and substrate during the laser pulse may be quite different. As such, the qualitative comparison between different pressures should still be valid even though the magnitudes may be incorrect. For a barium atom, (corrected for an energy dependent collision cross section) the mean free path at 50 mTorr was calculated to be ~6 mm, while the mean free path for the same atom under 160 mTorr would be 1.5 mm. Considering a target to substrate separation distance of 7.0 cm, the barium atom would undergo approximately 14 collisions at 50 mTorr and 50 collisions under 160 mTorr. If the gas collisions are treated as elastic, then the assumption of linear energy loss with pressure could be made and a ~200% reduction in kinetic energy between low and high pressure conditions would be expected [Smith, D. L. , 1995]. For the case of laser ablation of YBCO, the kinetic energies of the copper species in both vacuum and 200 mTorr oxygen have been measured. Under vacuum, by time of flight mass spectrometry, Cu^{2+} ions were found to have energies of approximately 35 eV [Zhang *et al.*, 1989] while in a background pressure of 200 mTorr, by intensified CCD array photography, the

energies of the Cu^{2+} species were found to be 0.25 eV. The 35 eV energy value obtained for the case of ablation in vacuum is certainly sufficient to cause surface damage as 35 eV is greater than the bond strength of many materials [Smith, D. L., 1995]. The 0.25 eV value obtained for the case of ablation under 200 mTorr is similar to the energy of an evaporated species, which would not impart damage to the growing film.

Figures 5.22 through 5.24 show overlay x-ray diffraction plots of two on-axis deposited $SrRuO_3$ fims at pressures of 20 mTorr and 160 mTorr.

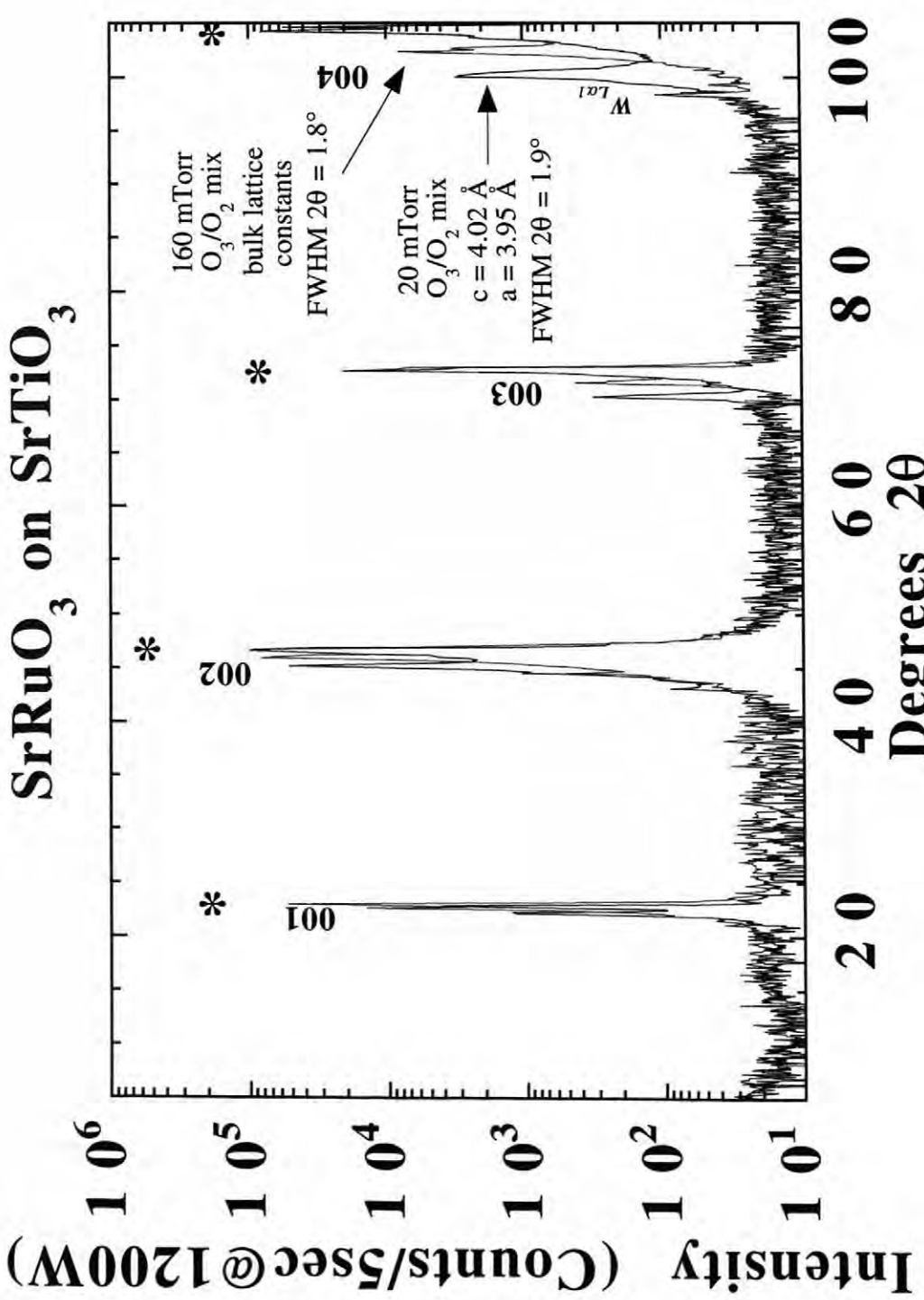

Figure 5.22: θ-2θ scan high and low pressure deposited $SrRuO_3$

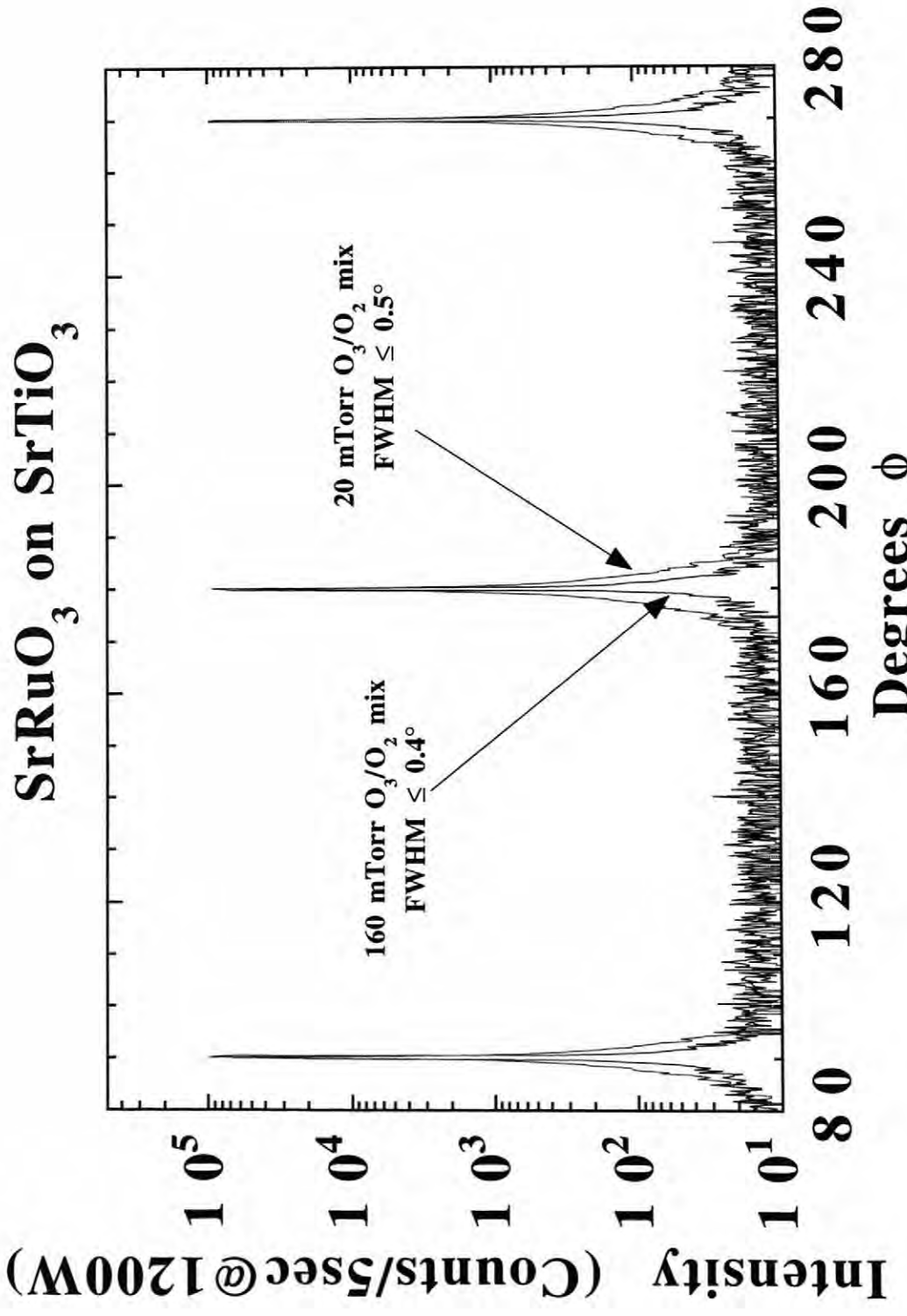

Figure 5.23: ϕ scan of high and low pressure deposited deposited $SrRuO_3$

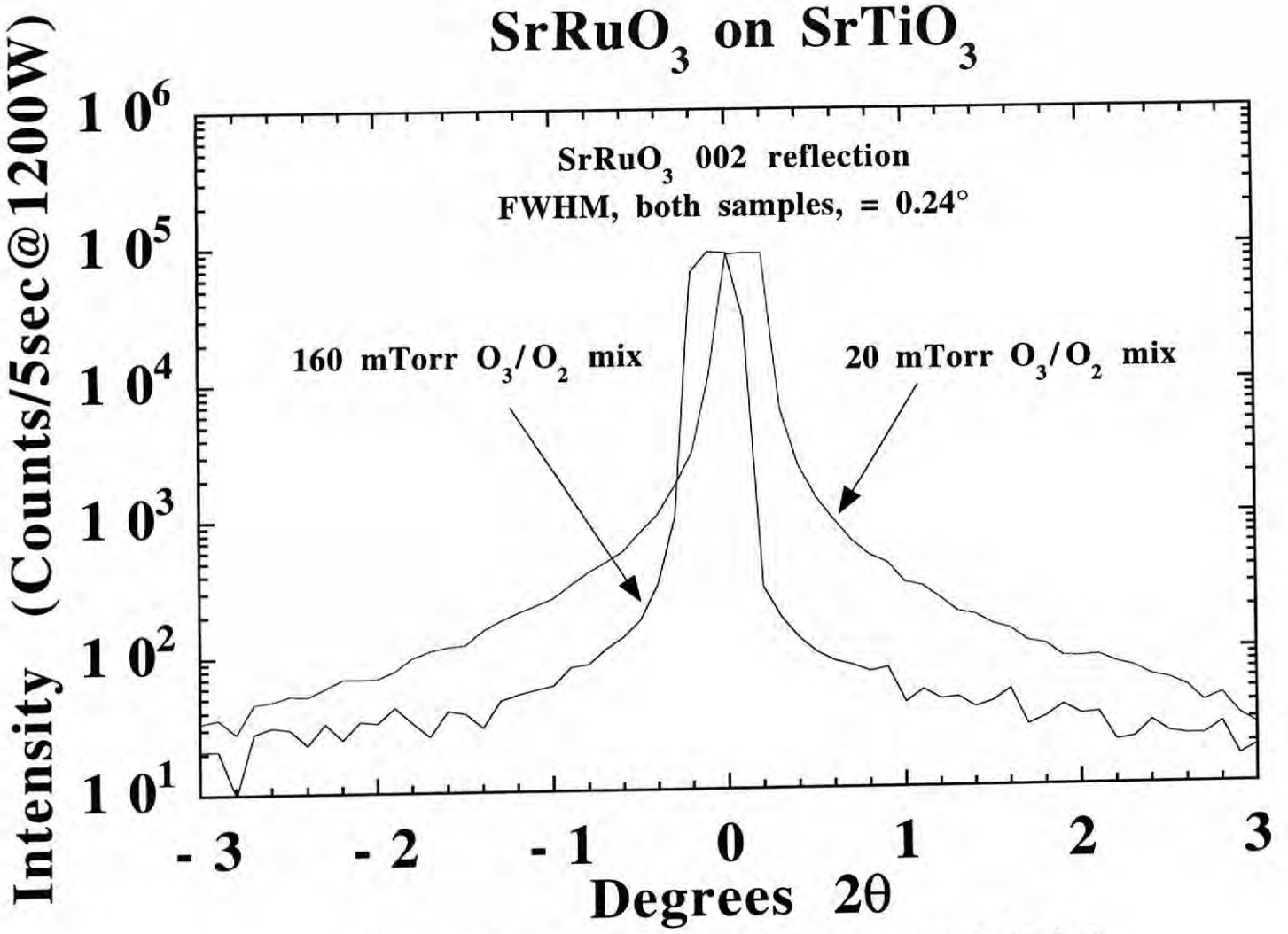

Figure 5.24: ω-scans of high and low pressure deposited $SrRuO_3$

The measured lattice constants of the high pressure deposited $SrRuO_3$ show the film to be cubic and similar in magnitude to the bulk, while those of the low pressure deposited $SrRuO_3$ show the film to be tetragonal with an in-plane constant of 3.95 Å and an out-of-plane constant of 4.02 Å. The lattice was found to have been swelled by approximately 3.3 % with respect to bulk strontium ruthenate.

From these figures it is also easy to see that the high pressure grown film is structurally superior to that grown at lower pressures. Not only are the FWHM values smaller for each circle, but the level of background noise is considerably larger for the low pressure film, this being indicative of increased crystalline disorder.

From this data it is unclear as to the cause of these film characteristics since the supply of oxidant and the degree of energetic bombardment are changing simultaneously and cannot be directly decoupled. In an attempt to elucidate the cause of the structural anomaly, a $SrRuO_3$ film was deposited off-axis at low pressures with all other conditions held constant. Deposition in the off-axis geometry should significantly reduce the energetic bombardment as the amount of material which can reach the film via a line-of-sight path is nearly eliminated. Figures 5.25 shows the x-ray diffraction data.

In the theta-two theta diffraction pattern two sets of peaks are present. The adjacent film peaks have been assigned the identical indices with the exception of "primes" which are meant to indicate that those reflections are due to a second phase. Diffraction patterns were taken in the other two circles for both phases but are not shown. These patterns indicate that both of the phases are epitaxial with the substrate. Off-axis scans were also performed in order to determine whether the extra peaks were indeed due to an extra phase or were simply indicative of a tetragonal cell which had twinned orientations. When the off-axis peaks were investigated, the measured d-spacings and their relative orientations and intensities supported the interpretation of multiple phases rather than orientational twinning.

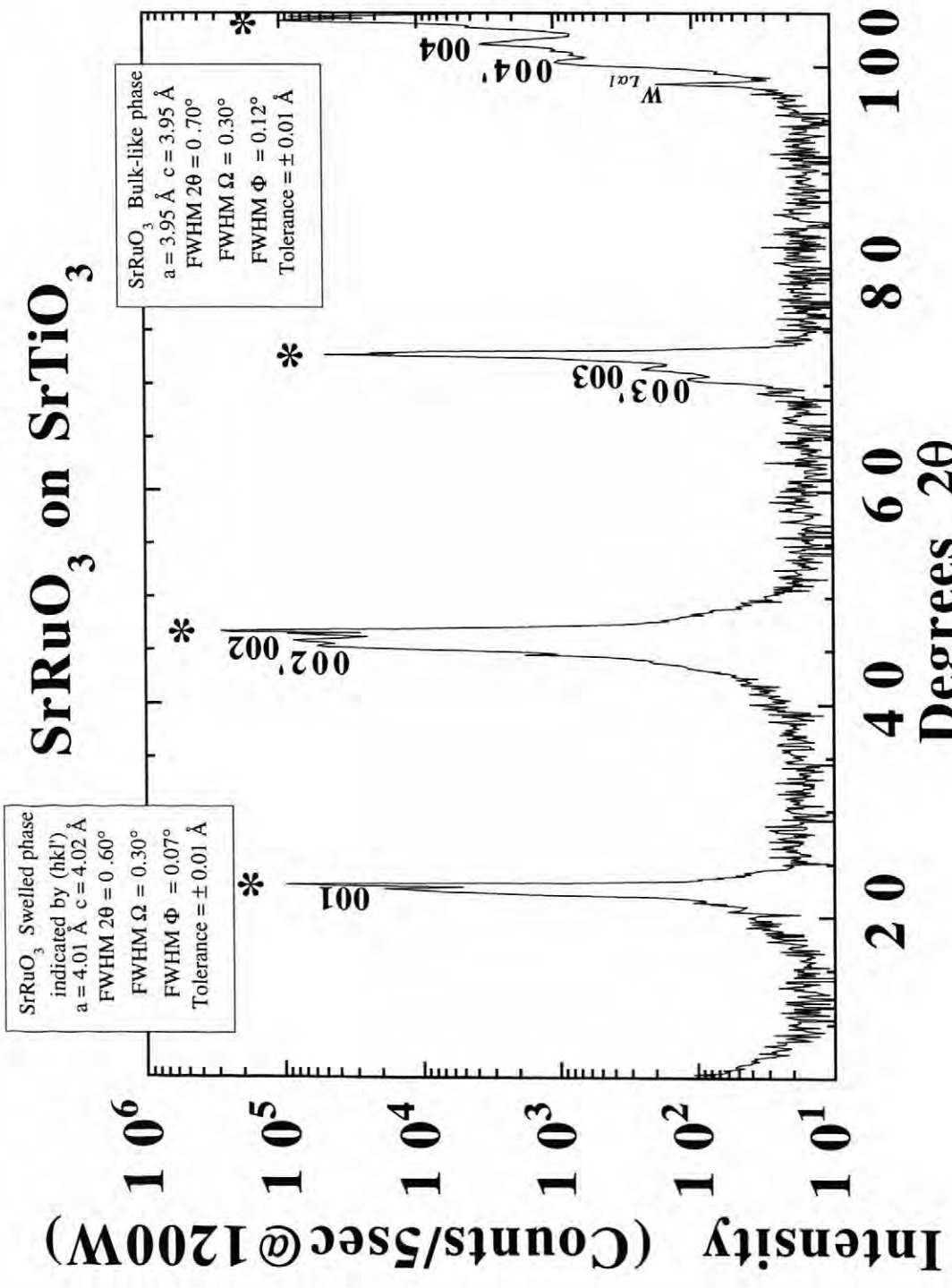

Figure 5.25: θ-2θ scan of off-axis deposited $SrRuO_3$

In the case of the off-axis grown film, it is believed that the extra phase was caused by a a deviation from stoichiometry from the 113 phase. Electrical property measurements, which will be discussed below, support this conclusion.

A second experiment was designed to separate the effects of bombardment and oxygen pressure. A final strontium ruthenate film was deposited under an atmosphere of 20 mTorr ozone/oxygen mix and 140 mTorr of argon, giving a total pressure of 160 mTorr. The cation oxidation states should be similar to the low pressure on-axis film, but now, the inert argon component of the atmosphere should effectively reduce the energetic bombardment to a level similar to that experienced by the high pressure on-axis deposited film. Figure 5.26 shows the x-ray diffraction pattern in two theta for the $SrRuO_3$ film deposited in an atmosphere of ozone/oxygen and argon. Again, diffraction patterns were taken for the other circles, and the film was found to be epitaxial with the substrate.

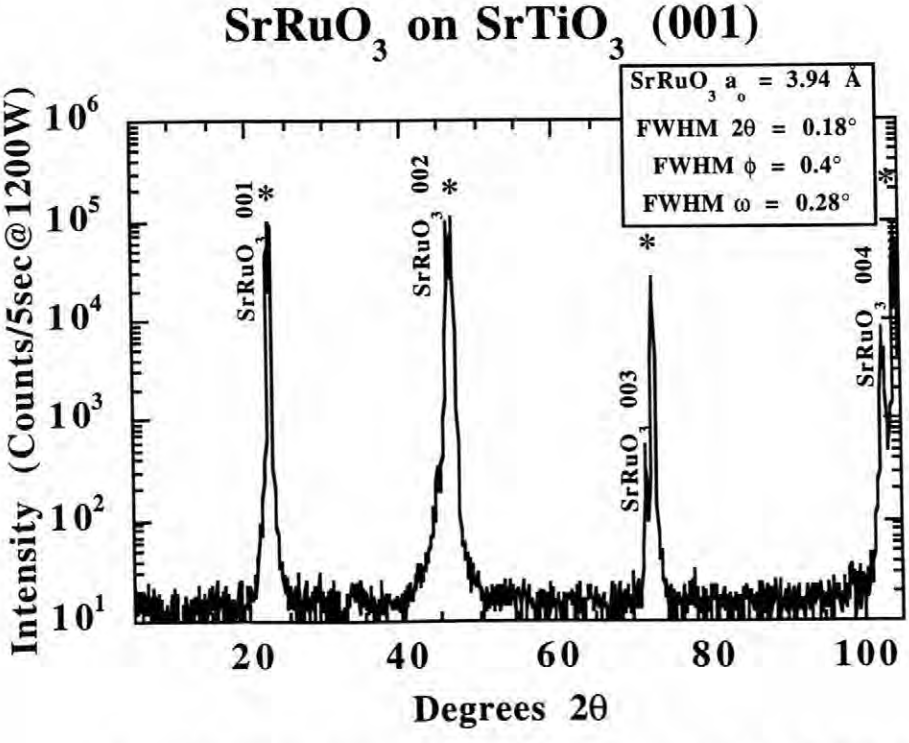

Figure 5.26: θ-2θ pattern for $SrRuO_3$ deposited in O_3/O_2/Ar mix

The x-ray diffraction data indicates that the film deposited under the oxygen/ozone/argon mix is cubic with nearly bulk lattice constant values. This result indicates that energetic bombardment during deposition rather than a lack of oxidant was responsible for the anomalous crystalline structure.

Along with the crystallinity, the electrical properties of the $SrRuO_3$ films varied as a function of deposition parameters. Shown in figure 5.27 is the temperature dependence of the $SrRuO_3$ resistivity in the low temperature regime.

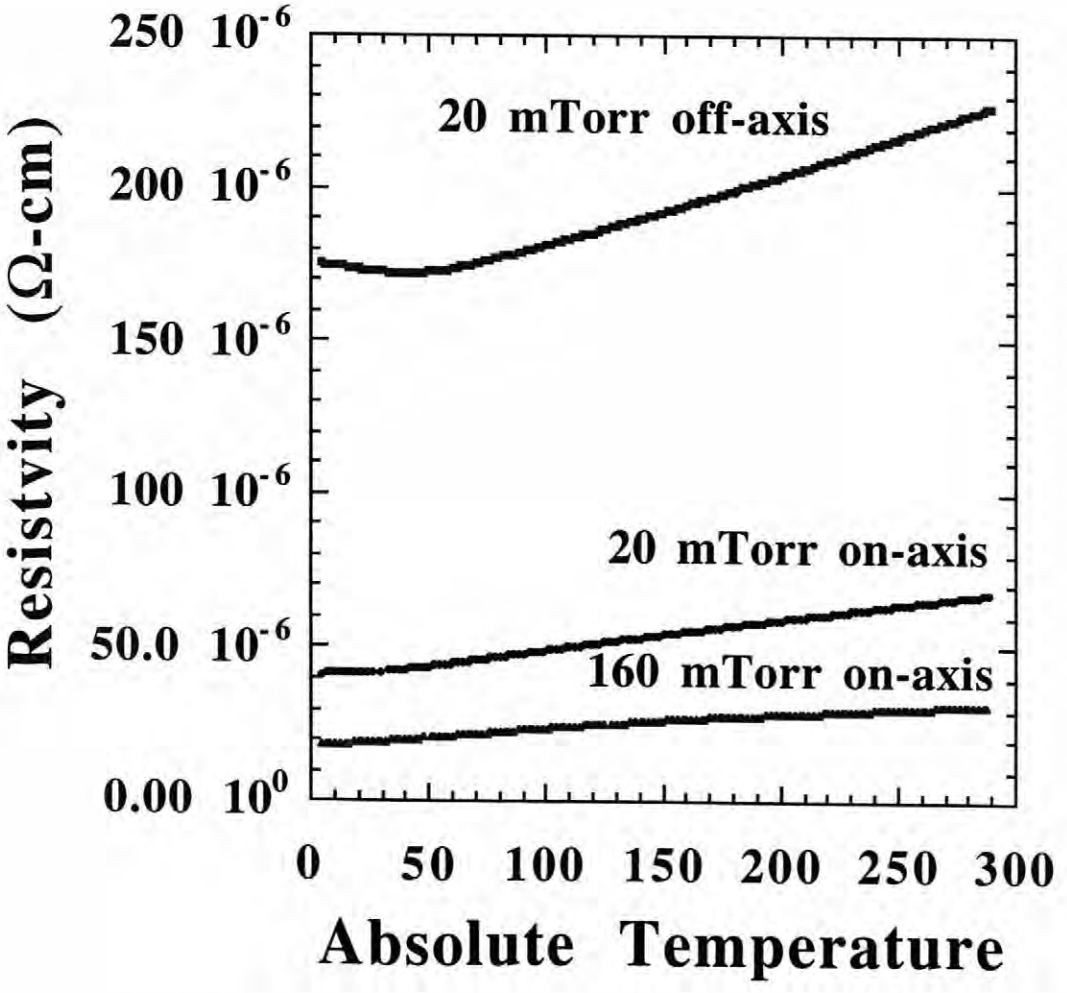

Figure 5.27: Temperature dependence of the resistivity of $SrRuO_3$ films

Upon comparison of the structural and electrical characterization it is quickly realized that the films subject to the least amount of energetic bombardmant during deposition not only had a crystalline structure most similar to the bulk, but in addition, had the lowest resistivity. With the exception of the off-axis deposited film, all samples behaved in a purely metallic fashion; that is, their resistivity decreased nearly linearly with temperature. The off-axis deposited film shows some transition to semiconducting behavior below 30 K, at which point the slope of the resistivity versus temperature curve changed sign. Due to the appearance of extra reflections in the x-ray pattern, it is believed that an off-stoichiometry phase is present in the film. It is possible that the presence of multiple phases is leading to the transition to semiconducting behavior at low temperatures.

Two models have been proposed to explain the increase in resistivity in samples subjected to energetic bombardment. Important to both is the following mechanism of conductivity in strontium ruthenate: In the perovskite structure, the adjacent oxygen/ruthenium octahedra exhibit overlapping orbitals in the order ruthenium, oxygen, ruthenium, etc, with π-overlap between the oxygen p and the ruthenium t_{2g} orbitals. Given sufficiently strong overlap a π and π^* band would result. Partial occupation of the π^* band would then lead to metallic conductivity [Callaghan *et al.*, 1966]. The very small value of resistivity in $SrRuO_3$ suggests that the mechanism of conduction is delocalized electrons, such as those found in π^* bands, rather than charge hoppng between localized states.

The change in conductivity between the low and high pressure deposited films can be explained by purely geometric argument involving a swelling of the perovskite lattice. If the swelled lattice of the low pressure deposited film is considered to slightly increase the distance between oxygen octahedra, then as a result, the orbital overlap would decrease and the delocalization of electrons in π^* bands would be reduced. The most likely result of such an occurrence would be to increase the material's resistivity. A schematic representation of this activity is illustrated in figure 5.28 below.

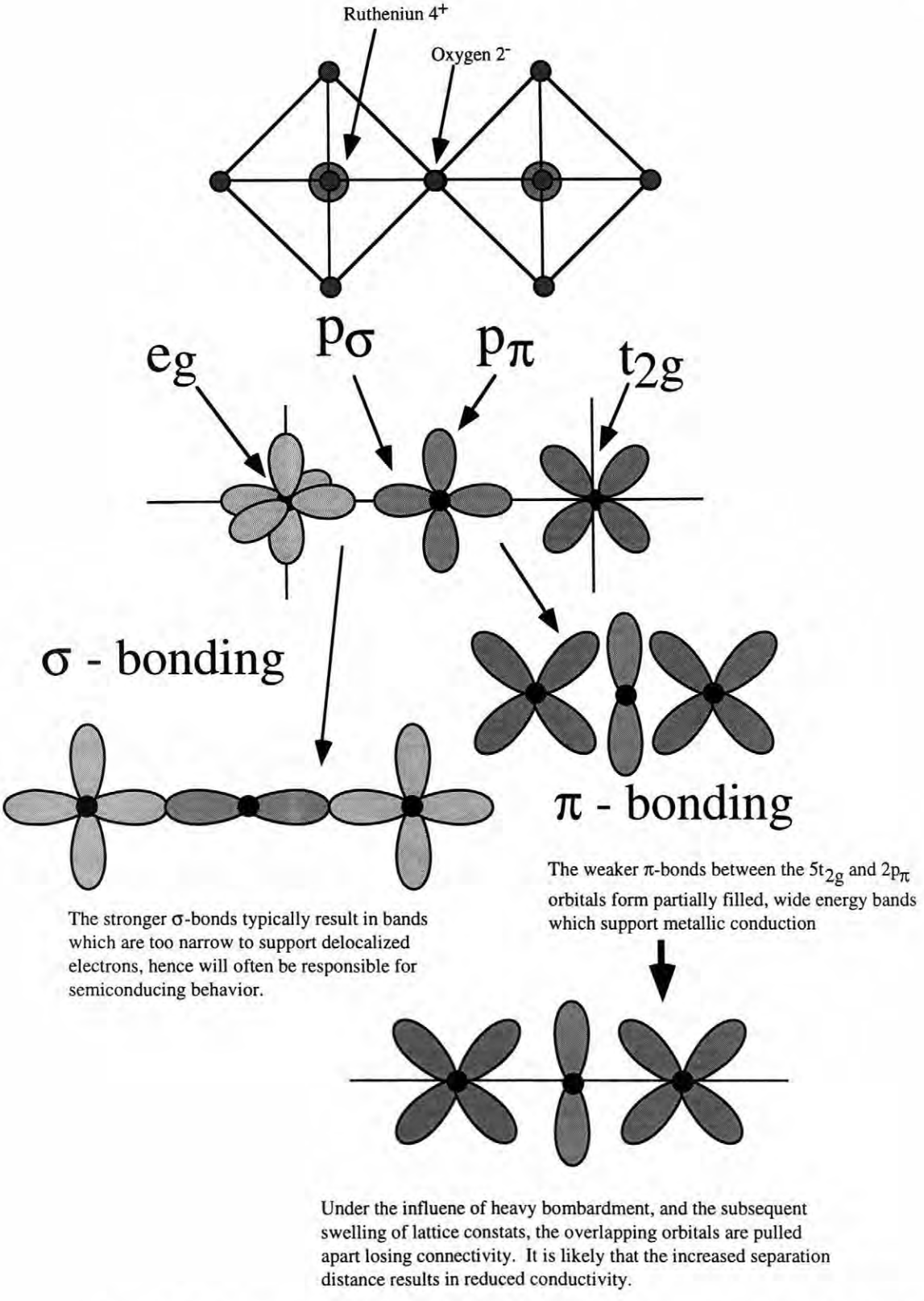

Figure 5.28: Mechanism for increasing resisitivity in bombarded $SrRuO_3$ films

The second mechanism relies upon a more theoretical arguement involving the incorporation of disorder into the crystalline structure and the resulting loss of symmetry between atomic sites and the pertubation of the interatomic potential array. Consider that each atomic site, in a perfectly ordered lattice, would have associated with it a Hamiltonian operator H_{ii}, all of which being identical. In this case, the overlap would result in an energy band, delocalized electrons, and metallic conductivity. If, however, some disorder were introduced into the lattice, a distribution of Hamiltonian operators would be required to represent the atomic array. Figure 5.29 illustrates this idea.

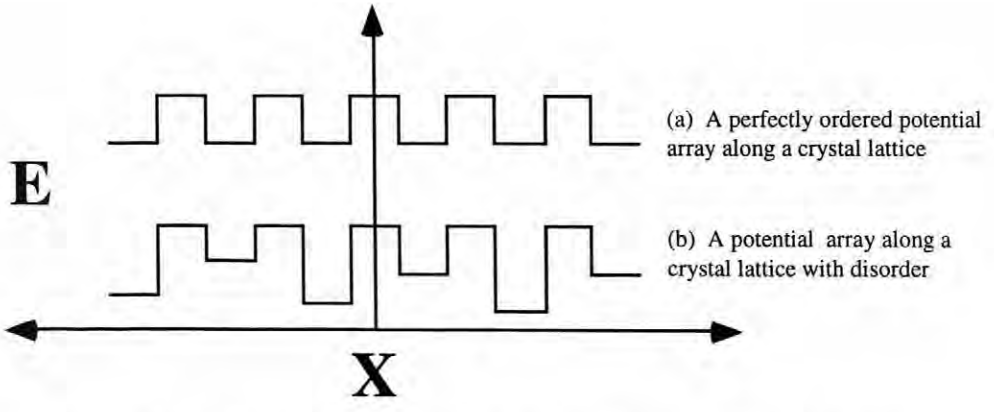

Figure 5.29: Potential distribution in (a) a perfect crystal and (b) a disordered crystal

If a distribution of slightly different potentials were encountered, all of the atoms centered around the mean potential value would have enough neighbors with similar H_{ii} values to form an energy band. Those atoms in the tail of the distribution with H_{ii} values far from the mean would have a localized character since an insufficient quantity would be present to promote band formation [Anderson, 1958, and Mott, 1974]. Figure 5.30 shows the Anderson localization in diagram form depicting the distribution of localized and delocalized states.

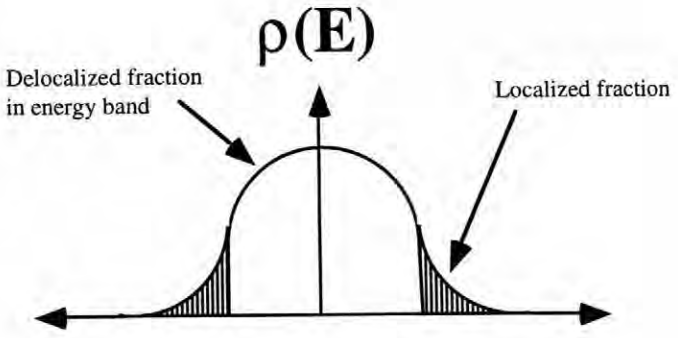

Figure 5.30: Anderson distribution of localized and delocalized states

The physical analog of this model is delocalized regions sandwiched between localized orbitals [Burdett, 1995]. This should lead to an increase in resistivity. The localized regions would be separated from the delocalized portions by a mobility gap with a temperature dependence. This treatment implies that when enough disorder is incorporated into a crystal, semiconducting behavior would be observed where temperature would promote carriers from the localized states, imparting a positive temperature coefficient of resistivity.

It is possible that both mechanisms contribute to the observed increase in resistivity for the heavily bombarded sample. Future work including mobility measurements and carrier concentrations should help to further elucidate the appropriate mechanism.

It should be noted, that in comparison to data published for single crystal $SrRuO_3$, the room temperature values of resistivity for laser ablation prepared $SrRuO_3$ are between a factor of 2 or three lower. However, the resistivity values converge at low temperatures, both on the order of 20 μΩ-cm [Bouchard and Gillson, 1972]. If the resistivity values for the ablated films are accurate, it is likely that subtle changes in stoichiometry are responsible for the disparities.

Chapter 6

SUMMARY AND FUTURE WORK

6.1 Hardware

Beginning with an existing standard high vacuum chamber equipped for room temperature deposition of oxide thin film materials, several improvements and upgrades were performed to facilitate the growth of epitaxial $BaTiO_3$ films and heterostructures. A high temperature block heater capable of achieving a maximum operating temperature of 750°C was designed and constructed. These temperatures allow the epitaxial growth of most perovskite phases. A new target rotation system was installed, as well as new hardware for pressure measurement and gas introduction. An ozone generator capable of producing 8% ozone with a balance of molecular oxygen was installed. Using an ozone/oxygen mix allowed a greater range of pressures to be used while still insuring complete oxidation of multiple cation complex oxides.

6.2 Deposition uniformity study

Time averaged deposition rate and spatial film thickness uniformity was investigated by depositing amorphous strontium ruthenate upon glass slides at room temperature at a variety of pressures, distances, and geometries.

For deposition in the on-axis geometry, the total deposited thickness for depositions at constant target to substrate distances was found to exhibit a maximum value when studied as a function of pressure. Specifically, when using a constant target to substrate distance of 7.0 cm, the time averaged deposition rate was found to exhibit a maximum value at a pressure between 50 and 75 mTorr. This maximum was attributed to scattering

of the ablated species by the ambient gas. The multiple components of the laser induced plasma and their distribution of kinetic energies were used to explain the maxima. When the surface structure of these films was investigated by optical microscopy it was realized that bombardment by energetic species occurs in laser ablation and has a dramatic effect on the thin film morphology. The trends observed for laser ablation were found to be analogous to those observed in sputtering processes and could be accounted for by the well known structure zone model relationships

At the constant deposition pressure of 50 mTorr, the target to substrate distance was varied. It was observed that though the average deposition rate decreased with increasing target to substrate distance, the thickness uniformity improved until ultimately thickness uniform regions ~ 1.0" in diameter could be observed.

Similar experiments were conducted using the off-axis geometry where the primary plume propagation direction (normal to the target surface) was parallel to the substrate growth face. In these experiments no maximum value in deposition rate was observed as pressure was varied. This however may only be true since the appropriate pressure regime was not investigated. Uniform thickness regions were not observed in any of the pressures investigated. In each case, the deposited thickness dropped monotonically with increasing distance from the target. The rate at which the thickness fell was found to be independent of ambient gas pressure.

In the on-axis experiments the thickness uniformity was found to be absolutely limited by the geometry of the substrate and substrate holder. This is to say that a small substrate, 10 mm x 10 mm, if deposited on without being mounted on a large flat plate would show optical interference fringes about its periphery indicating reduced thickness. When the same substrate was mounted upon a flat plate much larger than itself and a film deposited under the otherwise identical conditions, no optical interference fringes would be observed, indicating uniform thickness. This behavior was explained by the locally high pressures in the laser plasma and turbulent flow of the ablatant around physical

discontinuities such as wafer holders. These experiment suggest that baffling schemes could possibly be employed to achieve larger area depositions.

6.3 Deposition of epitaxial barium titanate

The epitaxial deposition of $BaTiO_3$ on several substrates was attempted and optimized for all. Given the appropriate deposition conditions, MgO, LiF, $SrTiO_3$, and $LaAlO_3$ were all found to be suitable for high quality barium titanate growth. Table 8 summarizes the deposition conditions and crystallinity of $BaTiO_3$ thin films on all substrates used.

Table 8: Results of $BaTiO_3$ depositions

Substrate (001) oriented	Deposition Temperature (°C)	FWHM ϕ - circle	FWHM 2θ - circle	FWHM ω - circle
MgO	650 +	1.2°	0.7°	1.2°
LiF	550	1.5°	0.5°	0.8°
$SrTiO_3$	650 +	0.8°	0.3°	0.3°
$LaAlO_3$	650 +	1.2°	0.4°	0.4°

When deposited on MgO, LiF, and $SrTiO_3$, $BaTiO_3$ was found to grow purely c-axis oriented. For ultra-thin $BaTiO_3$ deposited on $LaAlO_3$, (~250 - 500 Å) some a-axis oriented material was detected. However, when the film thickness increased to ~ 1000 Å, only c-axis oriented material was apparent to x-ray analysis. It is felt that when the film thickness increased, the stress state of the film must have changed in such a way as to make nucleation of a-oriented grains energetically unfavorable upon cooling through the ferroelectric transition.

6.4 Heterostructure deposition

In order to measure the electrical properties of $BaTiO_3$ thin films, heterostructures involving an epitaxial bottom electrode were necessary. In this investigation the 113 phase of strontium ruthenate, $SrRuO_3$, was used. Strontium ruthenate was successfully deposited epitaxially on $LaAlO_3$ and $SrTiO_3$ substrates. When deposition on MgO was attempted epitaxial films were unable to be grown, small amounts of {110} oriented material were always observed. Heterostructures consisting of a $BaTiO_3$ layer on a $SrRuO_3$ bottom electrode on both $SrTiO_3$ and $LaAlO_3$ substrates were successfully deposited. The crystallinity and morphology of the films were found to be strongly correlated and dependent upon the deposition pressure and geometry.

When both layers were deposited off-axis the films always exhibited a columnar structure even though grown at high temperatures. When structurally characterized, these films were found to be perfectly oriented in two theta, but extra orientations were always present in-plane. These extra orientations were attributed to the evolution of surface roughness which made nucleation of misoriented grains favorable.

To overcome these problems, extra energy was added to the films via energetic bombardment. Initially, the $BaTiO_3$ was grown on-axis with an off-axis grown $SrRuO_3$ electrode. Ultimately, both layers were grown on-axis as boulders were not found to seriously hinder electrical property measurements. Reduction of boulder populations was the primary motivation for off-axis deposition. When the barium titanate layer was grown on-axis at low pressures dramatic changes in the crystal structure were observed and attributed to energetic bombardment. Typically, when considerable bombardment was present, a second phase with extended lattice constants was detected. This phase was found to orient epitaxially on the substrate. At sufficiently large pressures and target/substrate separations these effects were not observed.

6.5 Electric property measurements

Three thin film heterostructures were fabricated and electrically characterized. In general, a trend of decreasing dielectric constant, switchable polarization, and transition temperature was observed with decreasing crystallinity and epitaxial orientation. Two of the films having similar growth conditions, thicknesses, and morphologies, were compared and studied and in order to prove the existence of a size-induced phase transition. The crystallinity of the pair was quantified using Williamson-Hall's method. Neither film showed bulk barium titanate electrical properties; both were in the size range where their transitions became diffuse and displaced from bulk values. Compositional measurements by RBS and DCP spectroscopy determined that the $BaTiO_3$ layers were consistently Ti rich by ~3 %. This deviation from stoichiometry manifested itself in large values of dielectric loss and conductivity at high fields and temperatures. Low voltage and liquid nitrogen temperature hysteresis measurements were used to prove that true ferroelectric transitions occurred, and were not simply an artifact of the conduction and loss. Sample BSS-12, which was determined to have a coherent crystal length of ~ 75 nm displayed a transition at ~ 58°C, while sample BSL-18, which had a coherent scattering length of ~ 45 nm displayed a transition at ~ 35°C. The coercive fields of the samples were found to increase with decreasing crystallinity. Table 9 gives an abbreviated summary.

Table 9: Electrical property data summary

	BSS-12	BSL-18
T_c	58 °C	- 35 °C
K_{max}	~ 150	~ 65
P_r - High V, Low T ($\mu C/cm^2$)	3.0	1.9
Coherence length (Å)	758	495

Due to differences in deposition geometry and morphology, the third sample could not be used in direct comparison with the others. This film showed greater values of resistivity, and it is believed that the presence of a thin film microstructure aided in isolating the otherwise mobile film carriers. This sample was, however, useful for modeling as the dielectric constant dropped linearly with temperature above the transition. The Curie-Weiss constant was calculated to be ~ 14,000 K^{-1} which is approximately 10 times smaller than what is expected from the bulk. Classical scaling theory was applied to the high temperature data to independently determine the gamma-exponent, which indicates the mathematical relationship between temperature and inverse permittivity. The value of the gamma exponent may offer some indication of whether or not Curie-Weiss behavior is being followed. For the sample investigated, the gamma coefficient was found to deviate from the classical value of unity. Further investigation and comparison to similar calculations on other samples is necessary to determine the validity of this model. Future work will include a compositional study of the $BaTiO_3$ films in order to reduce the conductivity. The possibility of adding donor dopants such as Mn^{4+} and Nb^{4+} to compensate trapped electrons will be investigated. In addition, a TEM investigation of the $BaTiO_3/SrRuO_3$ interface will be performed

6.6 Pressure and bombardment dependence of $SrRuO_3$

Since it was believed that the bottom electrodes played some role in observed properties of the barium titanate films, additional work was undertaken to investigate the material characteristics.

After the observation of elongated lattices constants and enlarged values of resistivity, the role of the deposition parameters, namely oxygen pressure and energetic bombardment, on the structure and properties of $SrRuO_3$ was investigated.

By a combination of depositions at high and low pressures, on and off-axis geometries, and variable partial pressures of oxygen, it was found that the level of energetic

bombardment had a dramatic influence upon the properties. In general, it was observed that with increasing energetic bombardment by the target species, the $SrRuO_3$ lattice swelled by as much as 3%, and the resistivity rose by greater than a factor of two. Experiments which varied the amount of oxidant while maintaining a constant level of energetic bombardment were also performed by deposition in a mixed atmosphere of oxygen and argon. Down to pressures of 20 mTorr O_3/O_2, the structure of the $SrRuO_3$ resembled the bulk. Electrical properties were not measured on these samples, but those experiments will be included in future work.

To explain the observed trends, two models have been proposed. The first model suggests that the swelling of the lattice results in a reduction in orbital overlap and consequent increase in resistivity, while the second involves the concept of an Anderson transition which relates the incorporation of disorder into a crystal to a metal-insulator transition. Currently, neither model can be substantiated. Future work including mobility and carrier density measurements as well as an investigation of the optical properties should help elucidate the mechanisms responsible for the observed experimental findings.

REFERENCES

Abe, K. and S. Komatsu, "Dielectric Constant and Leakage Current of Epitaxially Grown and Polycrystalline $SrTiO_3$ Thin Films," Jpn. Journl. Appl. Phys., vol 32 No. 9B pp. 4186-4189, (1993).

Abe, K. and S. Komatsu, "Thickness Dependence of Induced Ferroelectricity in Epitaxially Grown $Ba_{0.44}Sr_{0.56}TiO_3$ Thin Films," MRS Proceeddings, vol. 310 pp. 285-287, (1994).

Anderson, P. W., "Absence of Diffusion in Certain Random Lattices," Phys. Rev., vol. 109, no. 5, pp. 1492- 1505, (1958).

Anliker, M. , H. R. Bruger and W. Kanzig, "Behavior of Colloidal Seignette-Electrics: III," Helv. Phys. Acta., vol. 27, pp. 99-124, (1954).

Arlt, G., D. Hennings, and G. de With, "Dielectric properties of fine grained barium titanate ceramics," J. Appl. Phys., vol. 54, no. 4, pp. 1619-1625, (1985).

Akhsakhalyan, A. D., Yu, A. Bityurin, S. V. Gaponov, A. A. Gudkov, and V. I. Luchin, "Processes occurring in an erosion plasma during laser vacuum deposition of films. II. Interaction of laser erosion products with the solid surface." Sov. Phys. Tech. Phys., vol. 27, no. 8, pp. 973-977, (1982).

Atwater, H. A., F. A. Houle, and D.H. Lowndes, (eds.) "Surface Chemistry and Beam-Solid Interactions," MRS Symposium Proceedings vol. 201 (1990).

Beech, F. and I. W. Boyd, Photochemical Processing of Electronic Materials, edited by Boyd and Jackman, Academic Press, pp. 350-423, (1991).

Binder, K., "Surface Effects on Phase Transitions in Ferroelectrics and Antiferroelectrics," Ferroelectrics vol. 35 pp. 99-104 (1981).

Biryukov, S. V., V, M, Mukhortov, A. M. Margolin, Yu. I. Golovko, I. N. Zakharchenko, V. P. Dudkevich, and E. G. Fesenko, "Phase Transitions in Polycrystalline and Heteroepitaxial Ferroelectric Films," Ferroelectrics, vol. 56, pp. 115-118, (1984).

Bouchard, R. J. and J. L. Gillson, "Elecetrical Properties of $CaRuO_3$ and $SrRuO_3$ Single Crystals," Mat. Res. Bul., vol. 7, pp. 873-878, (1972).

Burdett, J. K., Chemical Bonding in Solids, Oxford University Press, New York, (1995).

Callaghan, A., C. W. Moeller, and R. Ward, "Magnetic Interactions in Ternary Ruthenium Oxides," Inorganic Chemistry, vol. 5, No. 9, pp. 1572-1576, (1966).

Cao, W., and C. A. Randall, "The Grain Size and Domain Size Relations in Bulk Ceramic Ferroelectric Materials," (To be published), (1995).

Ceramic Materials for Electronics: Properties, Processing, and Applications, edited by R. C. Buchanan, Marcel Dekker Inc., New York, 1986.

Champeaux, C., D. Damiani, C. Girault, P. Marchet, J. Aubreton, J. P. Meccurio, and A. Catherinot, Laser Ablation of Electronic Materials: Basic Mechanisms and Applications. edited by E. Fogarassy and Lazare, North Holland, Amsterdam, p141 (1992).

Cheung, J. T. and H. Sankur, "Growth of films by laser Induced Evaporation," CRC Critical Reviews in Solid State and Material Science. vol. 15, no. 63 (1988).

Pulsed Laser Deposition of Thin Films, edited by D. B. Chrisey and G. K. Huebner, Wiley Interscience, New York, (1994).

Daniels, J. and K. H. Haerdtl, "Electrical Conductivity at High Temperatures of Donor Doped Barium Titanate Ceramics," Philips Res. Rep., vol. 31, pp. 489-504, (1976).

Desu, S. B., "Influence of Stresses on the Properties of Ferroelectric $BaTiO_3$ Thin Films," J. Electrochem. Soc., vol. 140, no. 10 pp. 2981-2987, (1993).

Dudkevich, V.P., I. N. Zachachenko, and E.G. Fenesko, "The Surface Layer in Oxide Ferroelectric Crystals'" Ferroelectrics, vol. 18 pp. 185-190 (1977).

Dudkevich, V. P., V. M. Mukhortov, Y. I. Golovko, Y. G. Sindeev, and E. G. Fesenko, "Internal Size Effect in Condensed $BaTiO_3$ Ferroelectric Films." Phys. Solid State (a), vol. 65, pp. 463-467, (1981).

Dyre, P. E., S. D. Jenkins, and J. Sidhu, "Development and origin of conical structures on XeCl ablated polymide.," Appl. Phys. Lett. 49(8), 453-455 (1986).

Emmony, D. C., R. P. Howson, and L.J. Willis, Appl. Phy. Lett. vol. 51 no. 24, pp. 2054-2055 (1973).

English, F. L., "Electron Mirror Spectroscopy of $BaTiO_3$ surfaces," Journ. Appl. Phys., vol 39, no. 128 pp. 3231-3236, (1969).

Eom, C. B., personal communication, 1995.
V. N. Fillipovich and A. M. Kalinina, "Critical Amorphization Radius in Crystals," Struct. Glass, vol. 5, pp. 34-38, (1965).

Forsbergh, P. W. Jr., "Effects of a Two Dimensional Pressure on the Curie Point of Barium Titanate," Phys. Rev., vol. 93 no. 4 pp. 686-692 (1954).

Frey, M. H. and D. A. Payne, "Nanocrystalline barium titanate: Evidence for the absence of ferroelectricity in sol-gel derived thin-layer capacitors," Appl. Phys. Lett., vol. 63, no. 20, pp. 2753-2755, (1993).

Gitel'son, A. A., A. M. Leier, V. S. Milchzevsk, V. M. Murkhortov, and S. V. Orlov, "Physical Properties of $BaTiO_3$ $SrTiO_3$ Ferroelectric Thin Films in Weak Electric Fields," Soviet Phys. Solid State, vol. 19, no. 7, pp. 1121-1124, (1978).

Goehegan, D. B., Laser Ablation: Mechanics and Applications, edited by J.C. Miller and R.F. Haglund, Springer-Verlag, Heidlberg, p. 28 (1991).

Goehegan, D. B., "Fast intensified photography of $YBa_2Cu_3O_{7-x}$ laser ablation in vacuum and ambient oxygen," Appl. Phys. Lett. vol. 60, 2732 (1992).

Goswami, A. K., "Dielectric Properties of Unsintered $BaTiO_3$," J. Appl. Phys., vol 50. no. 5 pp. 619-624, (1969).

Hayashi, T., N. Ohji, K. Hirohara, T. Fukunaga, and H. Maiwa, "Preparation and Properties of Ferroelectric $BaTiO_3$ Thin Films by the Sol-Gel Process," Japn. J. of Appl. Phys. vol. 32 pp. 4092-4094 (1993).

Herbert, J. M., Ceramics Dielectrics and Capacitors, edited by D.S. Campbell, Gordon and Breach Science Publishers, NY (1985).

Jaffe, B., W. R. Cook Jr., and H. Jaffe, Piezoelectric Ceramics, Academic Press Ltd., India, (1971).

Kamalasanan, M. N, N. Deepak Kumar, and S. Chandra, "Dielectric and Ferroelectric Properties of $BaTiO_3$ Thin Films Grown by the Sol-Gel Process," J. Appl. Phys. vol. 79 no. 9 pp. 5679-5685 (1993).

Kinoshita, K. and A. Yamaji, "Grain-size effects on dielectric properties in barium titanate ceramics," J. Appl. Phys., vol. 47, no. 1, pp. 371-373, (1975).

Kniepkemp, H. and W. Heywang, "Depolarization Effects in Polycrystalline Barium Titanate," Z. Agnew Phys,. vol. 6, pp. 385-390, (1954).

Koren, G., R. J. Baseman, A. Guptz, M. I. Lutwyche, and R. B. Laibowitz, "Particulates reduction in laser ablated $YBa_2Cu_3O_{7-\partial}$ thin films by laser induced plume heating, " Appl. Phys. Lett. vol. 56, 2144-2146 (1990).

Krupanidhi, S. B., D. Roy, N. Maffei, and C. J. Peng, "Pulsed Laser deposition of Ferroelectric Thin Films," Integrated Ferroelectrics, vol. 1, pp. 253-268, (1991).

Kurogi, H., Y. Yamagata, T. Ikegami, K. Ebihara, B. Y. Tong, and K. Kumamoto, "Preparation of $PbZr_xTi_{1-x}O_3$ thin films by KrF excimer laser abation technique," unpublished, (1996).

Kuroiwa, T., T. Honda, H. Watarai, N. Mikami, T. Makita, and K. Sato, "Conduction Mechanisms of $SrTiO_3$ Thin Films by RF-Sputtering," Ceram. Trans, vol. 43, pp. 219-224, (1994).

Kretschmer, R. and K. Binder, "Surface Effects and Phase Transitions in Ferroelectrics and Dipolar Magnets," Phys. Rev. B, vol. 20 no. 3 pp. 1065-1075 (1979).

Lezgintseva, T. N., "Concerning the Structure of Surface Layers in Barium Titanate Crystals," Sov. Phys.-Solid State, vol. 7 no.4 pp. 785-788 (1965).

Lines,M. E., and A. M. Glass, Principles and Applications of Ferroelectrics and Related Materials, edited by W. Marshall and D. H. Wilkinson, Oxford University Press, Oxford, (1979).

Lu, H. A., L. A. Wills, D. W. Wessels, X. Zhan, J. A. Helfrich, and J. B. Ketterson, "Ferroelectric Properties of a-axis Textured Barium Titanate Thin Films," MRS Proceedings vol. 310 p. 319-323 (1994).

Maffei, N., "Excimer Laser Ablated Bismuth Titanate Thin Films For Nondestructive Readout Nonvolatile Memory Applications," PhD Thesis, Penn State University, (1993).

McKee, R. A., F. J. Walker, E. D. Specht, G. E. Jellison, Jr., L. A. Boatner, and J. H. Harding, "Interface stability and the growth of optical quality perovskites on MgO," Phys. Rev. Lett., vol. 72, pp. 2741-2744 (1994).

Merz, W. J., Phys. Rev., vol. 76, pp. 1221-12225, (1949).

Merz, W. J., Phys. Rev., vol. 91, pp. 513-517, (1953).

Messier, R., "Toward quantification of thin film morphology," J. Vac. Sci. Tech. A, vol. 4, No. 3, pp. 490-495, (1985).

Mikami, N. T., Horikawa, T. Makita, K. Sato, T. Kurowitz, T. Honda, and H. Watarai, "Dielectric Properties of Barium Strontium Titanate Films by RF Sputtering,"

Mott, N. F., Metal Insulator Transitions, London, Harper and Row Publishers, New York, (1974).

Müller, E. K., B. J. Nicholson, and G. L. Turner, " The Epitaxial Vapor Deposition of Perovskite Materials," J. Electrochem. Soc., vol. 110, no. 9, pp. 969-973, (1963).

Murakami, T. and A. Yamaji, "Dy-doped $BaTiO_3$ ceramics for high voltage capacitor use," Amer. Ceram. Soc. Bull., vol. 55, No. 6, pp. 572-575, (1972).

Newnham, R. E., and S. K. Trolier-McKinstry, "Structure Property Relationships in Ferroelectric Nano-composites," Ceram. Trans. vol. 8, pp. 235-252, (1990).

Nix, W. D., "Mechanical Properties of Thin Films," Metallurgical Transactions A, Vol. 20A, pp. 2217-2245, (1989).

Norton, M. G., and C. Barry Carter, "Observation of the early stages of heteroepitactic growth of $BaTiO_3$ thin-films," J. Mat. Res., vol. 5, no. 12. pp. 2762-2765, (1990).

Nose, T., H. Kim, and H. Uwe, "Dielectric Property of Epitaxial Films of $BaTiO_3$ Synthesized by Laser Ablation," Jpn. Journl. Appl. Phys., vol. 33 No. 9B pp. 5259-5261, (1994).

Payne, D. C., and J. C. Bravman, (eds) "Laser Ablation for Materials Science," MRS Symposium Proceedings vol.191 (1990).

Ramesh, R., A. Inam, W. K. Chan, B. Wilkins, K. Myers, K. Remsching, D. L. Hart, and J. M. Tarascon, "Epitaxial Cuprate Superconductor/Ferroelectric Heterostructures," Science vol. 252, pp. 944-949, (1991).

Robins, L. H., D. L. Kaiser, L. D. Rotter, and P. K. Schenk, "Investigation of the Structure of $BaTiO_3$ Thin FIlms by Raman Spectroscopy," J. Appl. Phys., vol 76 No. 11 pp. 7484-798, (1994).

Samara, G. A., " Pressure and Temperature Dependences of the Dielectric Properties of the Perovskites $BaTiO_3$ and $SrTiO_3$," Phys. Rev., vol. 151 pp. 378-386 (1996).

Schlag, S., H Eicke, and W. B. Stern, "Size Driven Phase Transition and Thermodynamic Properties of Nanocrystalline Barium Titanate," (to be published) J. Phys. Chem. (1996).

Sharma, R. K., N.-H. Chan, and D. M. Smyth, "Solubility of TiO_2 in $BaTiO_3$," J. Amer. Ceram. Soc., vol. 64, No. 8, pp. 448-451, (1981).

Shohata, N., S. Matsubara, Y. Miyasaka, and M. Yonezawa, "Epitaxial Growth of $PbTiO_3$ on $MgAl_2O_4$/Si Substrates," IEEE., vol. 86, pp. 580-584, (1986).

Singh, R. K. and J. Narayan, "Theoretical Model for Deposition of Superconducting Thin Films Using Pulsed Laser Evaporation Technique," J. Appl. Phys. vol. 68 p. 233 (1990).

Smith, D. L., Thin Film Deposition, edited by S.S. Chapman, McGraw Hill Inc., 1995, pp. 220-280.

Smith, H. M. and A.F. Turner, Applied Optics, 4, pp.147-148, 1965.

Robinson, R. S., "Energetic collisions in rare gas plasmas," J. Vac. Sci. Technol., vol. 16, No. 2, pp. 185-188, (1978).

Somekh, R. E., "The thermalization of energetic atoms during the sputtering process," J. Vac. Sci. Technol. A, vol. 2, No. 3, pp. 1285-1291, (1984).

Strikovski, M. D., E. B. Kluenkov, and S. V. Gaponov, "Crossed fluxes technique for pulsed laser deposition of smooth YBCO films and multilayers," Appl. Phys. Lett., vol. 63, No. 23, pp. 1146-1148, (1993).

Surowiak, Z., A. M. Margolin, I. N. Zakarchenko, and S. V. Biryukov, "The Influence of Structure on the Piezoelectric Properties of $BaTiO_3$ and (BaSr)TiO_3 Thin Films With a Diffuse Phase Transition," Thin Solid Films, vol. 176, pp. 227-246, (1989).

Tabata, H., H. Tanaka, and T. Kawai, "Construction of Strained $BaTiO_3$/$SrTiO_3$ Superlattices and Their Dielectric Properties," Preprint, (1995).

Tabata, H., H. Tanaka, and T. Kawai, "Formation of Artificial $BaTiO_3$/$SrTiO_3$ Superlattices by Pulsed Laser Deposition and Their Dielectric Properties," Appl. Phys. Lett. vol 65, no. 15, pp. 1970-1973, (1994).

Taylor, R. S., E. K. Leopold, D. L. Singleton, G. Paraskevopoulos, and R. S. Irwin, "The effect of debris formation on the morphology of excimer laser ablated polymers,"J. Appl. Phys. vol. 64 no. 5, 2815-2818, (1988).

Terauchi, H., Y. Watanabe, H. Kasatane, K. Kamagaki, Y. Yano, T. Terashima, and Y. Bando, "Structural Study of Epitaxial $BaTiO_3$ Crystals," J. Phys. Soc. Jpn., vol 61, no. 7, pp. 2194-2197, (1992).

Thornton, J. A. "Influence of Substrate Temperature and Deposition Rate on Structure of Thick Sputtered Cu Coatings," J. Vac. Sci. Technol., vol. 12, pp. 830, (1975).

Uchino, K., E. Sadanaga, and T Hirose, "Dependence of the Crystal Structure on Particle Size in Barium Titanate," J. Am. Ceram. Soc. vol. 72, no. 8, pp. 1555-1558, (1989).

Uchino, K., N-Y. Lee, T. Toba, N Usuki, H. Aburatani, and Y. Ito, "Changes in Crystal Structure of RF Magnetron Sputtered $BaTiO_3$ Thin Films," J. Ceram. Soc. Jpn., vol. 100, no. 9, pp. 1091-1093, (1992).

Van Buskirk, P. C., G. T. Stauf, R. Gardiner, P. S. Kirlin, B. Bihari, J. Kumar, and L. G. Gallatin, "CVD of Epitaxial Barium Titanate Films for Frequency Doubling Devices," MRS Proceedings vol. 310 p. 119-124 (1993).

Van Driel, H.M., J. E. Sipe, and J. F. Young, "Laser Induced Surface Structure on Solids: A Universal Phenomenon," Physical Review Letters, vol. 49 no. 26, pp. 1955-1958, (1982).

Venkatesan, T., X. D. Wu, R. Muenchhausen, and A. Pique, "Pulsed Laser Deposition Future Directions," MRS Bulletin 17, 54 (1992).

Venkatesan, T., X .D. Wu, A. Inam, Y. Jeon, M. Croft, E. W. Chase, C. C. Chang, J. B. Watchtman, R. W. Odon, F. Radicati, and C. A. Magee, "Nature of the Pulsed Laser Process for the Deposition of High Tc Superconducting Thin Films," Appl. Phys. Lett. vol. 53, p. 1431 (1988b).

Wang, T., K. M. Beauchamp, D. D. Berkley, B. R. Johnson, J. X. Liu, J. Zhang, and A. M. Goldman, "Onset of HTS in The Two-dimensional Limit," Phys. Rev. B. vol. 43, no. 10, 8623-8626 (1991).

Weidman, L.and H. Heluajian, "Laser photodecomposition of sintered $YBa_2Cu_3O_{6+x}$: Ejected species population distributions and initial kinetic energies for laser ablation wavelengths 351, 248, and 193 nm," Journ. of Appl. Phys. vol. 70, p. 4513 (1991).

Williamson,G. K. and W. H. Hall, "X-ray line broadening from filed aluminum and wolfram," Acta. Meta., vol. 1, 22-31, (1953).

Yano, Y., K. Iijima, Y. Saitoh, T. Terashima, Y. Bando, Y. Wantanabe, H. Kasatani, and H. Terauchi, "Epitaxial Growth and Dielectric Properties of $BaTiO_3$ Thin FIlms on Platinum Electrodes," J. Appl. Phys., vol 76 No. 12, pp. 7833-7838, (1994).

Yao, G-D., S. Y. Hou, M. Dudley, and J. M. Phillips, "Synchrotron x-ray topography studies of twin structures in lanthanum aluminate single crystals," J. Mater. Res., vol. 7, no. 7, pp. 1847-1855, (1992).

Yoneda, Y., H. Kasatani, H. Terauchi, Y. Yano, T. Terashima, and Y. Bando, "Ferroelectric Phase Transition in BaTiO3 Thin Films," J. Phys. Soc. Jpn., vol. 62, no. 6, pp. 1840-1843, (1993).

Yoneda, Y., H. Kasatani, H. Terauchi, Y. Tano, T. Terashima, and Y. Bando, "Ferroelectric Phase Transition in $BaTiO_3$ Films," J. Cryst. Growth, vol. 150, pp. 1090-1093, (1995).

Zhang, J., G. Cui, D. Gordon, P. Van Buskirk, and J. Steinbeck, "PE-MOCVD of Conductive Oxide Electrodes for ferroelectric Barium Titanate Capacitors," MRS Proceedings vol. 310 pp. 249-254, (1993).

Zhang, J. P., Z. Q. Huang, D. T. Shaw, and H. S. Kwok, "Generation of high energy atomic beams in laser-superconducting target interactions," Appl. Phys. Lett. vol. 54, no. 3. pp. 280-283, (1989).